Multi-modal, Multi-Domain Pedestrian Detection and Classification : Proposals and Explorations in Visible over StereoVision, FIR and SWIR

Alina Dana Miron

Institut National des Sciences Appliquées de Rouen

Laboratoire d'Informatique de Traitement de l'Information et des Systèmes

Universitatea "Babeş-Bolyai"

Facultatea de Matematică şi Informatică, Departamentul de Informatică

P H D T H E S I S

Speciality : Computer Science

Defended by

Miron Alina Dana

to obtain the title of

Doctor of Computer Science of INSA de ROUEN
and "Babeş-Bolyai" University

Multi-modal, Multi-Domain Pedestrian Detection and Classification:

Proposals and Explorations in Visible over StereoVision, FIR and SWIR

16 July 2014

Jury :

Reviewers:

    Fabrice MERIAUDEAU   -   *Professor*   - "Bourgogne" University

    Daniela ZAHARIE   -   *Professor*   - "West" University of Timisoara

    Crina GROŞAN   -   *Associate Professor*   - "Babeş-Bolyai" University

Examiner:

    Luc BRUN   -   *Professor*   - "Caen" University

PhD Directors:

    Abdelaziz BENSRHAIR   -   *Professor*   - INSA de Rouen

    Horia F. POP   -   *Professor*   - "Babeş-Bolyai" University

PhD Supervisors:

    Samia AINOUZ   -   *Associate Professor*   - INSA de Rouen

    Alexandrina ROGOZAN   -   *Associate Professor*   - INSA de Rouen

To Ovidiu, without whom
I would have never started this thesis
and to my family, that always
supported me

Acknowledgements

These are the voyages of my Phd. Its three-year mission (ok... four years in the end due to the ATER): to explore strange new domains, to seek out new algorithms and new methods, to boldly go where no man has gone before. The manuscript may not be as exciting as the board journal of the Enterprise, but I thank the persons that will have the patience to read it. Also this thesis would not exist without the help of several essential persons.

First of all, I would like to express my gratitude to my two Ph.D. directors, prof. Abdelaziz Bensrhair and prof. Horia F. Pop, for their guidance. I could not have manage to do all this work without the two Universities that hosted me during my thesis: INSA de Rouen in France, where I've conducted almost all my activity, and "Babeş-Bolyai" University in Romania.

Second, I would like express my gratitude to the jury that accepted to review my thesis: prof. Fabrice Meriaudeau (Université de Bourgogne), prof. Daniela Zaharie (West University of Timisoara), Crina Groşan ("Babeş-Bolyai" University) and Luc Brun (Cean University). This list includes my supervision committee from "Babeş-Bolyai" University: prof. Gabriela Czibula, Mihai Oltean and Crina Groşan, and from INSA de Rouen: Samia Ainouz and Alexandrina Rogozan.

I would like to particularly thank Alexandrina Rogozan, without whom I would have never come to France, and Samia Ainouz for her continuous guidance and help for the past years, both professionally and personally.

I'm also grateful for the financial support given by CoDrive project, but also the ATER position that has allowed me to finish writing the manuscript.

I would like to thank also my fellow comrades, the PhD students with whom I have shared ideas, anxieties and joy: Florian, Guillaume, Zacharie, Amnir, Yadu, Vanee, Rawia, Nadine, Xilan, Fabian. Also a special thank to my dear friends, Andreea, Cristina, Roxana, Flavia that had the patience to listen to me complain during these years. I hope I did not forget anyone (If I did, I will buy them an ice cream).

Last, but not the least, I would like to thank my love, Ovidiu, and my family, Ioan, Valeria, Dinu, Marius, who gave me the opportunity to follow my dreams and for their continuous encouragement.

<div align="right">

Un sincer mulţumesc,

Alina Miron

</div>

Summary

The main purpose of constructing Intelligent Vehicles is to increase the safety for all traffic participants. The detection of pedestrians, as one of the most vulnerable category of road users, is paramount for any Advance Driver Assistance System (ADAS). Although this topic has been studied for almost fifty years, a perfect solution does not exist yet. This thesis focuses on several aspects regarding pedestrian classification and detection, and has the objective of exploring and comparing multiple light spectrums (Visible, ShortWave Infrared, Far Infrared) and modalities (Intensity, Depth by Stereo Vision, Motion).

From the variety of images, the Far Infrared cameras (FIR), capable of measuring the temperature of the scene, are particular interesting for detecting pedestrians. These will usually have higher temperature than the surroundings. Due to the lack of suitable public datasets containing Thermal images, we have acquired and annotated a database, that we will name RIFIR, containing both Visible and Far-Infrared Images. This dataset has allowed us to compare the performance of different state of the art features in the two domains. Moreover, we have proposed a new feature adapted for FIR images, called Intensity Self Similarity (ISS). The ISS representation is based on the relative intensity similarity between different sub-blocks within a pedestrian region of interest. The experiments performed on different image sequences have showed that, in general, FIR spectrum has a better performance than the Visible domain. Nevertheless, the fusion of the two domains provides the best results.

The second domain that we have studied is the Short Wave Infrared (SWIR), a light spectrum that was never used before for the task of pedestrian classification and detection. Unlike FIR cameras, SWIR cameras can image through the windshield, and thus be mounted in the vehicle's cabin. In addition, SWIR imagers can have the ability to see clear at long distances, making it suitable for vehicle applications. We have acquired and annotated a database, that we will name RISWIR, containing both Visible and SWIR images. This dataset has allowed us to compare the

performance of different pedestrian classification algorithms, along with a comparison between Visible and SWIR. Our tests have showed that SWIR might be promising for ADAS applications, performing better than the Visible domain on the considered dataset.

Even if FIR and SWIR have provided promising results, Visible domain is still widely used due to the low cost of the cameras. The classical monocular imagers used for object detection and classification can lead to a computational time well beyond real-time. Stereo Vision provides a way of reducing the hypothesis search space through the use of depth information contained in the disparity map. Therefore, a robust disparity map is essential in order to have good hypothesis over the location of pedestrians. In this context, in order to compute the disparity map, we have proposed different cost functions robust to radiometric distortions. Moreover, we have showed that some simple post-processing techniques can have a great impact over the quality of the obtained depth images.

The use of the disparity map is not strictly limited to the generation of hypothesis, and could be used for some feature computation by providing complementary information to color images. We have studied and compared the performance of features computed from different modalities (Intensity, Depth and Flow) and in two domains (Visible and FIR). The results have showed that the most robust systems are the ones that take into consideration all three modalities, especially when dealing with occlusions.

Résumé

L'intérêt principal des systèmes d'aide à la conduite (ADAS) est d'accroître la sécurité de tous les usagers de la route. Le domaine du véhicule intelligent porte une attention particulière au piéton, l'une des catégories la plus vulnérable. Bien que ce sujet ait été étudié pendant près de cinquante ans par des chercheurs, une solution parfaite n'existe pas encore. Nous avons exploré dans ce travail de thèse différents aspects de la détection et la classification du piéton. Plusieurs domaines du spectre (Visible, Infrarouge proche, Infrarouge lointain et stéréovision) ont été explorés et comparés.

Parmi la multitude des systèmes imageurs existants, les capteurs infrarouge lointain (FIR), capables de capturer la température des différents objets, reste particulièrement intéressants pour la détection de piétons. Les piétons ont, le plus souvent, une température plus élevée que les autres objets. En raison du manque d'accessibilité publique aux bases de données d'images thermiques, nous avons acquis et annoté une base de donnée, nommé RIFIR, contenant à la fois des images dans le visible et dans l'infrarouge lointain. Cette base nous a permis de comparer les performances de plusieurs attributs présentés dans l'état de l'art dans les deux domaines. Nous avons proposé une méthode générant de nouvelles caractéristiques adaptées aux images FIR appelées « Intensity Self Similarity (ISS) ». Cette nouvelle représentation est basée sur la similarité relative des intensités entre différents sous-blocks dans la région d'intérêt contenant le piéton. Appliquée sur différentes bases de données, cette méthode a montré que, d'une manière générale, le spectre infrarouge donne de meilleures performances que le domaine du visible. Néanmoins, la fusion des deux domaines semble beaucoup plus intéressante.

La deuxième modalité d'image à laquelle nous nous sommes intéressé est l'infrarouge très proche (SWIR, Short Wave InfraRed). Contrairement aux caméras FIR, les caméras SWIR sont capables de recevoir le signal même à travers le pare-brise d'un véhicule. Ce qui permet de les embarquer dans l'habitacle du véhicule. De plus, les imageurs SWIR ont la capacité de capturer

une scène même à distance lointaine. Ce qui les rend plus appropriées aux applications liées au véhicule intelligent. Dans le cadre de cette thèse, nous avons acquis et annoté une base de données, nommé RISWIR, contenant des images dans le visible et dans le SWIR. Cette base a permis une comparaison entre différents algorithmes de détection et de classification de piétons et entre le visible et le SWIR. Nos expérimentations ont montré que les systèmes SWIR sont prometteurs pour les ADAS. Les performances de ces systèmes semblent meilleures que celles du domaine du visible.

Malgré les performances des domaines FIR et SWIR, le domaine du visible reste le plus utilisé grâce à son bas coût. Les systèmes imageurs monoculaires classiques ont des difficultés à produire une détection et classification de piétons en temps réel. Pour cela, nous avons l'information profondeur (carte de disparité) obtenue par stéréovision afin de réduire l'espace d'hypothèses dans l'étape de classification. Par conséquent, une carte de disparité relativement correcte est indispensable pour mieux localiser le piéton. Dans ce contexte, une multitude de fonctions coût ont été proposées, robustes aux distorsions radiométriques, pour le calcul de la carte de disparité. La qualité de la carte de disparité, importante pour l'étape de classification, a été affinée par un post traitement approprié aux scènes routières.

Les performances de différentes caractéristiques calculées pour différentes modalités (Intensité, profondeur, flot optique) et domaines (Visible et FIR) ont été étudiées. Les résultats ont montré que les systèmes les plus robustes sont ceux qui prennent en considération les trois modalités, plus particulièrement aux occultations.

Mots-clés: Véhicules intelligents, Détection de Piétons, Infrarouge lointain, Infrarouge à ondes courtes, Stéréo Vision

Rezumat

Scopul principal al construției vehiculelor inteligente este de a crește nivelul de siguranță pentru toți participanții la trafic. Detecția pietoniilor, fiind una dintre categoriile cele mai vulnerabile în trafic, este de o importanță majoră pentru orice Sistem de Asistență Avansată la Conducere (en: *Advance Driver Assistance System - ADAS*). Deși acest domeniu a fost studiat de aproape cincizeci de ani, nu există încă o soluție perfectă. Această lucrare se concentrază pe diverse aspecte legate de detecția și clasificarea pietonilor, și are ca obiectiv explorarea si compararea diverselor domenii (Vizibil, Infraroșu de Lungime Scurtă, Infraroșu de Lungime Lungă) și modalități (Intensitate, Disparitate, Flux Optic).

Din divesele tipuri de senzori, spectrul Infraroșu de lungime de unde lungă (en: *FIR*), capabil de a detecta temperatura diverselor obiecte, este deosebit de interesant pentru detectarea pietonilor. Aceștia din urmă, vor avea de regulă o temperatură mai ridicată decât mediul înconjurător. Din lipsa unor baze de date adecvate cu imagini rutiere FIR, am achiziționat și adnotat o bază de date cu imagini din acest spectru de lumină, pe care o vom numi RIFIR, conținând imagini atât în spectrul Visibil cât și FIR. Aceste imagini ne-au permis să comparăm performanța diverselor caracteristici calculate pe imagini în cele două domenii. In contextul imaginilor termice, am propus o nouă caracteristică adaptată pentru imaginile FIR, numită *Intensity Self Similarity (ISS)*. Reprezentarea ISS este bazată pe calculul unor similarități de intensitate între sub-blocuri din interiorul unei regiuni de interes. Experimentele realizate pe diverse baze de imagini au arătat că în general, spectrul FIR are o performanță mai bună decât domeniul Vizibil. Cu toate acestea, fuziunea celor două spectre de lumină a dat performanțele cele mai bune.

După analiza domeniului FIR, am studiat un alt spectru Infraroșu, care nu a fost folosit până acum pentru detecția și clasificarea pietonilor, Infraroșu de Lungime Scurtă (*Short Wave Infrared - SWIR*). Spre deosebire de camerele FIR, cele SWIR au abilitatea de a *vedea* prin parbriz, prin urmare pot fi montate în interiorul vehiculului. În plus, camerele SWIR au posibilitatea de a

vedea clar pe distanțe lungi, ceea ce le face convenabile pentru aplicații ADAS. Am achiziționat și adnotat o nouă bază de imagini, pe care o vom numi RISWIR, conținând imagini atât din Vizibil cât și din SWIR. Testele realizate au arătat rezultate promițătoare pentru spectrul SWIR folosit în aplicații de tip ADAS, având rezultate mai bune decât spectrul Visibil pe imaginile considerate.

Chiar dacă FIR și SWIR au dat rezultate favorabile, spectrul Visibil este încă domeniul cel larg utilizat, în special din cauza costului scăzut al echipamentelor. Clasicele imagini monoculare folosite pentru detecția și clasificarea de obiecte pot să dea un timp de procesare foarte lung. Stereo-Viziunea oferă o modalitate de a reduce spațiul de căutare al ipotezelor prin folosirea informației privind distanța până la obiecte, dată de harta de disparitate. Prin urmare, o hartă de disparitate robustă este esențială pentru a avea ipoteze relevante cu privire la locația pietonilor. În acest context, pentru calculul hărții de disparitate am propus câteva funcții de cost robuste la distorsiuni radiometrice. În plus, am arătat că technici simple de post-procesare pot avea un impact semnificativ asupra calității hărții de disparitate.

Folosirea hărții de disparitate nu este strict limitată la generarea de ipoteze, ci poate să fie utilizată și pentru calcularea unor caracteristici, funizând informații complementare imaginilor color. În acest context, am studiat și comparat performanța caracteristicilor calculate pe diverse modalități (Intensitate, Disparitate și Fluxul Optic) în diverse domenii (Visibil și FIR). Rezultatele au arătat că cele mai robuste sisteme sunt cele care iau în considerare toate cele trei modalități, în special pentru rezolvarea ocluziunilor.

Cuvinte cheie: Vehicule Inteligente, Detecția pietonilor , Infraroșu, FIR, SWIR, Stereo-Viziune

Contents

List of Tables

List of Figures

Introduction

Intelligent autonomous vehicles have long surpassed the stage of a Sci-Fi idea, and have become
a reality [62],[1]. The main motivation behind this technology is to increase the safety of both
driver and other traffic participants. In this context, pedestrian protection systems have become
a necessity. But merely passive components like airbags are not enough: active safety, technology
assisting in the prevention of a crash, is vital. For this, a system of pedestrian detection and
classification plays a fundamental role.

Challenges

Pedestrian detection and classification in the context of intelligent vehicles in an urban environment
poses a lot of challenges:

Pedestrian Appearance and Shape.   By nature, the humans have different heights and body
shapes. But this variability in appearance is further increased by different cloth types. Moreover,
human shape can change a lot in a short period of time (for example a person that bends to
tie its shoes). Also the appearance depends on the point of view of the camera, as well as the
distance between the camera and the pedestrian. Close pedestrians can bear little resemblance
with the ones situated far away.

Occlusion.   Occlusions represents an important challenge for the detection of any type of object,
and in the case of pedestrians they can be divided into: self and external occlusions. Self-occlusion
are cause especially by the pose of the object, in the case of a pedestrian that has a side-way
position in relation with the point of view of the camera will certainly exhibit occlusion of some
body-parts. Moreover different objects carried by the pedestrians might have the same effect (for
example hats, bags, umbrellas). In the external occlusions category we include other pedestrians

15

(especially in an urban situation), poles, other cars, as well as the situation in which the pedestrian is too close to the camera leading certain body-parts exit the field of view.

Environmental conditions. Although some meteorological circumstances might not have a direct impact on the quality of images (for example light rain), they can influence the appearance of pedestrians for cameras (for example a passer-by can open an umbrella which might lead to occlusion of the head region). Other conditions might lead to situations where the quality of retrieved images is altered (for example situations of haze, fog, snow, heavy rain etc.). Another factor that should be taken into consideration is the time of day, that has a direct impact over the amount of ambient light available - usually, during daytime the problem of pedestrian detection and classification poses less problems than during night.

Sensor choice. Each existing sensor has certain disadvantages and advantages, depending on the situation. For example, passive sensors like visible cameras can be affected by low light conditions, giving poor images with low variation in intensity across objects and background, while thermal cameras might experience the same problems when the environment has a similar temperature with the pedestrians. Active sensors, like LIDAR, have the advantage of providing distance to all objects in a scene, but they have as output a large datasets that might be difficult to interpret.

Other objects. Distinction between non-pedestrians and pedestrians might not be always simple, being difficult to construct a model that differentiates between pedestrians and any other existing objects.

Main Research Contributions

Motivated by the importance of pedestrian detection, there exist an extensive amount of work done in connection with this field. *Our objective is to study the problem across different light spectrum and modalities, with an emphasis on disparity map.*

Our main contributions can be summarised as follows:

- Creation and annotation of two databases for benchmarking of pedestrian classification, one for Far-Infrared (FIR) and the other one in Short-Wave Infrared (SWIR).

- In the context of Thermal images, we have proposed a new feature, Intensity Self Similarity (ISS). The performance of ISS was compared on three different datasets with state of the art features.

- As a novelty, we have studied the SWIR spectrum for the task of pedestrian classification, and we have performed a comparison with the Visible domain.

- As a low cost solution, we believe that Stereo Vision is a promising alternative. In this context, we have also focused on improving Stereo Matching algorithm by proposing new cost functions.

- We have studied the performance of different features across different domains (Visible, FIR) and across multiple modalities (Intensity, Motion, Disparity map)

Thesis Overview

This thesis is organized as follows (see also figure 1):

Chapter 1 presents an in-depth analysis for the motivation of a pedestrian detection system, along with an overview of existing types of sensors. Our sensor of choice is passive sensors represented by cameras sensitive to different light spectrums: Visible, Far Infrared and Short Wave Infrared. We present also a short review of the steps employed in the task of pedestrian classification and detection with an emphasise on the step of feature computation.

In **Chapter 2** we study the problem of pedestrian classification in Thermal images (Far-Infrared Spectrum). After overviewing existing datasets of Thermal images, we have reached the conclusion that they all have important disadvantages: either the quality of the thermal images is poor and there is not possibility of direct comparison with the Visible spectrum; or the datasets are not publicly available. In this context, we have acquired and annotated a new dataset. Moreover we have proposed a feature adapted for pedestrian classification in Far-Infrared images and compared it with other state of the art features, in different conditions.

A new spectrum that can be interesting for the task of pedestrian detection and classification is the Short-Wave Infrared (SWIR). An analysis of this light spectrum is made in **Chapter 3**. After having performed some preliminaries experiments on a restricted dataset, we have acquired and annotated a dataset of SWIR images, along with the Visible correspondent. On this later dataset, we have compared the two spectrums from the perspective of different features.

Infrared cameras represent an interesting alternative to Visible cameras, and in general with better results, but remains an expensive one. In this context, StereoVision could improve the results obtained by just the employment of Visible cameras. **Chapter 4** deals with the algorithms of Stereo Matching. We propose several improvements for this algorithm, that mostly focus on the employed cost function.

Chapter 5 treats the problem of multi-modality pedestrian classification (Intensity, Depth
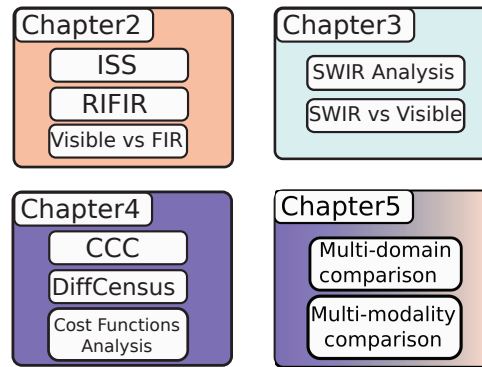
Figure 1: Thesis structure
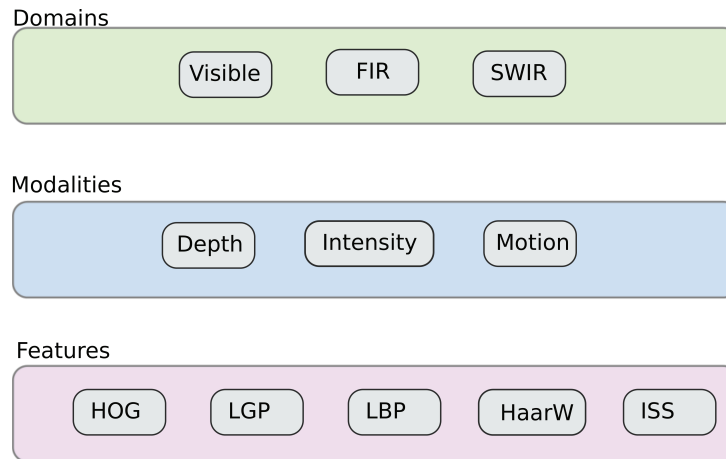
Figure 2: Domain-modality-feature relationship

and Optical Flow) in both Visible and FIR spectrum. In figure 2 is presented the difference between the domains and modalities employed. Moreover we show a preliminary analysis of the impact of the quality of the Disparity Map over the results of classification. Finally, conclusions and future work are presented in **Chapter 6**.

List of articles

Journal Papers

- **Alina Miron**, Samia Ainouz, Alexandrina Rogozan, Abdelaziz Bensrhair, *"A robust cost function for stereo matching of road scenes"*, Pattern Recognition Letters, No. 38, (2014): 70-77.

- **Alina Miron**, *"Post Processing Voting Techniques for Local Stereo Matching"*, Studia Univ. Babes-Bolyai, Informatica, Volume LIX, Number 1, (2014): 106-115

- **Alina Miron**, Samia Ainouz, Alexandrina Rogozan, Abdelaziz Bensrhair, *"Cross-comparison census for colour stereo matching applied to intelligent vehicle."*, Electronics

Letters 48.24 (2012): 1530-1532.

- **Alina Miron**, Samia Ainouz, Alexandrina Rogozan, Abdelaziz Bensrhair, Horia F. Pop, *"Stereo Matching Using radiometric Invariant measures"*, Studia Univ. Babes-Bolyai, Informatica, Volume LVI, No.3, (2011): 91-96.

Conferences

- Fan Wang, **Alina Miron**, Samia Ainouz, Abdelaziz Bensrhair, *Post-Aggregation Stereo Matching Method using Dempster-Shafer Theory*, IEEE International Conference on Image Processing 2014 (accepted)

- **Alina Miron**, Rean Isabella Fedriga, Abdelaziz Bensrhair, and Alberto Broggi, *SWIR Images Evaluation for Pedestrian Detection in Clear Visibility Conditions*, Proceedings of IEEE ITSC (2013): 354-359

- Massimo Bertozzi, Rean Isabella Fedriga, **Alina Miron**, and Jean-Luc Reverchon, *Pedestrian Detection in Poor Visibility Conditions: Would SWIR Help?*, IEEE ICIAP (2013): 229-238

- **Alina Miron**, Bassem Besbes, Alexandrina Rogozan, Samia Ainouz, Abdelaziz Bensrhair, *Intensity Self Similarity Features for Pedestrian Detection in Far-Infrared Images*, IEEE Intelligent Vehicle Symposium (2012): 1120-1125

- **Alina Miron**, Samia Ainouz, Alexandrina Rogozan, Abdelaziz Bensrhair, *Towards a robust and fast color stereo matching for intelligent vehicle application*, IEEE International Conference on Image Processing (2012): 465-468

Presentations

- One Day BMVA Symposium at the British Computer Society: *"Stereo Matching using invariant radiometric features"*, London, May 18th 2011

- Journee GdR ISIS, Analyse de scenes urbaines en image et vision, *"Stereo-vision for urban scenes."*, Nov. 8th 2012, Paris

1

Preliminaries

Contents

1.1 Motivation

As shown in a report published by World Health Organization from 2013 [104], it is estimated that every year 1.24 million people die as a result of a road traffic collision. That means that over 3000 deaths occur each day. An additional 20 to 50 million[1] more people sustain non-fatal injuries from a collision, leading the traffic collision to be also one of the top causes of disability worldwide.

---

[1]Non-fatal crash injuries are insufficiently documented

Road traffic injuries are the eight leading cause of death globally, among the three leading causes of death for people between 5 and 44 years of age and the first cause of death for people aged $15 - 19$. Another sad statistic is that road crashes kill 260 000 children a year and injure about 10 million (join report of Unicef and the World Health Organization). Without any action taken, road traffic injuries are predicted to become the fifth leading cause of death in the world, reaching around 2 million deaths per year by 2020. The main cause of the increase in number of deaths is caused by a rapid increase in motorization without sufficient improvement in road safety strategies and land use planning. The economic consequences of motor vehicle crashes have been estimated between 1% and 3% of the respective GNP[2] of the world countries, reaching a total over \$500 billion.

Analysing the casualties worldwide by the type of road user shows that almost half of all road traffic deaths are among vulnerable road users: motorcyclists (23%), pedestrians (22%) and cyclists (5%). An additional 31% of deaths are represented by car occupants, while for the extra 19% there doesn't exist a clear statistic of the road user type.
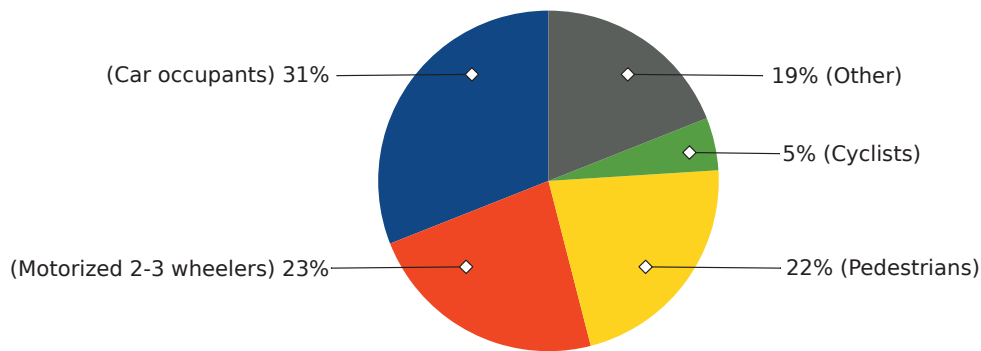
Figure 1.1: Road traffic casualties by type of road user

Action must be taken on several levels and that is why, in March 2010 the United Nations General Assembly resolution 64/255 proclaimed a Decade of Action for Road Safety 2011–2020 with a goal of stabilizing and then reducing the forecasted level of road traffic fatalities around the world by increasing activities conducted at national, regional and global levels. There exist five pillars to implement different activities: *Road safety management, Safer roads and mobility, Safer vehicles, Safer road users* and *Post-crash response.*

Five key safety risk factors have been identified as speed, drink-driving, helmets, seat-bels, and child restraints. For short term the way to address the problem of road collisions is better legislation addressing these key factors. If all the countries would pass comprehensive laws, according to [104], the number of world wide road casualties would decrease to a total of around 800 000 per year. Therefore along a legislation that address key problems of road safety,

---

[2]Gross Net Product

infrastructure and vehicle manufactures should follow along.

Because human factor is the leading cause of traffic accidents [50], contributing wholly or partly for around 93% of crashes (see figure 1.2), we consider that for long term, Advanced Driver Assistance Systems (ADAS) will play a key role in reducing the number of road accidents.
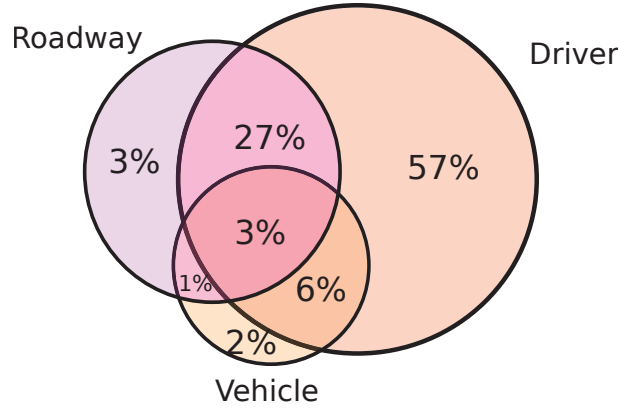
Figure 1.2: Causes by percentage of road accidents (in USA and Great Britain)

Autonomous intelligent vehicles could represent a possible solution to the problem of traffic accidents, having the capability in a lot of situations to react faster and being more effective, due to possible access to multiple sources of information (given by different sensors, but also by vehicle-to-vehicle communication). Moreover intelligent vehicles could have further benefits like reducing traffic congestions, higher speed limit or relieving the vehicle occupants from driving. But all these will be feasible only the moment when the vehicles become reliable enough.

Furthermore, in intelligent transportation field, the focus on passenger safety in human-controlled motor vehicles has shifted, in recent years, from *collision mitigation systems*, such as seat belts, airbags, roll cages, and crumple zones, to *collision avoidance systems*, also called Advanced Driver Assistance Systems (ADAS). The latter includes adaptive cruise control, lane departure warning, traffic sign recognition, blind spot detection, among others. If the collision mitigation systems seek to reduce the effects of collisions on passengers, ADAS systems seek to avoid accidents altogether.

In this context, it is imperative for the vehicles (both autonomous and human-controlled) to be able to detect other traffic participants, especially the vulnerable road users like pedestrians.

1.2 Sensor types

Choosing the right sensor for an object detection problem is of paramount importance. The right choice can have a huge impact over the ability of the system to perform robustly in different situations and environments.

Frequency (Hz)

10^{24} 10^{22} 10^{20} 10^{18} 10^{16} 10^{14} 10^{12} 10^{10} 10^{8} 10^{6} 10^{4} 10^{2} 10^{0}

| Gamma rays | X-rays | UV | Visible | Infrared | Micro wave | FM | AM Radio waves |

10^{-16} 10^{-14} 10^{-12} 10^{-10} 10^{-8} 10^{-6} 10^{-4} 10^{-2} 10^{0} 10^{2} 10^{4} 10^{6} 10^{8}

Wavelength (m)

| NIR | SWIR | MWIR | LWIR | FIR |

0.7 1.4   3   8   15   1000 µm
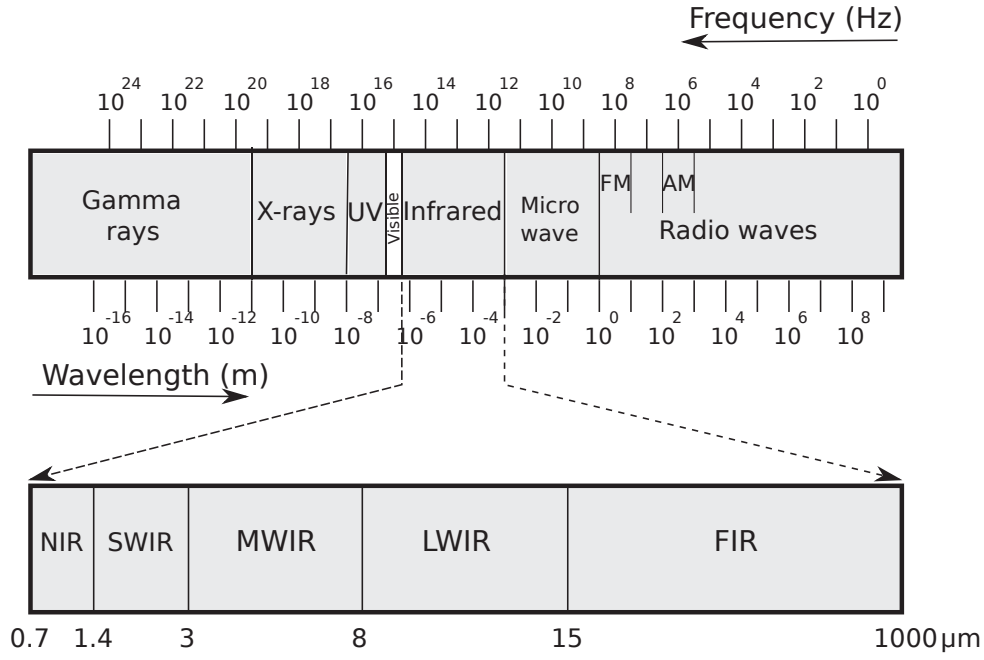
Figure 1.3: Electromagnetic spectrum with detailed infrared spectrum.

Because pedestrian detection is a challenging problem that has applications not only in the field of intelligent vehicles but also for computer interaction or surveillance systems, different sensor types have been taken into consideration for the information acquisition from the environment.

In table 1.1 there are presented different camera types, like webcams, mono-visible cameras, stereo cameras or infrared cameras, with advantages and disadvantages. Moreover, in table 1.2 are presented some of the complementary sensors.

Testing all sensors types might prove difficult, therefore, due to convenience (access, databases, low-sensor cost, wide applicability), we are going to explore just the use of passive sensors (i.e. cameras) for the task of pedestrian detection and classification. We are going to analyse Visible spectrum (i.e. range 0.4-0.75 μm) with emphasises on the use of depth information obtained from Stereo Vision, Short-Wave Infrared and Far Infrared (i.e. range 8-15 μm). In figure 1.3, for reference, is presented the electromagnetic spectrum. In literature, in the context of cameras, the range 8-15 μm is referred either as Long-Wave Infrared or Far Infrared. Thus, throughout this thesis we are going to use these terms interchangeably.

1.3 A short review of Pedestrian Classification and Detection

There is a significant amount of existing works in the domain of pedestrian classification. Recent surveys compare different algorithms and techniques. Gandhi and Trivedi [54] present a review of pedestrian safety and collision avoidance systems, that includes infrastructure enhancements. They classify the pedestrian detection approaches according to type and sensor configurations.

Table 1.1: Review of different camera types

Camera Type	Pros	Cons
Webcam - RGB • *Connection type*: USB 2, USB 3, IEEE 1394 (rare) • *Resolution range:* usually @30fps 640x480	• Cheap; Easy to find; Simple to use • Widely supported by different software environment	• Usually poor image quality, especially in low light • Difficult to change camera settings • Typically fixed lens • Problems can be experienced when functioning for extended periods of time
Mono-Visible Cameras (CCD and CMOS) • *Connection type*: USB 2, USB 3, GigE, IEEE 1394	• High resolution at high frame rate is possible • Interchangeable lens to suit different applications • Camera designed for long time functioning • Main types of cameras used	• In night time, or difficult weather conditions the camera performance can drop • Depending on the application, without any depth information, the computation time could increase well beyond real-time • Software integration could be difficult because each type of camera comes with it's specific drivers that are platform dependent
Stereo Vision Cameras	• Same advantages like the Mono-Visible Cameras • Extra information provided by the computed depth can give essential information about the scene	• Same disadvantages like Mono-Visible Cameras • Depending on the stereo vision algorithm used and the quality desired for the disparity map, computation time could increase a lot
Near-Infrared Cameras	• Generally the same resolution like visible cameras • They capture light that is not visible to human eye • Low cost compared with other infrared cameras • Can be used very low-light	• Monochrome; • They require infrared light, and to be used in low light situations an IR emmiter • Sensitivity to sunlight
Far-Infrared Cameras	• Generally the same resolution like visible cameras • They capture the thermal information from the environment • Will work in very low-light conditions without any additional emitter • Robust to daytime and night time, especially for people detection	• High-cost • Can't see through glass, therefore for an application ADAS they must be mounted outside the vehicle. • The integration could be difficult, due to custom electronics or capture hardware

Table 1.2: Review of other types of sensors

Sensor Type	Pros	Cons
Depth Cameras		
• They belong in fact to the IR cameras category in the sense that there exist an infrared light projection that is used to construct a depth image using structured light or time-of-flight.	• They have all the advantages of stereo-cameras • Depth image is constructed without the need of a stereo-matching algorithm, thus high frame rate is obtained	• Small range of effectiveness • Shiny surfaces are not detected or can cause strange artifacts • Sensitivity to sunlight, therefore not suitable for outside use
Radar		
• Transmits microwaves in pulses that bounce off any object in the path, thus being able determine distance to objects	• Fairly accurate in determining the distance to objects	• Low spatial resolution therefore it is not practical for detecting the type of object
LIDAR		
• Works by projecting optical laser light in pulses and analysing the reflected light	• Is the most effective way of getting a 3D model of the environment • High resolution depth image; Fast acquisition	• High cost • Very large datasets might prove difficult to interpret

Geronimo et al. [58] also survey the task of pedestrian detection for ADAS, but they choose to define the problem by analysing each different processing step. These surveys are an excellent source for reviewing existing systems, but sometimes it is difficult to actually compare the performance of different systems.

In this context, a few surveys try to make a direct comparison of different systems (features, classifier) based on Visible images. For example, Enzweiler and Gavrila [39] cover the components of a pedestrian detection system, but also compare different systems (Wavelet-based AdaBoost, histogram of oriented gradient combined with an SVM classifier, Neural Networks using local receptive fields and a shape-texture model) on the same dataset. They conclude that the HOG/SVM approach outperformed all the other approaches considered. Enzweiler and Gavrila [40] compare different modalities like image intensity, depth and optical flow with features like HOG, LBP and they conclude that multi-cue/multi-feature classification results in a significant performance boost. Dollar et al. [36] proposed a monocular dataset (Caltech database) and make an extensive comparison of different pedestrian detectors. It is showed that all the top algorithms use in one way or another motion information.

In this section we will just provide a short overview of the components that take part of most of the pedestrian classification and detection systems.

A simplified architecture of a pedestrian detection system can be split into several modules (as presented in Figure 1.4): preprocessing, hypothesis generation and object classification/hypothesis refinement. Although several more modules could be added, like Segmentation or Tracking, we believe the three modules to be essential for the task. Furthermore, feedback loops between modules could be added in order to have a higher precision.

1.3.1 Preprocessing

This module contains functions like exposure time, noise reduction, camera calibration etc. Most existing approaches can be divided into monocular-based or stereo-based.

In case of monocular cameras, a few approaches undistort the images by computing the intrinsic camera parameters [57]. Nevertheless, most of the existing datasets that benchmark pedestrian detection and classification algorithms, do not provide camera intrinsic parameters or undistorted images [36],[30].

In case of stereo-based systems, camera calibration of both intrinsic and extrinsic is usually a requirement for the stereo-matching algorithm. Most of the systems will assume a fixed position of the cameras and will therefore use just once the calibration checkboard. Other systems, take into consideration the fact that the cameras relative position could be changed, therefore they propose to continuously update extrinsic parameters [23].

1.3.2 Hypothesis generation

Hypothesis generation, also referred as candidate generation or determining Regions of Interest (ROI) , has the purpose of extracting possible areas where a pedestrian might be found in the image.

An exhaustive method is that of using a sliding window. A fixed window is moved along the image. In order to detect pedestrians of different sizes, the image will be resized several times and then it is parsed again. In the next module (object classification), each window is separately classified into pedestrian/non-pedestrian. This technique will result in a high coverage by assuring that every pedestrian in the image is contained in at least one window. Nevertheless, it has several drawbacks. One disadvantage is the high number of hypothesis generating, thus a high processing time. Moreover, many irrelevant regions, like that of sky, road, buildings are parsed, usually leading to an increase in the number of false positives.

In monocular systems, other approaches perform image segmentation by considering color distribution across the image or gradient orientations. In case of Far-Infrared images, intensity threshold is a widely used technique, along with other methods like Point-of-Interest (POI)

Preprocessing

- Noise reduction
- Image undistortion/ Image calibration (StereoVision)
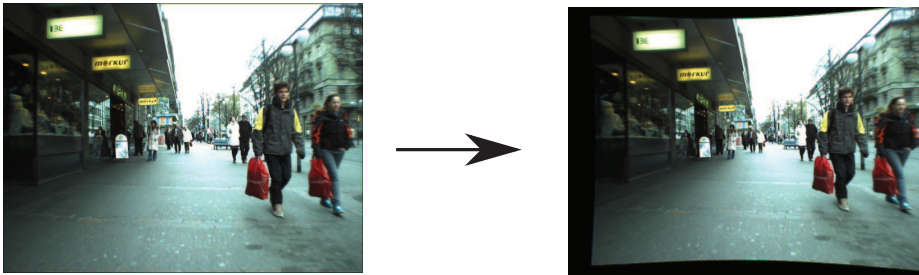
Hypothesis Generation

Sliding Window/ Pyramid resizing

Disparity Map Hypothesis generation

Disparity Map computation → Ground Removal → Obstacle Detection
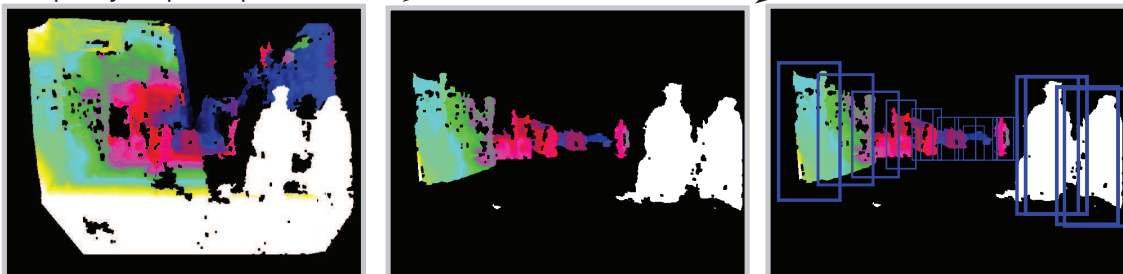
Classification/ Hypothesis Refinement

Hypothesis → Classification → Refinement
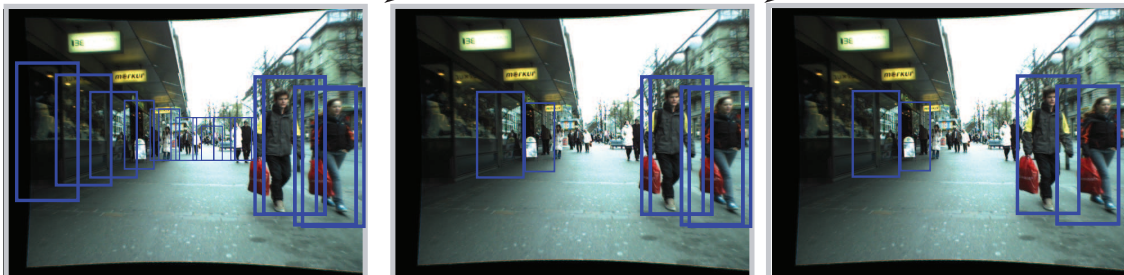
Figure 1.4: A simplified example of architecture for pedestrian detection

extraction.

In stereo-based systems, computation of disparity map provides valuable information. Techniques like stixels computation [8] or ground removal followed by determining objects above a certain height from disparity maps [79], reduce the search space by up to a factor of 45 [9].

1.3.3 Object Classification/Hypothesis refinement

This module, usually, will take as input a list of ROIs generated in the previous step, and will classify them in pedestrian/non-pedestrian (in order to reduce the false positive rate). For this, different features are computed like: silhouette matching [55],[22], appearance features computed using a holistic approach (Histogram of Oriented Gradients [30], HAAR wavelets [106], Haar-like features [126], Local Binary Patterns [100] etc.) or by modelling different body parts using different appearance features. These features are used to learn a classifier like Support Vector Machine [29], AdaBoost [52], Artificial Neural Networks [139] among others.

AdaBoost (Adaptive Boosting) is a machine learning algorithm that combines several weak classifiers into a weighted sum. Contrary to SVM and Artificial Neural Networks, AdaBoost selects only those features that have proven to improve the classification model. Because irrelevant features do not need to be calculated, this will reduce the feature dimensionality and running time. The main disadvantage of AdaBoost is that is susceptible to overfitting more than other classification algorithms. It might also prove sensitive to noisy data and outliers.

Artificial Neural Networks is a machine learning algorithm inspired by the brain system. The classifier is a simple mathematical model that works by constructing neurons (nodes) organized in layers and connected by weighted *axons* (lines). Even though the model might be simple, the main advantage of artificial neural networks is that they can learn complex patterns, even from incomplete or noisy data. Neural networks require usually extensive learning times, the output error might depend on the chosen architecture. A complex model can be used to learn complex tasks, but overly complex models tend to lead to problems with learning.

SVM Classifier. Support Vector Machine is a supervised learning technique that constructs a hyperplane in a high dimensional space using a relatively few training examples. Over-fitting might be avoided by optimising the regularisation parameters, while expert knowledge about the problem can be built by optimising the kernel used.

The optimal hyper-plane (see figure 1.5) is used to classify an unlabeled input data X by using a decision function given by

$$f(X) = sign(\sum_{X_i \in SV} (y_i \alpha_i K(X_i, X) + b)) \tag{1.1}$$
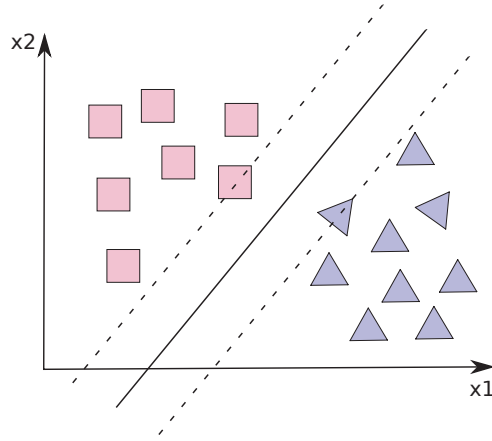
Figure 1.5: For a SVM trained on two-class problem, it is shown the maximum-margin hyperplane (along with the margins)

where SV is the set of support vector items X_i, b is the offset value, K is the kernel function and α_i are the optimized Lagrange parameters.

In this thesis, we have chosen to work only with Support Vector Machine classifier, due to fast training and testing time. There exist different types of kernel functions that could be used with the SVM. Among them, we have chosen to perform experiments with the Linear kernel for a fast classification step.

In the next section we are going to present some of the significant features that are going to be used across this thesis.
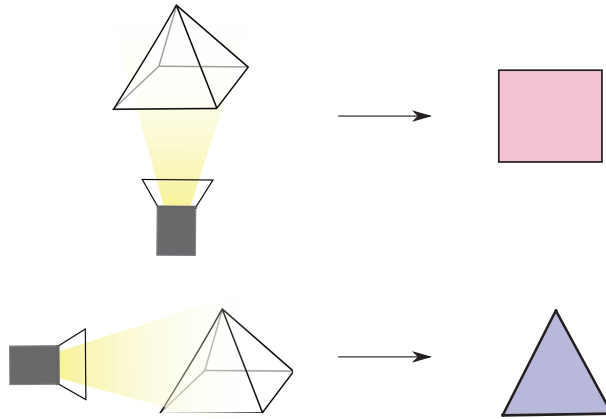
Figure 1.6: A pyramid as seen from two points of view

1.4 Features

Features, in the context of computer vision, represent different attributes or aspects of a particular image. For example, in figure 1.6 is presented how a pyramid is seen from two different points of view. In the same way, different features will ideally reveal various information about the image.

In recent years, a large amount of features were developed. In what follows, we are going to present a few features that are either widely used, or represent a reference point in literature, and will be further used in various chapters of the thesis.

1.4.1 Histogram of Oriented Gradients (HOG)

Gradient based features have become very popular due to the robust results obtained in both the sparse version (Scale Invariant Feature Transformation - SIFT [89]) and dense representation (Histogram of Oriented Gradients - HOG [30]). HOG represents, currently, a state of the art feature for pedestrian classification.

Local object appearance can be well characterised by the distribution of local intensity gradients or edge directions. In the case of HOG, this is performed dividing the image into small *cells*. For each cell a 1-D histogram is constructed containing the gradient orientations. By normalising the obtained histogram inside bigger regions called *blocks*, it is obtained a better invariance to illumination conditions. The final feature vector is constructed by the simple concatenation of the computed histograms. In figure 1.7 are presented the main steps for computation of HOG features.

1.4.2 Local Binary Patterns (LBP)

In comparison with HOG, that is used to capture edge or local shape information[100], local binary pattern (LBP) operator is a texture descriptor that is widely used due to its invariance to gray level changes.

There exist different methods to compute LBP, varying by different choice of parameters. In order to compute the LBP operator we use the method described by Wang et al. [131], because has proven to be one of the most robust. In a formal manner the operator can be described by equation 1.2.

$$LBP_{p,r}(c) = \sum_{i \in N_{p,r}(c)} s(I_i - I_c) * 2^p \tag{1.2}$$

where p is the number of pixels in a considered neighbourhood, r is the radius of the neighbourhood, c are the coordinates of the central pixel, $N_{p,r}(c)$ represents the set of coordinates for the pixels found at radius r from the central pixel, and $s(x)$ is defined by equation 1.3.
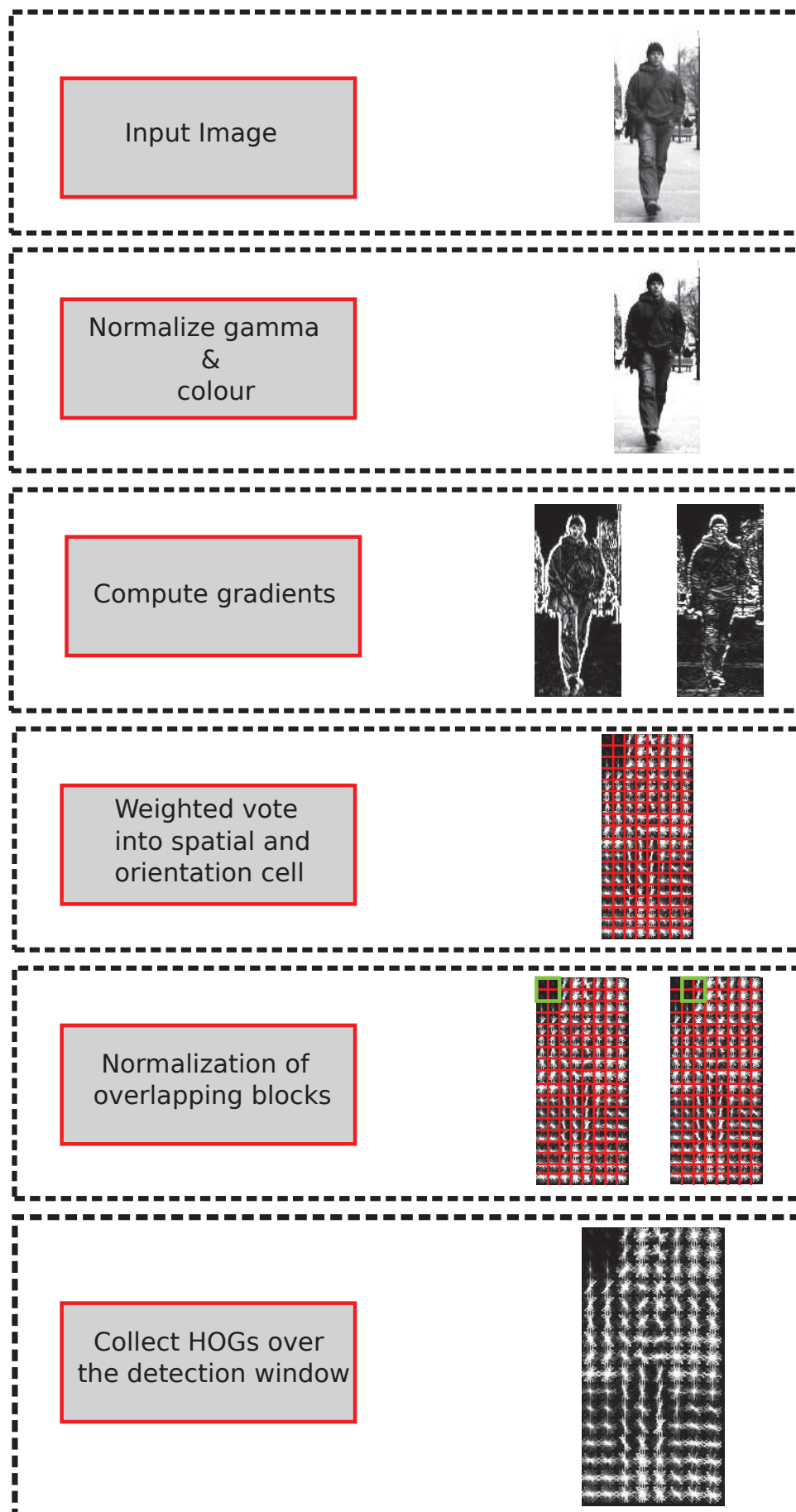
Figure 1.7: HOG Feature computation

$$s(x) = \begin{cases} 1, & \text{if } x \geq 0 \\ 0, & \text{otherwise} \end{cases} \tag{1.3}$$

| p=8, r=1 | p=12, r=2 | p=16, r=4 |
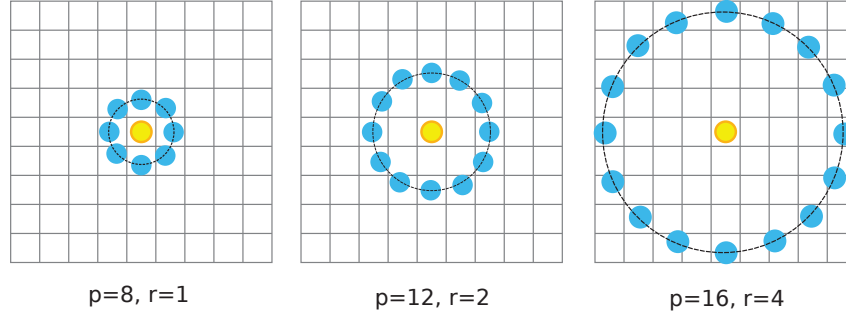
Figure 1.8: Examples of neighbourhood used to calculate a local binary pattern, where p are the number of pixels in the neighbourhood, and r is the neighbourhood radius

The main steps to compute LBP are:

- Like in the case of HOG, the ROI is divided into cells of 8×8 pixels.

- Each pixel in a given cell is compared with the pixels in a considered neighbourhood and a bit-string is constructed. This vicinity region is usually considered a circle as shown in figure 1.8.

- The bit-string has the same length as the number of pixels in the neighbourhood, and is constructing by comparing the value of a pixel with the pixels in the vicinity. If the center pixel's value is smaller than the neighbour's value , then in the bit-string a "1" will be written, otherwise a "0", like showed in figure 1.9. Because in this approach a large number of patterns can be created that could introduce noise in the classification process, only the uniform patterns are considered. A uniform pattern, as seen in figure 1.10, is defined by those pattern that lead to a maximum of two 0-1 transitions.

- In the following step, over each cell, a histogram is computed based on the decimal valued of transformed bit-string.

- The histograms of all cells are concatenated and normalised. This gives the final feature vector for the considered window.

1.4.3 Local Gradient Patterns (LGP)

LBP features are sensitive to local intensity variations and therefore could lead to many different patterns in a small region. This might affect the performance of some classifiers. To overcome
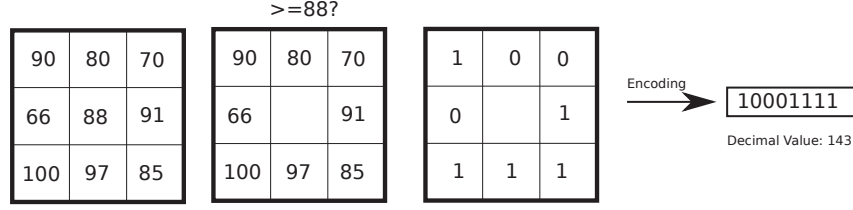
Figure 1.9: Local binary pattern computation for a given pixel. In this example the pixel for which the computation is performed is the central pixel having the intensity value 88.
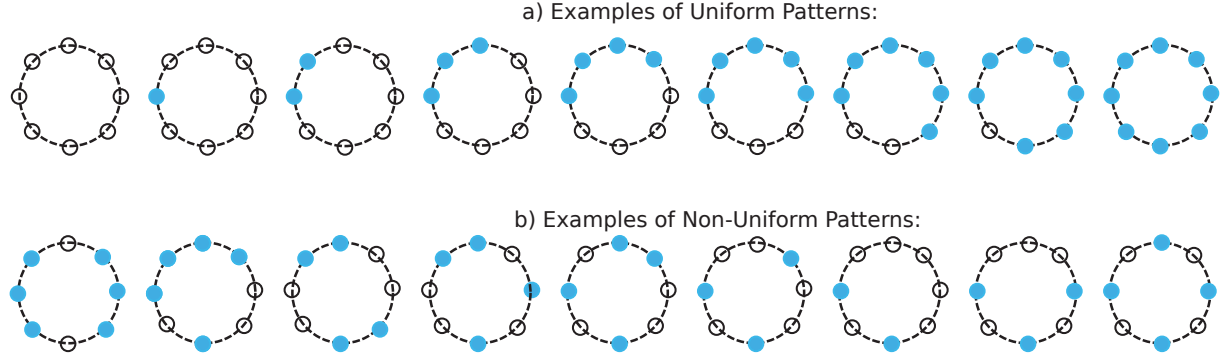
Figure 1.10: Examples of Uniform (a) and non-uniform patterns (b) corresponding for LBP computed with $r = 1$ and $p = 8$. There exist a total of 58 uniform local binarry pattern plus one(for others)

this, Jun et al. [72] proposed a novel representation called Local Gradient Patterns (LGP).

$$LBP_{p,r}(c) = \sum_{i \in N_{p,r}(c)} s(G_i - \overline{G}) * 2^p \tag{1.4}$$

where gradient s is defined in equation 1.3, G_p is defined in 1.5 as the absolute difference between the central pixels intensity I_c and its neighbouring pixel I_i, and $\overline{G}$ is defined in equation 1.6

$$G_i = |I_i - I_c| \tag{1.5}$$

$$\overline{G} = \frac{1}{p} \sum_{n=0}^{p-1} G_n \tag{1.6}$$

This operator is computed in a similar manner as LBP. Instead of working on intensity values of the pixels, it employs gradient values of the neighbourhood pixels (see equation 1.4). The gradient is computed as the absolute value of intensity difference between the given pixel and its neighbouring pixels. The central pixel value is replaced by the average of gradient values (see figure 1.11).
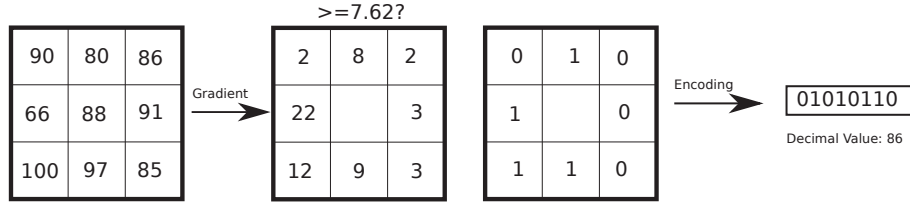
Figure 1.11: Local gradient pattern operator computed for the central pixel having the intensity *88*.

1.4.4 Color Self Similarity (CSS)

Recent work has shown that local low-level features are particularly efficient ([34], [132]). In [127] a new feature (*CSS*), is proposed for images in the visible spectrum, based on second order statistics of colors. This method takes advantage of locally similar colors within an analysis window.

This window is first divided into blocks of 8×8 pixels. For a given color space, like RGB and HSV, a histogram with $3 \times 3 \times 3$ bins is computed for each block. Every block is then compared to all others blocks using histogram intersection resulting in a vector of similarities. Finally, a L2-normalization is applied to that similarity vector.

1.4.5 Haar wavelets

Haar wavelets were introduced by Papageorgiou and Poggio [106]. The idea behind this type of features is to compute the difference between the sum of intensities in two rectangular areas in different configurations and sizes (see figure 1.12.a),1.12.b), 1.12.c)). These were extended by Viola et al. [126]. They introduced two new configurations for the rectangular areas (see figure 1.12.d), 1.12.e)) and also proposed a classifier based on layers of weak classifiers (AdaBoost).

1.4.6 Disparity feature statistics (Mean Scaled Value Disparity)

A feature that is interesting from the perspective of using disparity map, is the disparity feature statistics proposed by Walk et al. [128].

The main idea behind these features is that even if the heights of pedestrians are not identical, they are still very similar. The disparity statistics proposed in [128] are based on the invariant property of disparity map, that the ratio of disparity and observed heigh is inversely proportional to the 3D object height.

In order to make the disparity statistics features independent of the distance to the object, in a scenario of sliding window search, the disparity values are divided by the appropriate scale level
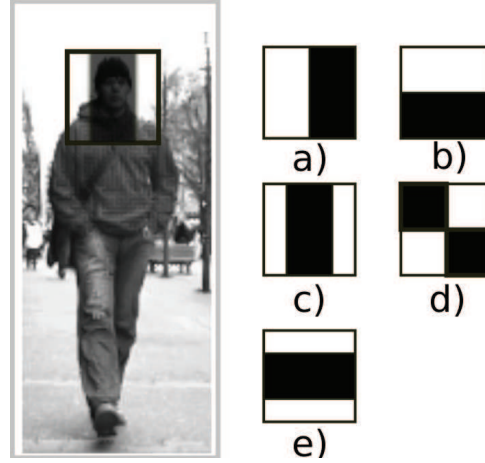
Figure 1.12: Haar wavelets a),b),c) and Haar-like features d),e). The sum of intensities in the white area will be subtracted from the sum of intensities of the black area.

of the image pyramid. The next step is to divide the considered window for classification into cells of 8×8 pixels, like performed for HOG and LBP. The mean value of the scaled disparities is computed for each cell, and the final feature vector is obtained by concatenating the mean values computed across all cells. Because other statistics could be computed on the disparity map, we will name in what follows these features **Mean Scaled Value Disparity (MSVD)**.

1.5 Conclusion

In this chapter we have presented an overview of the pedestrian detection and classification sensors and systems. For the final experiments performed in this thesis we have chosen to work with three different types of cameras: FIR, SWIR and Visible. Accordingly, in the following chapter, we treat the problem of pedestrian classification in FIR spectrum.

2

Pedestrian detection and classification in Far Infrared Spectrum

Contents

In this chapter, we study the pertinence of using a monocular FIR camera for the task of pedestrian detection and classification. In recent years, the cost of infrared (IR) cameras has decreased, making them an interesting alternative to visible cameras for pedestrian detection systems ([10], [134], [115], [86]). Moreover, infrared cameras still provide pertinent and discriminative information even in difficult illumination conditions (i.e. night, fog) and they are less prone to confusion caused by colors, textures and shadows belonging to objects other than pedestrians.

Although there exists different IR sensors characterized by their wavelength, FIR camera seems to be the most suitable for distinguishing hot targets like pedestrians. This ability represents an advantage of FIR cameras over visible ones, especially during the night. Despite this, pedestrian detection in IR images remains a challenging task, because the system has to deal not only

37

with the problem of their variability in posture, range, orientation, but also with the lack of texture information. Therefore, texture can be an advantage, due to less distractions in the image, and disadvantage, due to less information available. Another challenge is that objects other than pedestrian, like vehicles, animals, electricity sources, appear also as hot targets in the FIR spectrum.

2.1   Related Work

Usually, the sliding window technique, mostly used in the Visible domain, is not suitable for real-time object detection application that uses a complex classifier. In response to this, Infrared domain offers the possibility of generating a smaller number of hypothesis to be tested, therefore becoming an interesting alternative to the Visible spectrum. Moreover, thermal Infrared has a clear advantage over Visible spectrum during the night, where it can still provide relevant information about the environment.

For Region of Interest (ROI) generation in FIR images a natural solution would be to use a threshold, like in [115], or even better an adaptive threshold by assuming that non-pedestrian intensities follow a Gaussian distribution [13]. Unfortunately, the problem of estimating an appropriate threshold remains a key issue because the pedestrian intensities vary with respect to range and outside temperature.

Erturk [42] presents a region of interest extraction in infrared images based on one-bit transform. Potential interest regions are obtained by using a target mask, followed by a comparison of the original image histogram with the masked image histogram in order to obtain an automated threshold value. This method was tested only on static images and is not followed by a classification step.

Kim and Lee [73] present a region of interest generation method specialized for nighttime pedestrian detection using far-infrared (FIR) images. They respond to the problem of finding a good intensity threshold, by working with image segments and also using the low-frequency characteristics of the FIR images.

Wang et al. [129] try to improve the local contrast between targets and background in the static infrared images, by proposing a background model. In the same time to filter the false negatives a ramp loss function is used to learn the characteristics of a pedestrian. Liu et al. [88] use a pixel-gradient oriented vertical projection approach in order to estimate the vertical image stripes that might contain pedestrians. Afterwards, a local thresholding image segmentation is adopted to generate ROIs more accurately within the estimated vertical stripes.

Other approaches consists in detecting warm symmetrical objects with specific size and aspect

ratio [18], or in detecting pedestrian heads based on pixel classification [16],[94].

For the pedestrian classification step there exist different approaches that are based on global or region object representation. Bertozzi et al. [13] presents a validator stage for a pedestrian detection system based on the use of probabilistic models for the infrared domain. Four different models are employed in order to recognize the pose of the pedestrians; open, almost open, almost closed and fully closed legs are detected. Nanda and Davis [98] use probabilistic templates to capture the variations in human shape specially for the case where the contrast is low and body parts are missing. Unfortunately, techniques based on symmetry verification or template matching are not precise enough for the task of pedestrian detection. The global features that include gray level features [117] and Gabor wavelets [3], are computed over all the pixels within a Bounding Box (BB). Region-based features, like Haar wavelets [2] and Histogram of Oriented Gradients (HOG) [115],[138] encode the influence of each pixel that lies in a BB.

Kim et al. [74] propose a modified version of the well-known HOG descripor, called historgram of local intensity differences that claim it is more suited for FIR images in terms of both accuracy and computation efficiency. Sun et al. [118] propose the use of Haar-like features in combination with AdaBoost in order to detect pedestrians during the night. Also a pedestrian classification system based on AdaBoost and a combination of Haar and ad-hoc-features is proposed by Cerri et al. [27]. They test the system in the context of using NIR illuminators.

Li et al. [85] propose a feature based on local oriented shape context (LOSC) descriptor also for nighttime pedestrian detection. They based their approach on a shape context descriptor that is enhanced with edge's orientation.

Zhang et al. [138] investigate the methods derived from visible spectrum analysis for the task of human detection. They extend two feature classes (edgelets and HOG features) and two classification models(AdaBoost and SVM cascade) to the FIR images. Zhang et al. [138] concludes that it is possible to get detection performance in FIR images that is comparable to state-of-the-art results for visible spectrum images on a dataset of around 1000 pedestrians.

Mählisch et al. [91] proposed a detector approach for low-resolution FIR images based on a hierarchical contour matching algorithm and a cascaded classifier approach.

In order to take advantage of some properties of infrared images, Fang et al. [45] introduce a projection feature for segmentation (in order to avoid shape-template and pyramid searching) and two-axis pixel-distribution (histogram and inertial) feature for classification.

Krotosky and Trivedi [80] present an interesting analysis of Color-, Far-Infrared-, and multimodal-stereo approaches to pedestrian detection. They design a four-camera experimental testbed consisting of two color and two infrared cameras for capturing and analysing various

configuration permutations for pedestrian detection, thus providing an in-depth analysis for the use of color and FIR. Their conclusion is that on the tested images, visible images provided better results than the infrared ones.

Olmeda et al. [102] propose a pedestrian detection system based on discrete features in thermal infrared images, these descriptors are matched with defined regions of the body of a pedestrian. In case of a match it creates a regions of interest which is then classified using an SVM. Olmeda et al. [103] present a study on pedestrian classification and detection in FIR images using a descriptor named Histograms of Oriented Phase Energy combined with a latent variable SVM approach.

With the exception of the dataset used by Olmeda et al. [103], from our knowledge, the other articles do not make public the acquired images. As a consequence, it is quite difficult to compare the proposed approaches.

2.2 Datasets

Although there exists a reasonable number of benchmark datasets for the pedestrian detection in the Visible domain[1], in case of FIR images most of the datasets are not publicly available.

Datasets like that proposed by Simon Lynen [113], Davis and Keck [32], Davis and Sharma [33] focus mostly on surveillance application, therefore they use a fixed-camera setup.

Recently Olmeda et al. (2013) [103] proposed a dataset[2] acquired with an Indigo Omega, having and image resolution of 164×129. The dataset is divided in two parts: one that tacks the problem of pedestrian classification (OlmedaFIR-Classification), and the other one that is constructed for the problem of pedestrian detection (OlmedaFIR-Detection). In figure 2.1 are presented examples of images from the OlmedaFIR-Detection dataset. Unfortunately, it does not contain also information from the Visible spectrum, therefore making difficult a complete assessment of the FIR performance.

An interesting dataset that contains both FIR and Visible images is proposed by Bertozzi et al. [12]. Unfortunately, the dataset had just a small number of annotations (around 1000 BB), therefore it might not provide statistically relevant results. Moreover, this dataset is not publicly available[3].

---

[1]The Visible domain dataset will be treated in chapter 5
[2]We will further refer to this dataset as **OlmedaFIR**
[3]This dataset is maintained by Vislab. Terms and conditions for usage may apply. `http://vislab.it/`

a)   b)

Figure 2.1: Images examples from Oldemera dataset a),b)

In order to respond to the deficiencies of the datasets proposed by Olmeda et al. [103] and Bertozzi et al. [12], on one hand, we propose a new benchmark for pedestrian detection and classification in FIR images, which consists of sequences acquired in an urban environment with two cameras (FIR and color) mounted on the exterior of a vehicle. We will further refer to the proposed dataset as *RIFIR*[4]. On the other hand, we have extended the annotations on the dataset proposed by Bertozzi et al. [12]. We will further refer to the extended dataset as *ParmaTetravision.*

In table 2.1 we present an overview of existing pedestrian datasets. In what follows we will present dataset statistics for the both *ParmaTetravision* and *RIFIR.*

2.2.1   Dataset ParmaTetravision

Dataset ParmaTetravision contains information taken from two visible and two infrared cameras and was provided to us by VisLAB laboratory in Parma Italy [12]. In a previous work [16], there were annotated around 1000 pedestrians BB (table 2.2), but we felt that this will not provide a large enough dataset in order to compare the performance of different features. Thus, we have extended the annotation to include a much larger number of images and manually annotated BB for both training and testing[5].

	Pedestrian	Non-Pedestrian	Overall
Number of BB (IR)	1089	1003	2092

Table 2.2: ParmaTetravision[Old] Dataset statistics

---

[4]The dataset is publicly available at the web address: `www.vision.roboslang.org`
[5]For training we have use sequences 1 and 5 from the dataset; while for testing sequences 2 and 6.

Dataset	Properties										Training		Testing	
	Acquisition setup	Environment	Infrared	Visible	Occlusion Label	Stereo	Resolution	No. Img.	No. Unique Ped	No. BB	No. Img.	No. Ped.BB	No. Img.	No. Ped.BB
ETHZ Thermal Infrared Dataset[113]	Surveillance	Road Scene	FIR	NO	NO	No	324×256	4318	22	6500	-	-	-	-
OSU Thermal Pedestrian Database[32]	Surveillance	Road Scene	FIR	NO	NO	No	360×240	284	-	984	-	-	-	-
OSU Color-Thermal Database[33]	Surveillance	Road Scene	FIR	YES	NO	No	320×240	17089	48	-	-	-	-	-
RGB-NIR Scene Dataset[24]	Surveillance	Outdoor	NIR	YES	-	No	1024×768	477	-	-	-	-	-	42
OlmedaFIR-Classification[103]	Mobile	Road Scene	FIR	NO	NO	NO	164×129	81529	-	~16000	~10000	~10000	~6000	~6000
OlmedaFIR-Detection[103]	Mobile	Road Scene	FIR	NO	NO	NO	164×129	15224	-	8400	~6000	~4300	~5000	~4100
Parma-Tetravision[a][12]	Mobile	Road Scene	FIR	YES	YES[b]	YES	320×240	18578	280	~18000	~10000	~9000	~8000	~8800
RIFIR (Proposed Dataset)	Mobile	Road Scene	FIR	YES	YES[b]	NO	650×480	~24000	171	~20000	~15000	~14000	~9300	~6200

Table 2.1: Datasets comparison for pedestrian classification and detection in FIR images

[a]Dataset statistics based on our annotations

[b]Only two-class occlusion labels available: occluded or not occluded

As presented in table 2.3, the final dataset contains 10240 images for **training** having annotated 11554 pedestrian BB in visible spectrum and 9386 BB in IR spectrum; and 8338 images for **testing** with 9386 annotated pedestrian BB in visible and 8801 in IR. The disagreement in the number of pedestrian from visible and IR is due to differences in camera optics and positioning. For the final dataset used for the problem of pedestrian classification, we have retained only those BB that have a height above $32px$, are visible in both cameras and don't present major occlusions. Therefore in the end we have **6264** pedestrian BB for **training** and **5743** pedestrian BB for **testing**. Furthermore, for the problem of pedestrian classification we have extracted 26316 negative BB for training and 14823 for testing.

	Sequence Train	Sequence Test	Overall
Number of frames	10240	8338	18578
Number of unique **pedestrians**	120	160	280
Number of annotated **pedestrian BB** (Visible)	11554	11451	23005
Number of annotated **pedestrian BB** (IR)	9386	8801	18187
Number of **pedestrian BB** visible in both cameras with height > 32 px, and not presented major occlusions	6264	5743	12007
Number of **negative BB** annotated	26316	14823	41139

Table 2.3: ParmaTetravision Dataset statistics

In figure 2.3 is presented the height histogram for the annotated pedestrians for both Training and Testing. Most of the pedestrians have a height inferior to 150 pixels. Due to a small difference in optics, the pedestrians in FIR images will appear slightly larger than those in Visible images.

In the dataset, annotated pedestrians tend to be concentrated into the same regions. In figure 2.2 is presented a normalized heat map obtained by plotting the annotated pedestrian BBs. The heat map is presented as in indicator that even if pedestrian tend to concentrate in the same region, different optics and environment will produce various heat maps. In figure 2.4 is presented an example of image from the ParmaTetravision dataset.

(a)   **(b)**
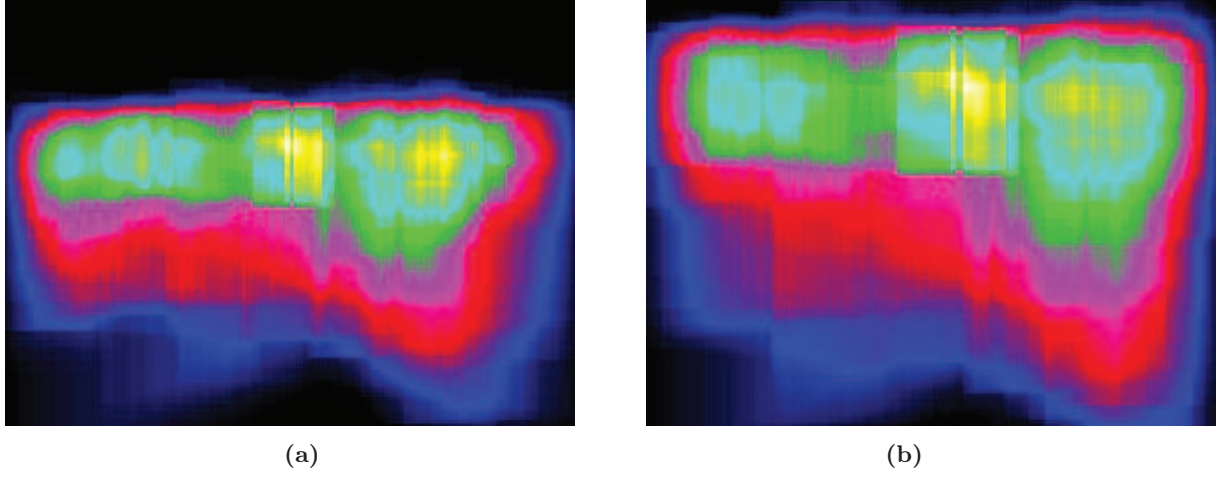
Figure 2.2: Heat map of training for ParmaTetravision Dataset: a) Visible b) FIR

(a)   **(b)**
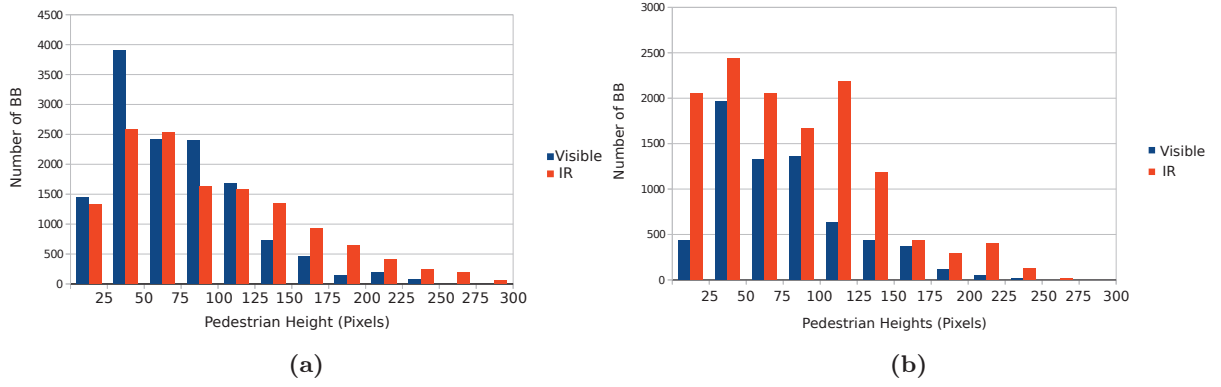
Figure 2.3: Pedestrian height distribution of training (a) and testing (b) sets for ParmaTetravision

a)   **b)**

Figure 2.4: Images examples from ParmaTetravision dataset a) Visible spectrum b) Far-infrared spectrum

44

2.2.2 Dataset RIFIR

For the acquired dataset, we have used two cameras: one Visible domain camera (colour) with a resolution of 720×480 and a FIR camera with a resolution of 640×480. In table 2.4 are presented some information regarding the employed FIR camera[6].

Characteristic	Value
Pixel Resolution	640×480
Focal length	24.5 mm
Spectral range	$7.5\mu m$ to $13\mu m$
Object temperature range	-20 to $+150°C$
Accuracy	$\pm 2\%$ of reading
Image frequency	50Hz
Control	GigE Vision and GenICam compatible
Power system	12/24 VDC, 24 W absolute max
Operating Environment	*Operation Temperature:* $-15°C$ to $+50°C$; *Humidity:* $0-95\%$

Table 2.4: Infrared Camera specification

Due to difference in camera optics and position, we had to annotate the pedestrian independently in the Visible and FIR images. As presented in table 2.5 the final dataset contains 15023 images in **training** with 19190 annotated pedestrian BBs in Visible spectrum and 14356 in FIR spectrum; and 9373 images for **testing** with 7133 annotated pedestrian BBs in Visible and 6268 in the FIR domain.

Following the same methodology as in the case of ParmaTetravision dataset, for the final constructed classification dataset we have only considered those pedestrians with a height above *32 pixels*, that are visible in both cameras, and do not present occlusions. In consequence, there are 9202 pedestrian BB for training and 2034 for testing. In what concerns the negative BBs, we have considered 25608 in training set and 24444 in testing.

---

[6]The camera was provided by Laboratoire d'Electronique, d'Informatique et de l'Image (Le2i) `http://le2i.cnrs.fr/`

In figure 2.5 is presented the height histogram for the annotated pedestrian in both Training and Testing. While in the ParmaTetravision dataset most of the pedestrians had a height below 150 pixels, in the case of RIFIR dataset, most of the pedestrians have a height below *100 pixels*, thus making the dataset more challenging. In figure 2.6 is presented the heat map, for both Visible and FIR, obtained by superimposing the annotated pedestrians. Small differences are due to camera optics and positioning. In figure 2.7 is presented an extract from the RIFIR dataset.

	Sequence Train	Sequence Test	Overall
Number of frames	15023	9373	24396
Number of unique **pedestrians**	138	33	171
Number of annotated **pedestrian BB** (Visible)	19190	7133	26323
Number of annotated **pedestrian BB** (IR)	14356	6268	20624
Number of **pedestrian BB** visible in both cameras with height > 32 px	9202	2034	11236
Number of **negative BB** annotated	25608	24444	50052

Table 2.5: RIFIR Dataset statistics

(a)   (b)
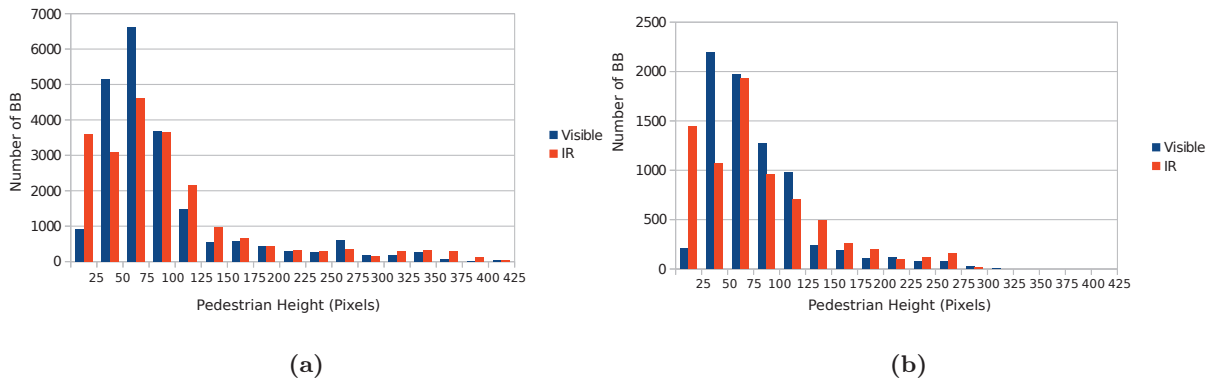
Figure 2.5: Pedestrian height distribution of training (a) and testing sets (b) for RIFIR

(a)   (b)
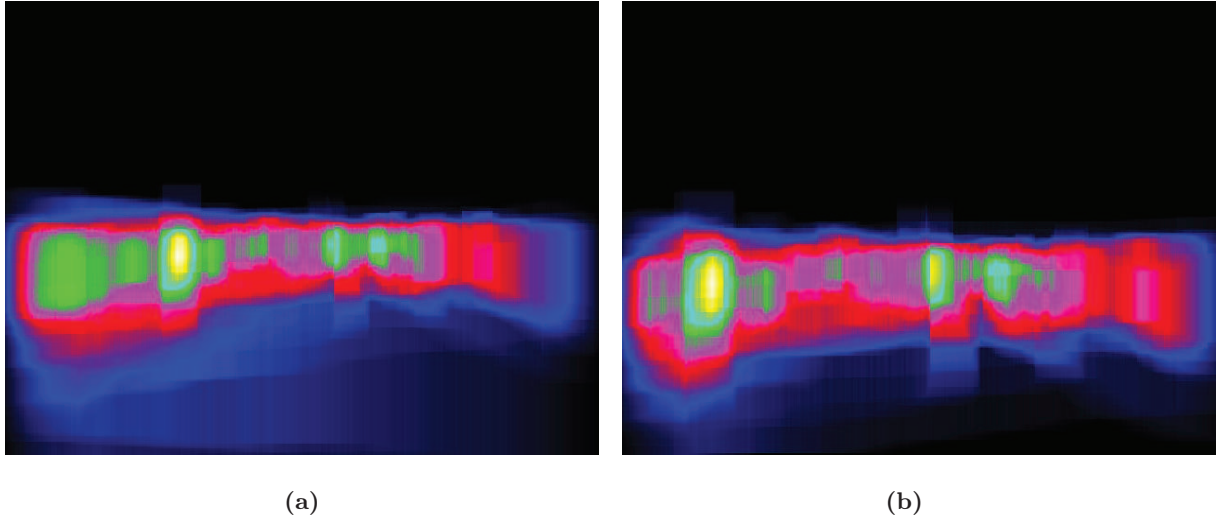
Figure 2.6: Heat map of training for RIFIR Dataset: a) Visible, b) FIR

a)   b)

Figure 2.7: Images examples from RIFIR dataset a) Visible spectrum b) Far-infrared spectrum

2.3 A new feature for pedestrian classification in infrared images: Intensity Self Similarity

Motivation In [15], detection of pedestrians ROIs based on an algorithm of head detection was combined with a classifier based on local and global SURF-based features. The local features describe the appearance of an obstacle and are extracted from a codebook of scale and rotation-invariant SURF descriptors. Whereas, global features, extracted from a set of interest points, provide complementary information by characterizing the shape and the texture. The disadvantage of SURF points used in the phase of ROI classification is that detected key points repeat more often on background and less on the people even when looking at two consecutive frames of a video [84]. Therefore, another type of descriptor is needed that will be more robust to consecutive frames, like HOG or CSS.

47

Feature description   Inspired by CSS, we propose an original feature representation, called Intensity Self Similarity, adapted for FIR images. In contrast with images acquired with cameras in visible spectrum, that can provide color information, those taken using FIR sensor, provide only information about the pixel intensities, making CSS representation not suitable. After a careful analysis of road scenes in FIR spectrum, we believe that FIR images emphasise several intensity structures, since pixels within a pedestrian head region have approximately the same intensity values, the arms intensity values seem to be similar and this also could be applied to the leg areas. According to this, we propose a self similarity feature based on intensities values of thermal images, rather than on color information.
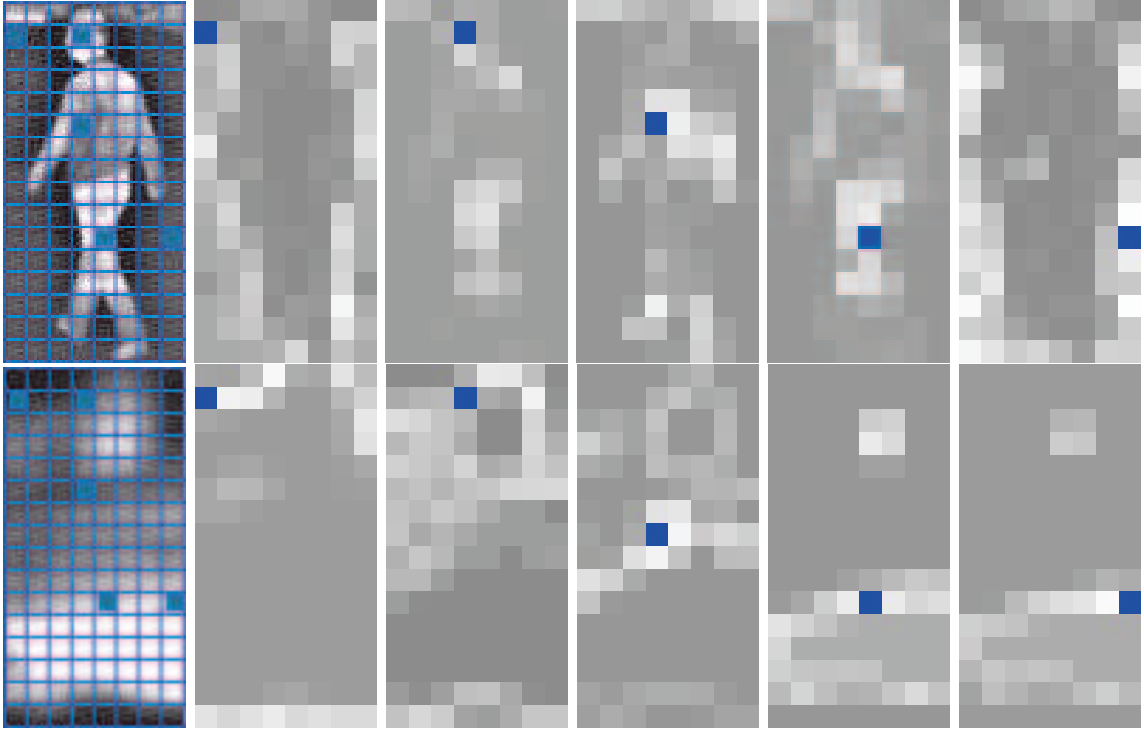
Figure 2.8: Visualisation of Intensity Self Similarity using histogram difference computed at positions marked with blue in the IR images. A brighter cell shows a higher degree of similarity.

We divide each pedestrian full-body BB into n blocks of 8×8 pixels (see figure 2.8). After computing a histogram for each block, we construct a similarity vector of $n * (n - 1)/2$ elements, by comparing the histogram of each block with the histograms of all the other blocks within a given BB.

For the comparison of two histograms H_1 and H_2, we have tested different techniques like:

- *Histogram Intersection:*$\sum_{i=\overline{1,histSize}} min(H_1[i], H_2[i])$

- *Histogram Difference:*$\sum_{i=\overline{1,histSize}} |H_1[i] - H_2[i]|$

- *Chi Square Distance:* $\sum_{i=\overline{1,histSize}}(H_1[i] - H_2[i])^2/H_2[i]$
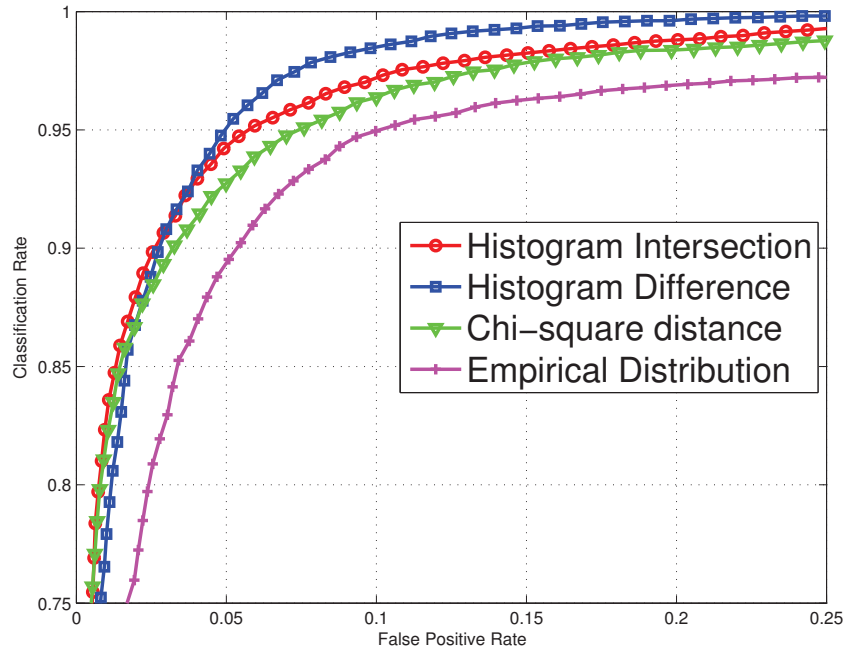
Figure 2.9: Performance of ISS feature on the dataset ParmaTetravision[Old] using different histogram comparison strategies

- *Empirical Distribution:* $\sum_{i=\overline{1,histSize}} 1_{H_1[i] \leq H_2[i]}$

Feature parameters optimisation This feature is used to feed up a fast, but efficient linear-kernel SVM classifier. In order to validate the proposed feature we have used the dataset ParmaTetravision[Old] that contains 1089 pedestrians. The pedestrian detection performances are estimated by the precision rate, the recall rate and the F-measure, using a 10-fold Cross Validation (CV) technique.

In figure 2.9 is plotted the ROC[7] curve for each tested technique of histogram comparison. Subsequently, we have chosen to use histogram difference rather than histogram intersection, like [127], because it provided lower false positive rate for a high recall.

For the choice of block and histogram size, we have tested blocks of 8×8 and 16×16 pixels, and six different histograms sizes. The results in terms of F-measure are presented in figure 2.10. As it can be observed, the histogram size does not have a significant impact for the performance, results varying just between $\pm 0.5\%$. On the contrary, the block size, has a greater influence over the results.

For the final configuration of ISS feature, we have chosen to use block size of 8×8 pixels, histogram of 16 bins and histogram difference for comparison algorithm.

---

[7]Receiver operating characteristic
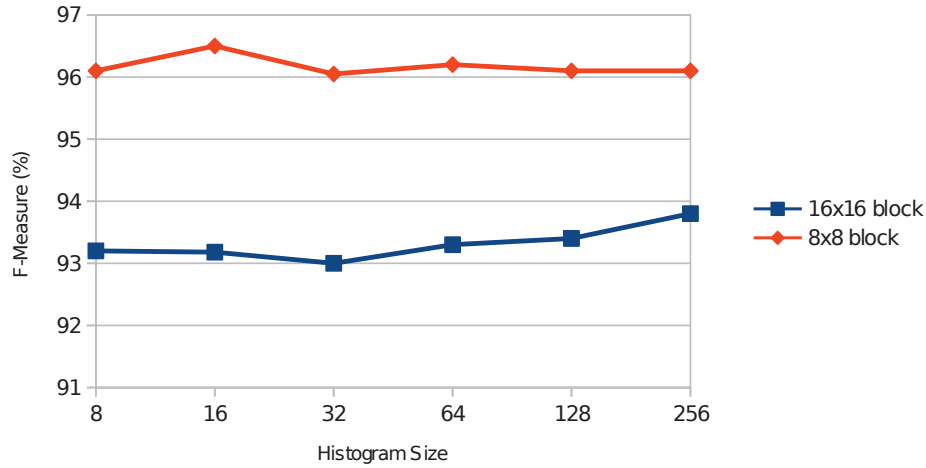
Figure 2.10: Comparison of performance in terms of F-measure for different combination of Histogram Size and Blocks Size

In table 2.6 are presented the classification performances obtained with ISS and HOG features with an SVM classifier trained with a Linear kernel and a penalty parameter one, to allow fast classification and fair feature representations comparison. As it can be observed, on the tested dataset, ISS, with an F-measure of 96.5%, has provided better results than HOG feature, with an F-measure of 92.3%.

We emphasis the fact that there is a complementarity between ISS and HOG representations, since ISS features provide information about the similarities between different regions within a BB, while HOG features provide information concerning the shape of objects within a BB. We decided to exploit this complementarity with an early fusion at the feature level. The results presented in table 2.6 show that the fusion of these two descriptors provides a statistically significant improvement of the F-measure up to 97.7% on ParmaTetravision[Old].

Features	ISS	HOG	ISS+HOG
F-Measure(%)	96.5	92.3	**97.7**
Precision(%)	96	91.5	**97.8**
Recall(%)	97	93.1	**97.7**

Table 2.6: Classification results with early fusion of ISS and HOG features FIR images on ParmaTetravision[Old]

2.4 A study on Visible and FIR

The initial experiments presented in section 2.3 showed ISS to be a promising feature given good results on its own. We also showed that ISS is complementary with HOG features increasing

the F-Measure. Nevertheless, the testing dataset was fairly small. Consequently, we decided to extend the experiments to include more features and several datasets.

In this section we are going to compare the performance of different features like HOG, LGP, LBP and the proposed ISS on the Far Infrared domain, using three datasets: ParmaTetravision, OlmedaFIR-Classification and the proposed RIFIR. Moreover, a comparison between the FIR and Visible Domain is conducted using the datasets ParmaTetravision and RIFIR.

2.4.1 Preliminaries

For all three databases, in order to be consistent in the classification process, we have resized the annotated BBs to a size of 48 pixels in width and 96 in height.

HOG features are computed on cells of 8×8 pixels, accumulated on overlapping 16× 16 pixel blocks, with a spatial shift of 8 pixels. This results in a number of 1980 features.

LBPs and LGPs features are computed using cells 8×8 pixels, and a maximum number of $0 - 1$ transitions of 2. This results in a number of 4248 features.

ISS is computed on cells of 8×8 pixels, histogram size of 16 pixels and histogram difference. This results in a number of 5944 features.

These features are fed to a linear SVM classifier. For this, we have used the library LIBLINEAR [44].

All the results in this section are reported in term of ROC curve (false positive rate vs classification rate), considering as reference point the false positive rate obtained for a classification rate of *90%*.

2.4.2 Feature performance comparison on FIR images

First of all, we decided to evaluate the performance of the considered features (HOG, LBP, LGP, ISS) in the FIR domain. In figure 2.11 is presented the performance of using each individual feature independently on dataset RIFIR (figure 2.11.a), ParmaTetravision (figure 2.11.b) and Oldemera-Classification(figure 2.11.c).

On datasets RIFIR and Oldemera-Classification the best performing feature is LBP, followed closely by LGP. On ParmaTetravision dataset, the best performing feature is LGP followed closely by LBP. On datasets ParmaTetravision and Oldemera-Classification HOG features performs better than ISS, while on RIFIR the situation is reversed.

In our opinion, the difference in performance between features comes from the fact that even if all three datasets were obtain using FIR cameras, there is a difference in sensors, road scenes and environmental conditions. It seems that as single feature, the Local Binary/Gradient Patterns
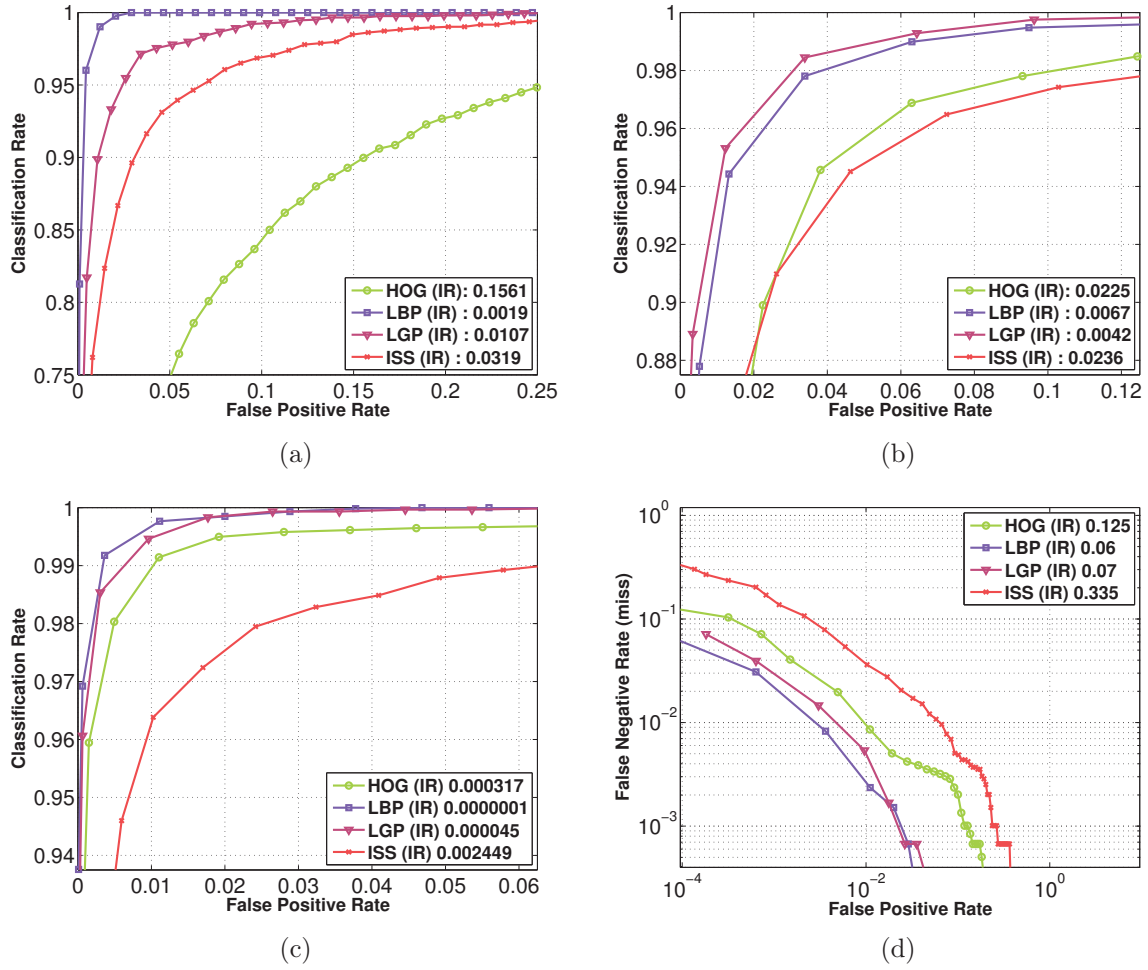
Figure 2.11: Performance comparison for features HOG, LBP, LGP and ISS in the FIR spectrum on datasets a) RIFIR b) ParmaTetravision c) Oldemera-classification. The reference point is considered the obtained false positive rate for a classification rate of 90%. In figure d) are also shown the results for Oldemera-classification but this time as miss-rate vs false positive rate. In this case the reference point is the miss rate obtained for a false positive rate of 10^{-4}

are more adapted for the task of pedestrian classification in FIR images. Nevertheless, because the features are complementary, we will test a fusion of features in section 2.4.5.

In figure 2.11.d) is presented a comparison between the considered features on the Oldemera-classification, in terms of False Positive Rate vs False Negative Rate (miss rate), on a log-log scale. We chose to present the results in this manner because this is the preferred approach of Olmeda et al. [103]. The reference point is considered the false negative rate obtained for a false positive rate of 10^{-4}. We report slightly different results than that of Olmeda et al. [103] for HOG and LBP features. Thus, for HOG we obtain a miss rate of 0.125 (in comparison with the reported 0.21 [103], and for LBP we obtain a miss rate of 0.06 (in comparison with the reported 0.41 [103]). The difference in results may come from slightly different implementation for the features and from the use of different libraries for SVM classifier.
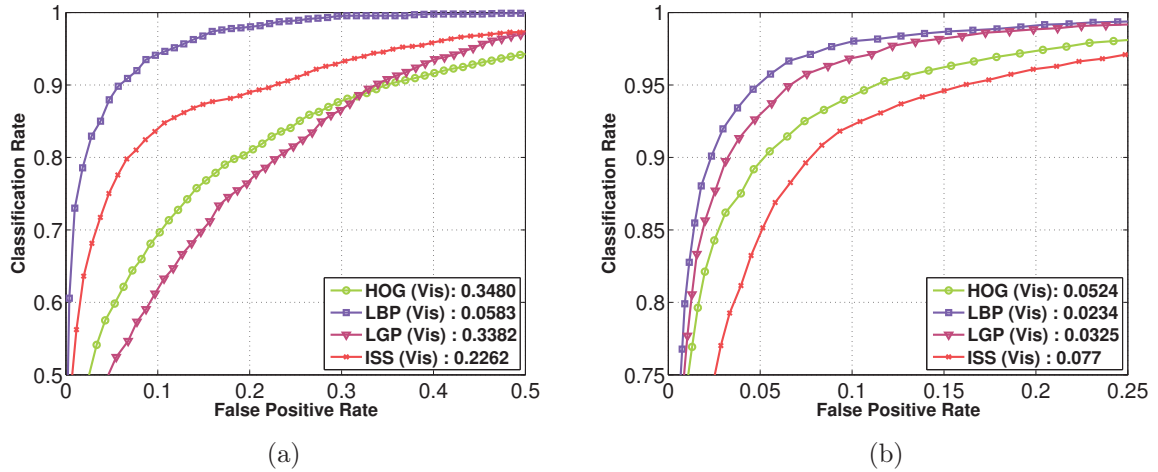
Figure 2.12: Peformance comparison for the features HOG, LBP, LGP and ISS in the Visible domain on datasets a) RIFIR, b) ParmaTetravision

2.4.3 Feature performance comparison on Visible images

For the second scenario, we decided to evaluate the features (HOG, LBP, LGP and ISS) in the Visible domain on the datasets RIFIR and ParmaTetravision. The results are reported in figure 2.12. LBP continues to be one of the most robust features obtaining a false positive rate of 0.05 on RIFIR dataset and 0.02 on ParmaTetravision. For the other considered features the results are quite different.

As it can be observed from the example images from both datasets, RIFIR color images have more noise than the grayscale images from ParmaTetravision. This has a direct impact over the performance of features based on gradient: HOG and LGP. Thus, while ISS features manage to be more robust in the context of noise (RIFIR), HOG and LGP perform better on higher quality images (ParmaTetravision).

2.4.4 Visible vs FIR

Having the performance of different features on both Visible and FIR domains, we can now compare the two spectrums. In figure 2.13 is presented a comparison between the same feature computed on Visible and FIR for the two databases: RIFIR and ParmaTetravision. On both datasets, the features computed on the FIR images have a better performance than those computed on Visible. We withhold from drawing a definite conclusion that FIR cameras will always perform better than Visible ones because it depends on the quality of cameras used and also optics. What we can definitely say is that on the tested dataset the FIR spectrum gives better results.

The performance difference on the RIFIR dataset between Visible and FIR is quite large for LGP and LBP with a factor of approximatively *30*. HOG and ISS features computed on FIR

result in a smaller number of false positives than the equivalent on Visible, with a factor of *two*, on both datasets.

2.4.5 Visible & FIR Fusion

In section 2.4.4 we have showed that on the two considered datasets, for the task of pedestrian classification, features computed on FIR images performed better than the counterpart computed on Visible.

By fusing both spectrums, as seen in figure 2.14.a) for RIFIR and 2.14.b) for ParmaTetravision, the false positive rate for a classification rate of 90%, is further reduced.

HOG features computed on Visible and FIR improve by a factor of *two* the results, in comparison with just computing on FIR domain, for RIFIR dataset, and by a factor of five for ParmaTetravision. For RIFIR dataset, the same factor of approximately *two* is obtained for LBP, LGP, and ISS features, while on the ParmaTetravision the factor will be usually equal of larger than *five*.

Features computed from FIR and Visible are highly complementary, and the use of the two spectrums will always lower the error rate. Unfortunately, the information fusion is not straightforward because two different cameras are used, one for FIR and one for Visible domain, therefore there will always be difference in point of views. A correlation method between the two domains is necessary. A possible hardware solution is to construct a camera capable of capturing information from both light spectrums.

2.5 Conclusions

In this chapter we have described a new feature, ISS, that we adapted for the thermal images and performed extensive tests on different datasets. Moreover, we have proposed a new dataset, RIFIR, publicly available, in order to benchmark different algorithms of pedestrian detection and classification. This dataset contains both Visible and FIR images, along with correlated pedestrian and non-pedestrian bounding boxes in the two spectrums.

Moreover, a comparison between features computed on Visible and FIR spectrum is performed. On the two tested datasets, Far-Infrared domain provided more discriminative features. Also, the fusion of the two domains will further decrease the false positive error rate.

As shown in the related work section of this chapter, FIR spectrum was already studied in different aspects for the task of pedestrian classification and detection. In comparison, in the next chapter we present an analysis performed on another infrared spectrum, less popular: the Short Wave Infrared.
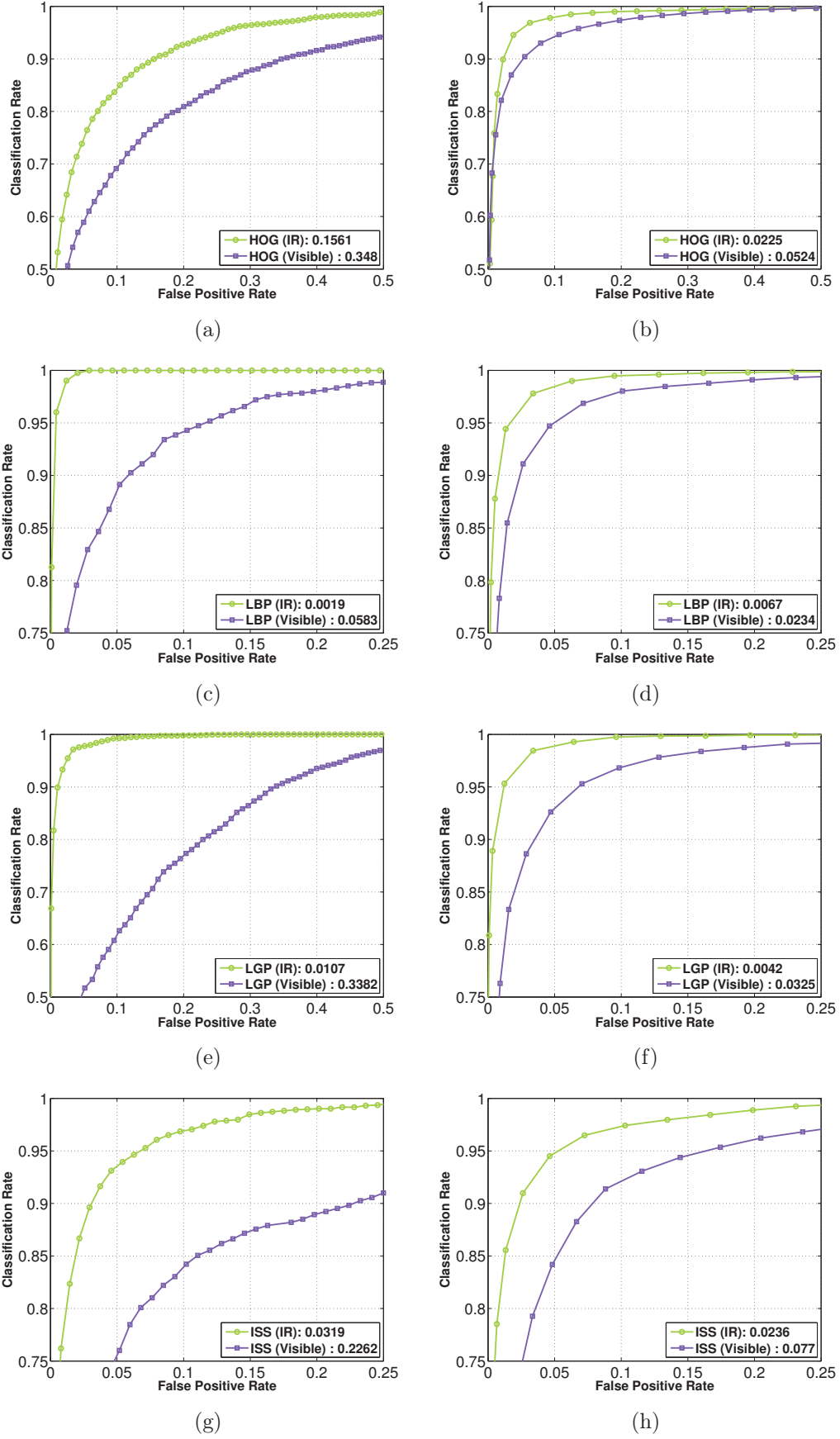
Figure 2.13: Performance comparison of features between Visible and FIR domains on: a), c), e), g) RIFIR dataset; b), d), f), h) ParmaTetravision dataset
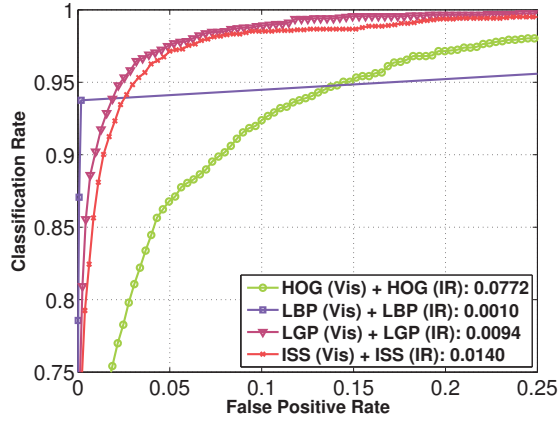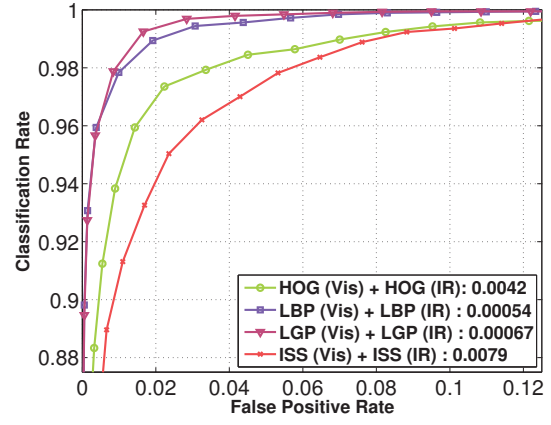
Figure 2.14: Individual feature fusion between Visible and FIR domain on a) RIFIR dataset b) ParmaTetravison dataset

3

Pedestrian Detection and Classification in SWIR

Contents

The purpose of this chapter is to investigate the suitability of the SWIR spectrum for the problem of pedestrian detection and classification. In what follows we present related work along with a short analysis of imagining in SWIR spectrum. Afterwards, in order to study the performance of pedestrian detection and classification using SWIR cameras we have performed two different experiments.

For the first one we have used a dataset provided by Vislab[1] acquired with a low cost SWIR camera. After having annotated three different sequences of images, we then evaluated if features learned on visible images are suitable to be used on SWIR images. Other tests performed include an SVM classifier based on deformable part models ([47], [48]), on grammar models [59] and a HAAR based classifier [87].

---

[1]Artificial Vision and Intelligent Systems Laboratory (VisLab) of Parma University (Italy) - `www.vislab.it`

Due to the limitations of the first dataset, for the second experiment we have acquired and annotated a new set of images using two cameras, a SWIR and a Visible one. Thus, we are able to compare pedestrian classification performances in the two wavelengths on a fairly large dataset. For this, we compare several spatial features like HOG, LBP and LGP. Moreover, we propose to enrich the intensity-based features from visible domain with features extracted from SWIR.

3.1 Related work

SWIR imaging began to be taken into consideration for computer vision applications because it could bring useful contrast or complementary information to situations and applications where visible or thermal imaging cameras are ineffective. This makes SWIR frequently used for diverse applications such as aligning telecommunications fibers and sources, engineering optical wave-guides, inspecting pharmaceutical quality, sorting recycled plastics, monitoring incoming sources of raw agricultural products to groom out contamination by dirt, stones or packaging debris, as well as grade sorting by moisture level or fat content, remote sensing of arid and semiarid ecosystems[4], vegetation mapping in semiarid aread [37], ocean data color processing [130]. Applications that mainly benefit from reduced scattering effects of longer wavelengths, illumination from invisible sources (for example infrared active illumination or simply the night glow from the upper atmosphere) or thermal emitting objects with temperatures above 150 $C°$ are candidates for SWIR cameras [63].

Unlike Mid Wave IR (MWIR) and Long Wave IR (LWIR), SWIR cameras can image through the windshield and thus be mounted in the vehicle's cabin for a "driver's eye" view of the way ahead. Moreover, SWIR imagers have the ability to see clearer at long distance through the atmosphere, making SWIR suitable for investigations in the field of automotive applications [122]. The main issues concerning it have been to achieve low cost SWIR sensors, operating at close to room temperature and CMOS compatible.

The problem of pedestrian detection and classification has been approached from both a hardware and software perspective, using different sensors and developing many different detection techniques. A variety that however doesn't include Short Wave InfraRed (SWIR) sensors, able to provide images with a noticeably different information content from visible ones (see figure 3.1).

3.2 SWIR Image Analysis

From an empirical perspective, visible and SWIR images acquired indoor highlight some very different characteristics (e.g. figure 3.1), but as soon as acquisitions are moved outdoor (in clear

visibility conditions), those differences span reduce. (fig. 3.2).

(a)   (b)

(c)   (d)
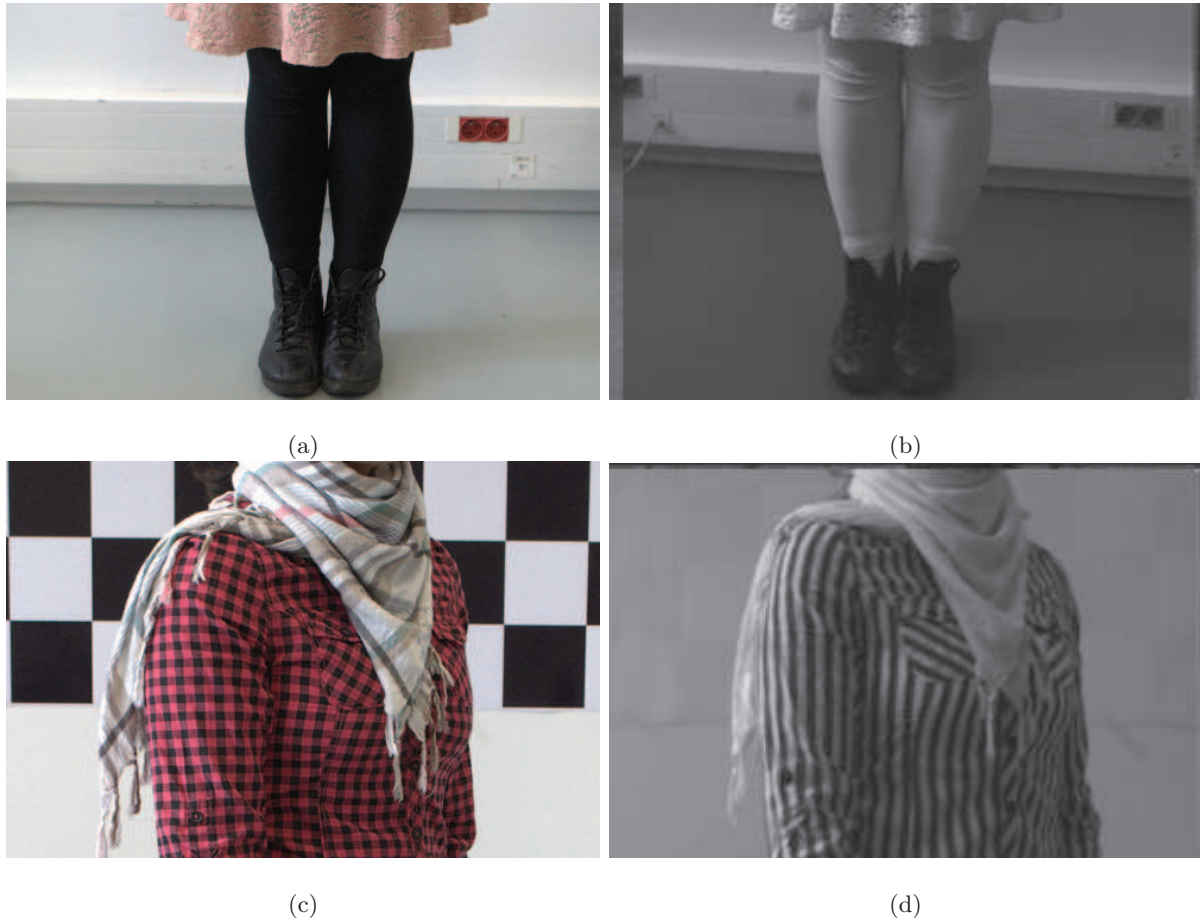
Figure 3.1: Indoor image examples of how clothing appears differently between visible [a, c] and SWIR spectra [b, d]. Appearance in the SWIR is influenced by the materials composition and dyeing process.

swir   *visible*

Figure 3.2: Images acquired outdoor: SWIR and visible bandwidths highlight similar features both for pedestrian and background.

The difference comes from the fact that visible spectrum covers the wavelength between 380 nm and 700 nm, therefore light in SWIR band (wavelengths from $900nm$ to $1700nm$) is not visible for the human eye. Despite of this, the light in the short wave infrared region interacts with objects in a similar way as the visible wavelengths. This is because light in the SWIR bandwidth is a reflective light (bouncing off objects in a similar way as the visible light).

Most of the existing SWIR cameras are based on InGaAs[2], HgCdTe [3] or InSb[4] sensors. Sensors based on HgCdTe or InSb are not very practical for an ADAS application due to the fact that they have to be cooled at very low temperatures [71], therefore throughout this chapter we have worked only with SWIR cameras based on InGaAs sensor. If efficient sensors are build, they can be very sensitive to light, thus permitting for SWIR cameras to work in dark conditions.

Another advantage of the SWIR cameras in comparison with other types of infrared cameras is the ability to capture images through glass, thus it can be mounted inside a vehicle.

3.3 Preliminary SWIR images evaluation for pedestrian detection

3.3.1 Hardware equipment

The device employed to acquire the visible and SWIR images shown in this section was developed within the European funded 2WIDE_SENSE collaborative project[5]. The camera has the possibility to acquire in the full Visible to SWIR bandwidth (see figure 3.3). In addition, the camera features a Bayer-like four filter pattern on its Focal Plane Array (FPA)[6] to enable the simultaneous and independent acquisition of four images, each one in a different spectral bandwidth (see figure 3.4a and 3.4b).

The filters Clear (C) *(400-1700 nm)*(acquires the full spectrum images), F1 (*1300-1400nm*), F2 (*1000-1700nm*), F4 (*540-1700nm*) were chosen to suit ADAS applications. Filter F4 is not used in the current work because it isolates the red bandwidths. While this might be useful for applications like traffic sign recognition or vehicle back lights, it might not be particularly interesting for the application of pedestrian detection.

---

[2]Indium Gallium Arsenide
[3]Mercury Cadmium Telluride
[4]Indium antimonide
[5]http://www.2wide-sense.eu.
[6]A **focal plane** is a sensing device used in imaging consisting of an array of pixels that are light-sensing at the focal plane of a lens.

Characteristic	Value
Spectral Range	VIS/NIR/SWIR
Filter Pattern	**C**(400÷1700)nm
	F1(1300÷1700)nm
	F2(1000÷1700)nm
	F4(540÷1700)nm
Dynamic Range	120dB
Angular Resolution	min 11px/∘
Field of View	HFOV30
	VFOV22
Imager Resolution	640×512px
Pixel Pitch	15 μ
Focal Length	18mm
Frame Rate	$> 24 fps$
Camera Size	(130×40×40)mm
Camera weight	$500gr$
Temperature Range	(-40 ÷ 80)
Supply Voltage	(6 ÷ 16) V
Power Consumption	< 1V

Table 3.1: Camera specifications
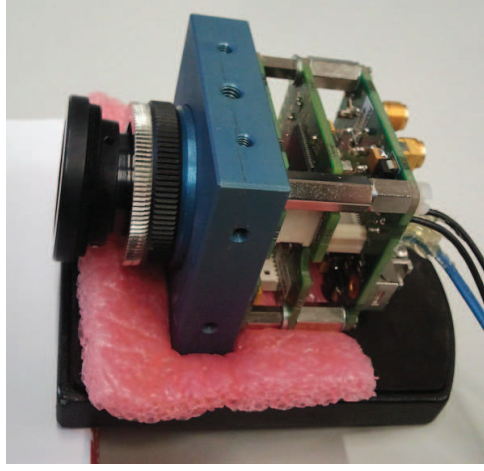
Figure 3.3: SWIR 2WIDE_SENSE camera

(a)

(b)
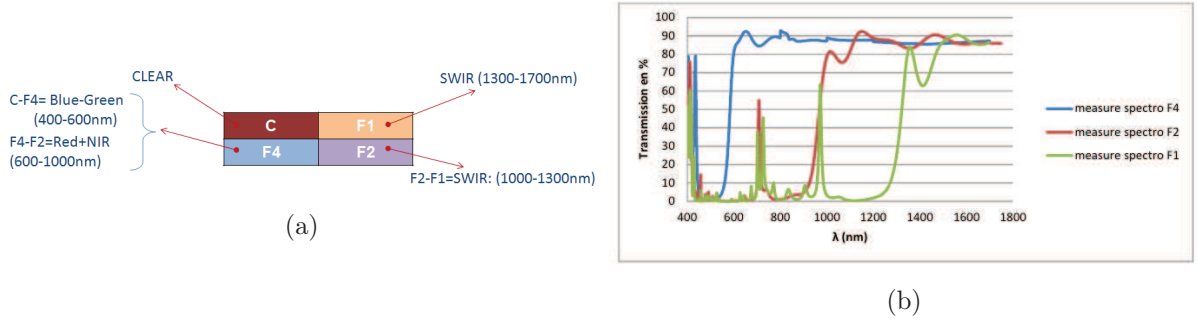
Figure 3.4: a) The 4×4 filter mask applied on the FPA. b) Filters F1, F2 and F4 transmission bands.

The camera has an uncooled InGaAs sensor, having a resolution of 640×512 px. Table 3.1 presents an overview of the characteristics of the camera module. The main feature of the camera is its large spectrum sensitivity (400-1700nm).

3.3.2 Dataset overview

Corresponding to filters C, F1 and F2 we have acquired three image sequences choosing a fixed setup for the camera in order to be able to compare the results obtained using different bandwidth filters for similar scenes. The filters had to be manually changed for each acquisition therefore some differences in the scene can be expected. The number of full-frame images tested for each bandwidth are presented in table 3.2.

After the acquisition of the three sequences, we have manually annotated a total of 4348 Bounding Boxes (BB) surrounding pedestrians, from which only 4.57% are occluded. This corresponds to 1998 BB annotated in filter C bandwidth, 1200 for filter F2, 1150 for filter F1.

In figure 3.5 the height distribution of the annotated pedestrians in each sequence is presented. We can observe that most of the BB are in medium range [50-100) with 41% of the total number

or near range [100-200] with 48% of the total number of BB. The closest pedestrian (with an average height of $200\,px$) are at a distance of about $4\,m$ while the farthest (with a height around $50\,px$) are at a distance of $30\,m$.
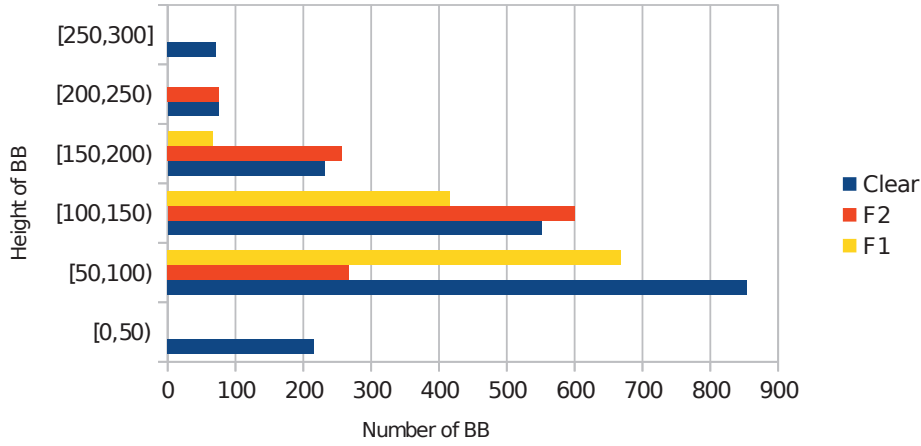
Figure 3.5: Height distribution over the annotated pedestrians.

Bandwidth	**Clear**	**F2**	**F1**
Full-frame Images	1704	1374	1421

Table 3.2: Number of full-frame images on each tested bandwidth

3.3.3   Experiments

3.3.3.1   Features from Visible to SWIR

There may be some differences in the way that clothes and the human skin are represented, but people have a similar appearance from their edges gradients point of view. In fig. 3.6 a visualisation of Haar wavelength computed on diagonal, horizontal and vertical, along with Sobel filter (which is the basis for our gradient computation of HOG features) for the same scene under the three different filters C, F1 and F2 is shown. As it can be seen from the images, the features are quite similar in the different bandwidths. Small differences can be observed in the hair, clothes and background, but the main contours of the objects are quite similar for both Haar transformations and Sobel transformation in the different tested bandwidths.

Most of the top algorithms developed for images acquired in the Visible bandwidth employ Histogram of Oriented Gradients (HOG) features [30], usually by combining them with others as HAAR-like features [35], color self-similarity [127] etc.

| (a1) | (b1) | (c1) | (d1) | (e1) |

| (a2) | (b2) | (c2) | (d2) | (e2) |

| (a3) | (b3) | (c3) | (d3) | (e3) |
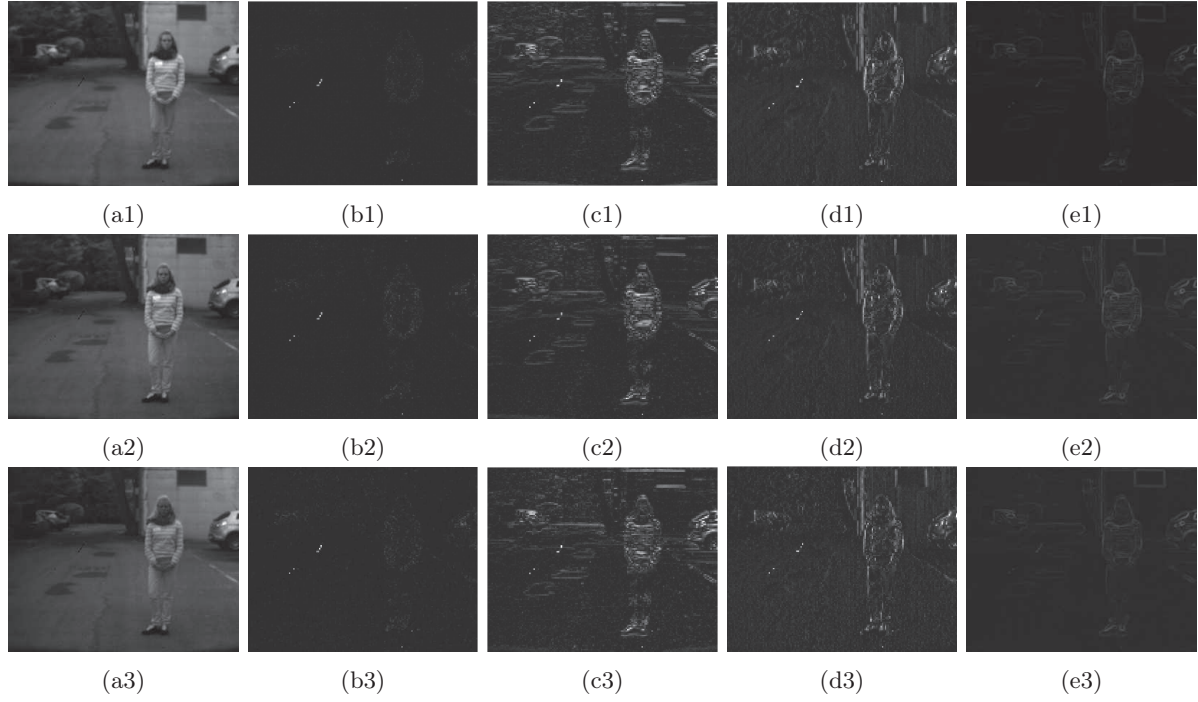
Figure 3.6: Image comparison between Visible range (a1), F2 filter range (a2) and F1 filter range (a3) with the corresponding on-column visualization of HAAR wavelets: diagonal (b1, b2, b3), horizontal (c1), (c2), (c3), vertical (d1), (d2), (d3) and Sobel filter (e1), (e2), (e3). Due to negligible values of the HAAR wavelet features along the diagonal direction, the corresponding images [b1, b2, b3] appear very dark.

In order to test if features trained on visible images are suitable to use for the SWIR images, we have trained an SVM classifier based on HOG features, since it is one of the most popular features for human classification, using the images in the INRIA dataset[7].

We have tested this classifier on all the three sequences of images over the annotated BB as positive examples and randomly selected negative BB from the images. The number of negative BB is taken to be twice the number of positives. As seen in table 3.3, the precision[8]of detection is good for all the filters tested while a bigger difference is in the recall[9] values.

Table 3.3: Results of HOG classifier on BB

	Clear	F2	F1
Precision(%)	95.18	94.79	93.85
Recall(%)	59.00	88.12	76.92
F-measure(%)	72.84	**91.33**	84.54

---

[7]http://pascal.inrialpes.fr/data/human/
[8]$Precision = \frac{TruePositives}{TruePositives+FalsePositives}$
[9]$Recall = \frac{TruePositives}{TruePositives+FalseNegatives}$

3.3.3.2   Pedestrian Detection Evaluation

In the previous section we have successfully applied features learned from the visible spectrum to the SWIR in the task of pedestrian classification. In this section we proceed in the evaluation of pedestrian detectors. In order to see the performance of classifiers in the SWIR images we have chosen to test three pedestrian detectors: deformable part models [47, 48], grammar models [59] and HAAR based classifier [87]. Since most of the annotated pedestrians are in medium or near range, the classifier based on deformable part models and the grammar models should be suitable for the task of detecting pedestrians [59]. Both of them are based on HOG as features. The third classifier was chosen in order to evaluate the performance of another state-of-the-art feature, HAAR-like features. All the three classifiers were trained on the INRIA dataset.

A detected BB (BB_{dt}) is considered to be a true positive if it overlaps with a ground truth BB (BB_{gt}) with at least 50% (Pascal measure as used by Dollar et al. [36], see eq. 3.1).

$$\frac{area(BB_{dt} \cap BB_{gt})}{area(BB_{dt} \cup BB_{gt})} > 0.5 \qquad (3.1)$$

Table 3.4: Classifier Comparison in terms of Precision (P) and Recall (R) on SWIR images over all the images

	Part-Models		Grammar-Models		HAAR	
	P(%)	R(%)	P(%)	R(%)	P(%)	R(%)
C	64.89	57.10	67.38	38.77	63.51	7.10
F1	68.51	80.62	71.96	45.64	83.33	3.00
F2	41.21	87.13	79.30	64.19	81.05	6.50

The results obtained for the three different filters are presented in table 3.4. The results vary depending on the classifier and used filter. The part based classifier obtains better results on the scenes taken with C and F1 filter, while with the grammar based classifier better results are obtained on the scene taken with F2 filter. Examples of pedestrian detection results with all the three tested algorithms are presented in fig. 3.7.

Figure 3.7: Image examples from the sequences showing similar scenes and corresponding output results given by the grammar models: C filter range (a), (d), (g), F2 filter range (b), (e), (h) and F1 filter range (c), (f), (i). False positives produced by the algorithm are surrounded by red BB while true positives are in green BB.

Due to differences in terms of pedestrian height in the three sequences acquired, we have also performed a test where we only consider the pedestrians with a height above 80 *px*. This test was chosen due to the fact that some of the pedestrian detectors, like the one based on deformable part models, perform better on close range pedestrians. Moreover this equilibrates the pedestrian heights over the three tested sequences. The results are presented in fig. 3.8. For the grammar model based detector the difference in performance is negligible, having an improvement only for the Clear filter. For the part-based detector the results improve for the Clear sequence but have a drawback in the F1 sequence.
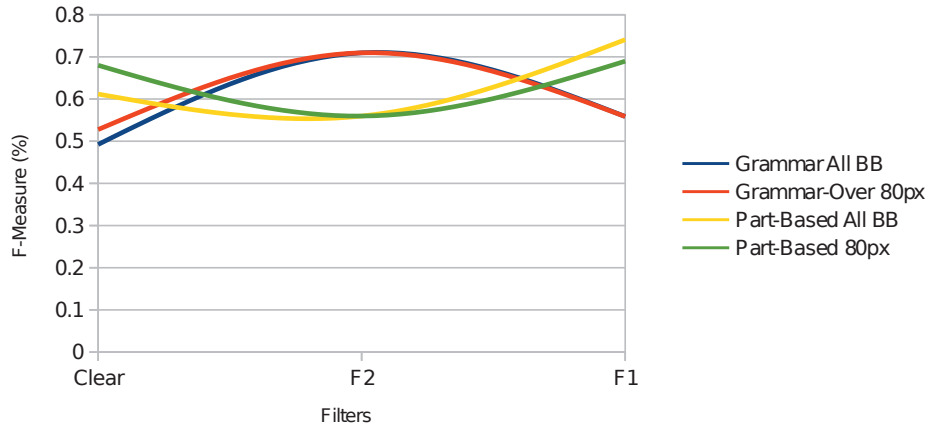
Figure 3.8: Results comparison when testing on all the BB vs. BB surrounding pedestrians over 80 px only.

3.4   SWIR vs Visible: Comparison of pedestrian classification in Visible and SWIR spectrum

In the previous section, we have tried to understand the effects that shorter wavelenghts (SWIR) have upon the task of pedestrian detection and classification. From the filters tested the best results are obtained with F1-filter using the part-based detector followed by F2-filter with the grammar-based detector.

The previous experiments showed that SWIR spectrum might be suitable for pedestrian detection in ADAS context, however we were unable to draw a categorical conclusion whether SWIR can give better results than visible spectrum because we did not have access to visible information from the same scene.

In section 3.3 three different filters (400nm-1700nm; 1300-1700nm; 1000-1300nm) were compared in a scenario with a fixed camera. The background was similar but the annotated pedestrians had different poses. Therefore, for the next experiment we have decided to embed a SWIR camera inside a vehicle along with a camera in the Visible spectrum. This will guarantee the information captured in the two domains to be similar, even if we will not have exactly the same point of view of the scene for the two cameras. The purpose of this acquisition setup was to construct a benchmark in order to compare the pedestrian classification in the two light spectrums: Visible and SWIR.

Previous works that compare visible and infrared light spectrums are mostly focused in the long-wavelength infrared or far-infrared. To this day, from our knowledge there doesn't exist

previous works that benchmarks the SWIR and Visible spectrum in a quantitative manner for the task of pedestrian detection in the ADAS context.

Characteristic	Value
Pixel Resolution	320×256
Input Pixel Size	30 microns square
Spectral Response	$950nm$ to $1700nm$
Peak quantum efficiency	approximately 80% at $1000nm$
Gray Scale Resolution	16 bits
Pixel frequency	10MHz
Exposure Time	From $< 10\mu sec$ to > 1 second
Control	RS232 via GigE
Power requirements	110 or 230V ac 50/60Hz less than 50W
Operating Environment	*Operation Temperature:* $0°C$ to $+50°C$; *Humidity:* $0 - 80\%$ RH non-condensing

Table 3.5: Camera specification

3.4.1 Hardware equipment

For the experiments presented in this section we have used a SWIR InGaAs camera with a format of 320×256 pixels. The camera is based on a Indium Gallium Arsenide technology and provides a sensitivity in the 950 nm to 1700nm waveband. The most important camera parameters are presented in table 3.5. The quantum efficiency is usually superior of 70%, having a peak of 80% at $1000nm$.

Unlike the previous experiment, the temperature of the sensor in this camera is reduced using a peltier cooler along with a secondary air cooling system. The cooling is necessary in order to reduce the build-up of thermally generated dark current. Therefore the camera is able to cope with extended exposure periods thus providing high sensitivity for faint signals.

The camera uses a digitisation of the CCD signal to 16 bits at $10MHz$ pixel frequency. The

maximum frame rate at a short exposure time is over 20 fps.

3.4.2 Dataset overview

We have collected two separate sequences of images, one used for training (*Sequence Training*) and the other one for testing (*Sequence Testing*), using two cameras: the SWIR camera described in the previous subsection, and a color camera. These were placed side by side, at a distance of approximately 10*cm*, inside the car. We will further refer to this dataset as RISWIR[10]

The cameras were not synchronized from a hardware point of view (due to logistic problems), but rather as a post processing step performed after the image acquisition. Because there were used two separate cameras, some small differences could be observed in the scenes captured: objects visible in one camera are not always present in the other ones view. This, along with differences in the focal length of the two cameras, have made the annotation process cumbersome: each object (both positive and negative instances) had to be annotated manually in two separate views.

	Sequence Train	Sequence Test	Overall
Number of frames	7049	3150	10199
Number of unique **pedestrians**	65	13	78
Number of annotated **pedestrian BB**	8618	1753	10371
Average pedestrian duration (frames)	132	134	133
Number of **pedestrian BB** visible in both cameras	6892	1372	8264
Number of **pedestrian BB** with height > 32 px	**4743**	**1023**	5766
Number of **negative BB** annotated	**6675**	**3219**	9894

Table 3.6: RISWIR Dataset statistics

In the training sequence we have annotated a total of *8618 BB* corresponding to pedestrian instances and *6675 BB* corresponding to non-pedestrian areas, while in the testing set a number of *1753* pedestrian BB and *3219* non-pedestrian BB were annotated. As presented in table 3.6 the number of unique pedestrians is of *65* in training and *13* for testing. Also, the average presence duration of a pedestrian in the sequences, is around *130* frames.

In order to test if the training and testing sequences contain pedestrians similar in appearance we have plotted the histogram of heights for the training and testing sequence, taking bins of 25

---

[10]It is publicly available at the following web address: `www.vision.roboslang.org`
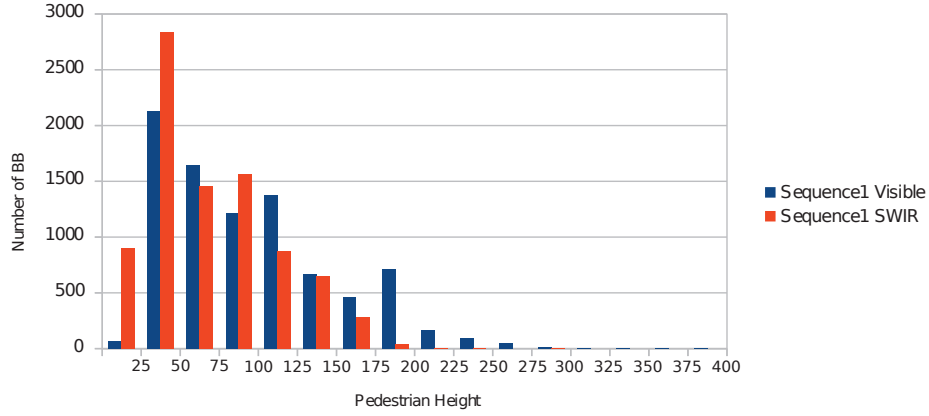
Figure 3.9: Height distribution for the Training Sequence
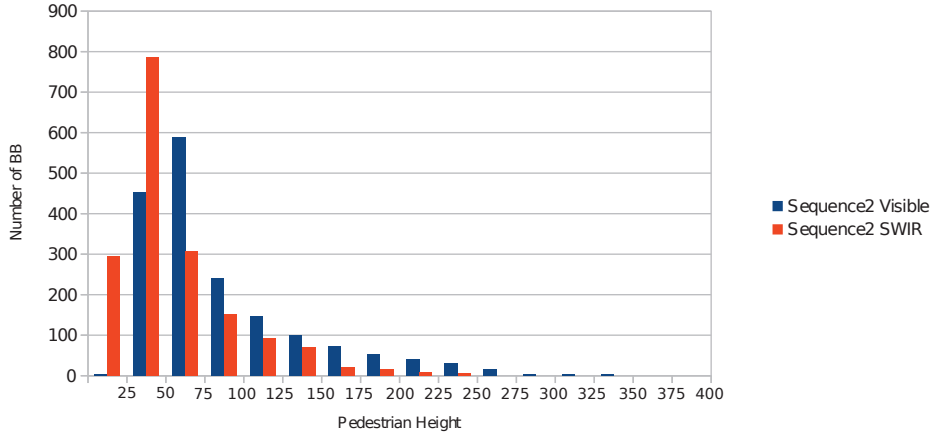
Figure 3.10: Height distribution for the Testing Sequence

pixels. As it can be observed from figure 3.9 and figure 3.10, most of the annotated pedestrians have a height in the interval $[25 - 100]$ pixels.

In figure 3.11 we have plotted the normalized heat-map of annotated pedestrians in both SWIR (3.11b,3.11d, 3.11f) and visible (3.11a, 3.11c, 3.11e).

Our purpose is to compare as accurate as possible classification rate of pedestrians in SWIR and visible images. Therefore, we have only taken into consideration those BB that have a correspondence in both SWIR and Visible images. Also, as shown in [36], pedestrians with a height under *32 pixels* are nearly impossible to detect, therefore we have eliminated these instances from both training and testing. For the final dataset we kept *4743* positive instances and *6675* negative examples for the training set, and *1023* positive instances and *3219* negative examples for the testing. In order to facilitate testing, all the considered BB were scaled at a

(a) Training Visible

(b) Training SWIR

(c) Negatives Visible

(d) Negatives SWIR

(e) Testing Visible

(f) Testing SWIR
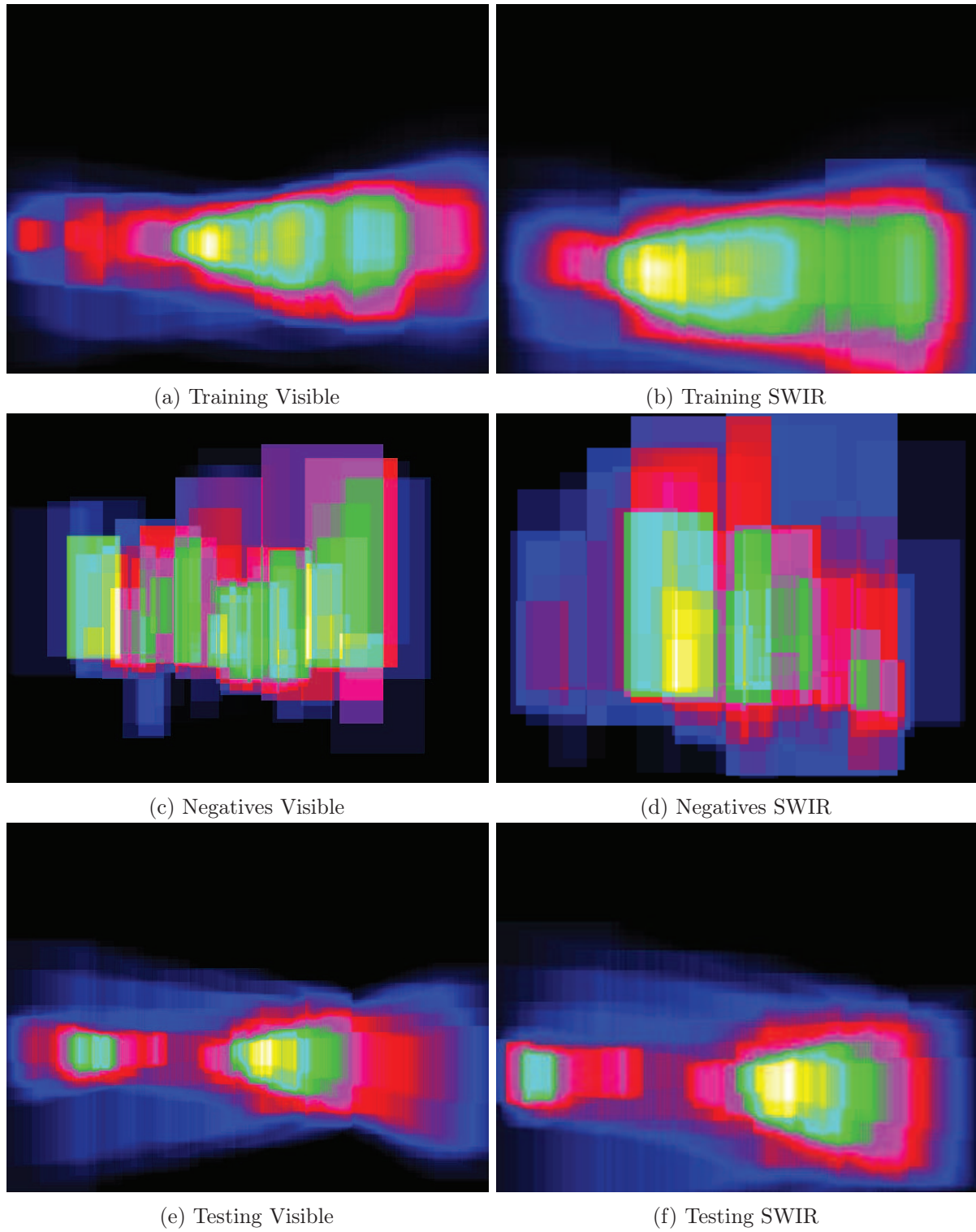
Figure 3.11: Heat map given by the annotated pedestrians across training/testing and SWIR/visible.

Figure 3.12: Examples of images from the dataset: a),c) Visible domain and the corresponding images from the SWIR domain b),d)

dimension of 48×96 pixels.

3.4.3 Experiments

The reference point for any pedestrian classification experiment is the performance of different features in the Visible domain. Following this line, in figure 3.13 is ploted the classification rate versus the false positive rate for three features: HOG, LBP and LGP. The reference point of comparison is the false positive rate for a 90% classification rate.

In the Visible domain, HOG features seem to be the most robust tested feature with a false positive rate of 0.41. This is followed by the LBP with a false positive rate of 0.56 and LGP with 0.6. Fusing different features, in the visible domain, lowers slightly the error rate (figure 3.14). Even if LGP feature had the highest false positive rate when testing each feature independently on the Visible dataset, in combination with HOG, has a better performance than the fusion of LBP and HOG. The lowest error rate is obtained by combining all three features.
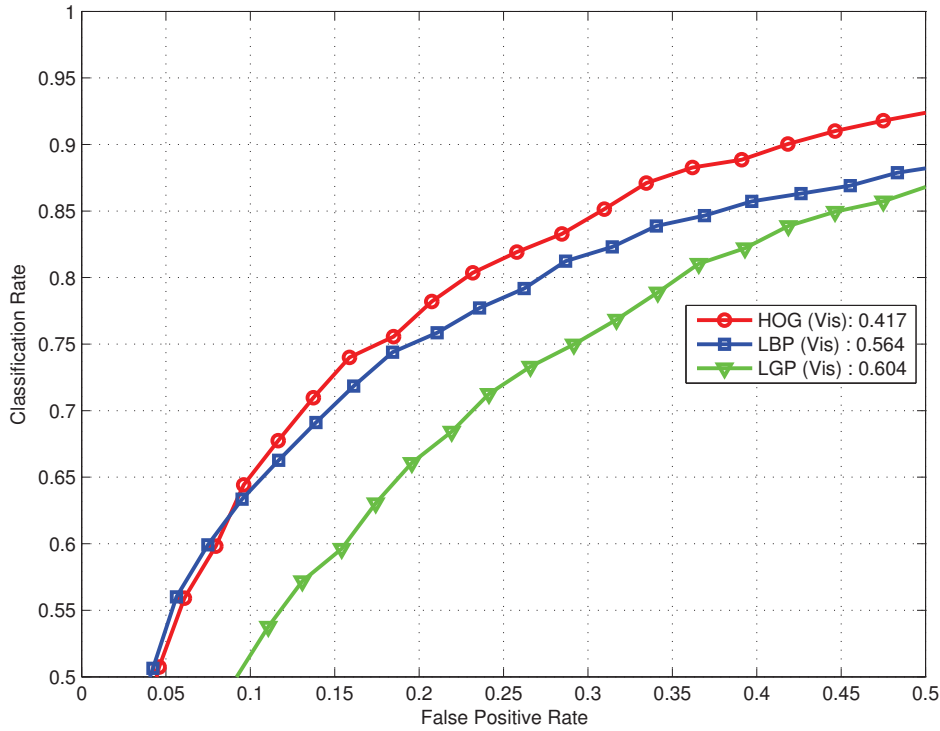
Figure 3.13: Feature performance comparison in the Visible domain. The reference point is considered the obtained false positive rate for a classification rate of 90%.

In what concerns the situation in the SWIR domain, see figure 3.16, LBP and LGP have a better performance than HOG. The leading feature now is LBP with a false positive rate of 0.25, followed by LGP with 0.29. HOG feature has a false positive rate of 0.31. It can be observed that all three features have a better performance in the SWIR domain than in the Visible one. Moreover, in the SWIR domain the feature fusion has a highest impact than the counterpart in Visible (figure 3.16) . Once more, the combination of HOG and LGP (with a false positive rate of 0.12), gives better results than the combination of HOG and LBP (with a false positive rate of 0.16). Like in the case of Visible, the lowest error rate is obtained by combining all three features.

Other fusion strategies, like fusing for each feature the Visible and SWIR domain (figure 3.17) or combining several features with both Visible and SWIR (figure 3.18) doesn't seem to lower the false positive rate.

3.4.4   Discussion

The results presented in this chapter show some promising prospects for the SWIR domain. On the collected dataset, features computed on SWIR images had a lower false positive rate than the once compute in the Visible domain.

73
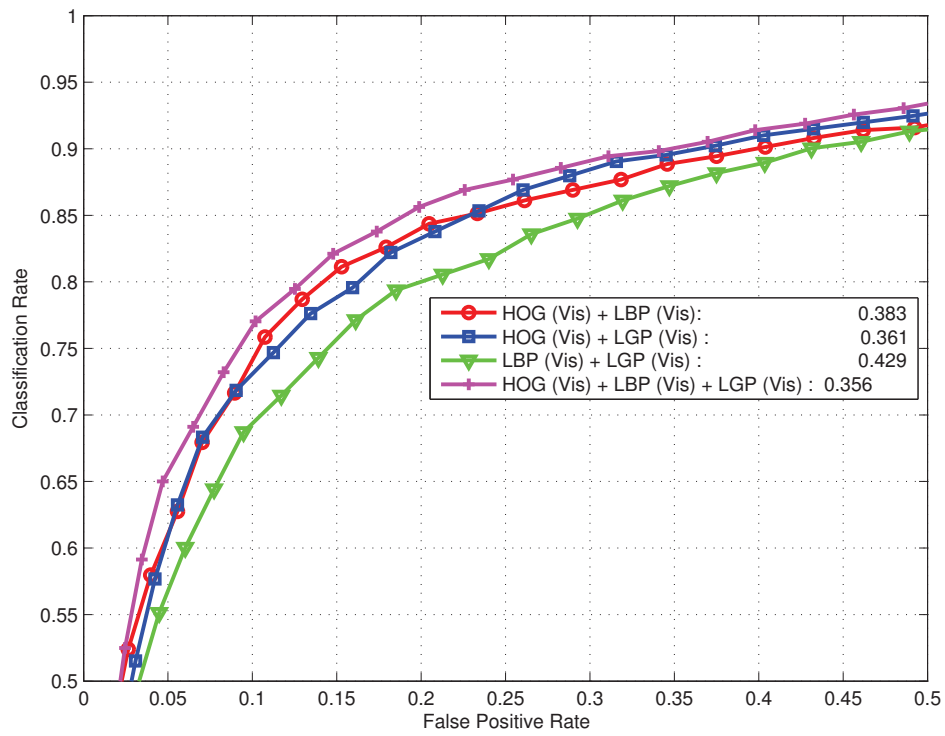
Figure 3.14: Comparison of feature fusion performance in Visible domain. The reference point: classification rate of 90%.
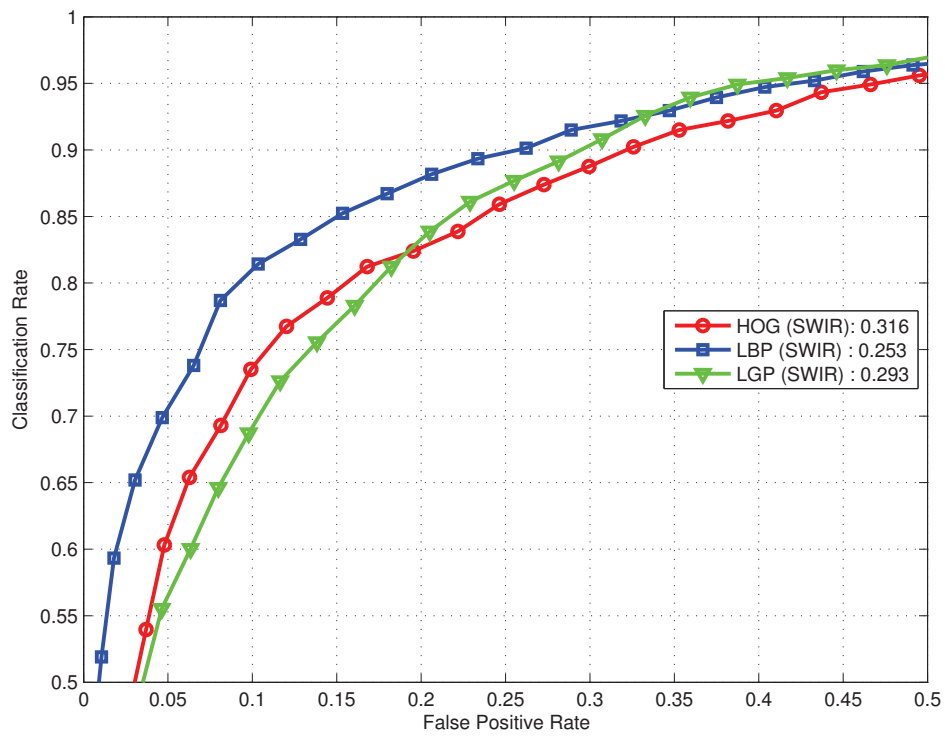
Figure 3.15: Feature performance comparison in SWIR domain. The reference point: classification rate of 90%.
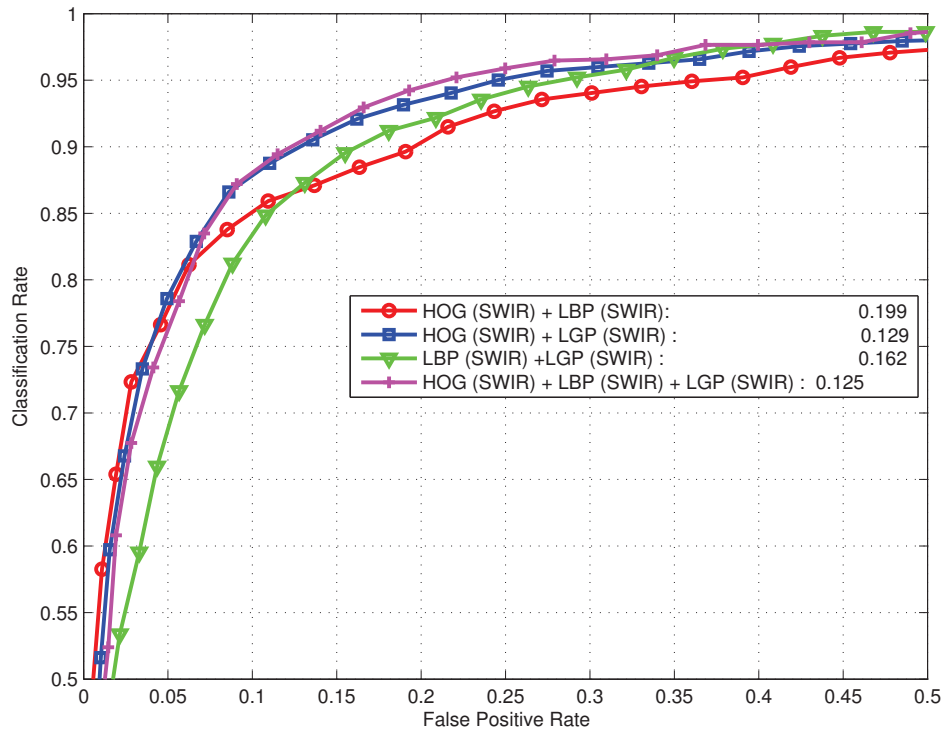
Figure 3.16: Comparison of feature fusion performance in SWIR domain. The reference point: classification rate of 90%.
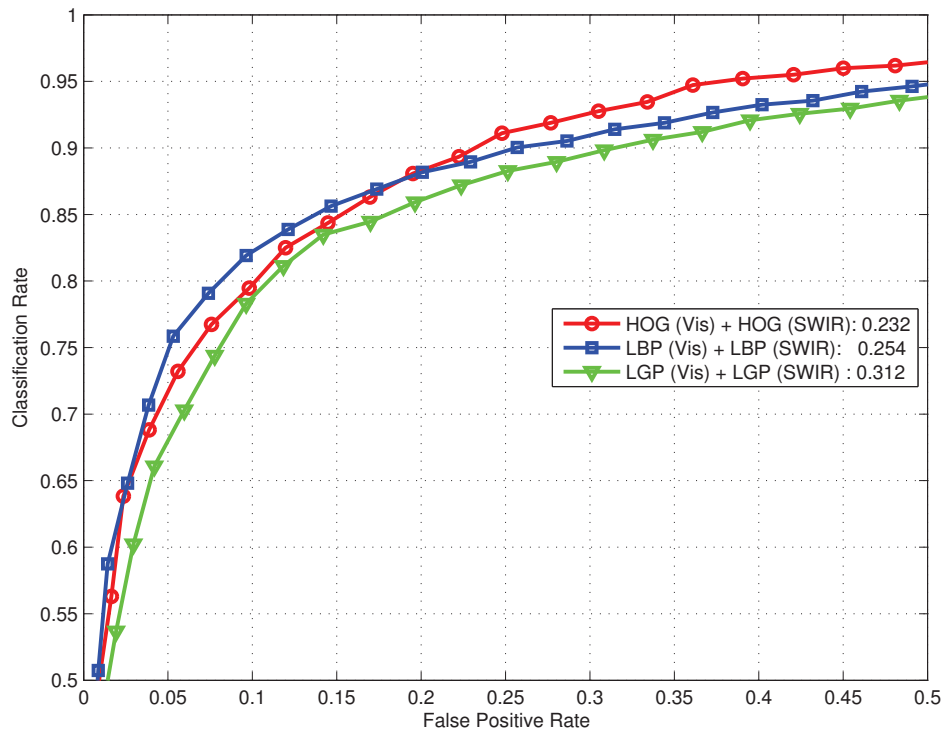
Figure 3.17: Comparison of Domain fusion performance for different features. The reference point: classification rate of 90%.
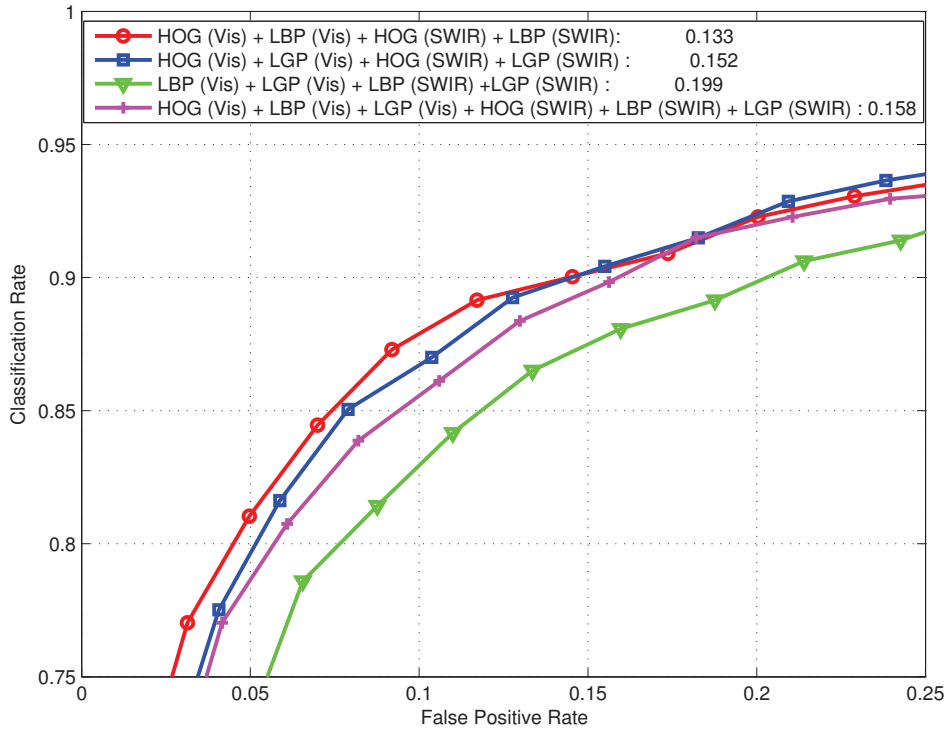
Figure 3.18: Comparison in performance of Domain and different feature fusion strategies. The reference point: classification rate of 90%.

First, we have tested HOG, LBP and LGP independently on each domain. On the Visible domain, HOG features had the best results, whereas in the SWIR domain LBP worked better.

Second, we have tested feature fusion on the same domain. Using different features from both modalities, the combination of HOG and LGP gave better results than HOG and LBP, for both Visible and SWIR.

Third, we have assessed the performance of fusing the two domains, Visible and SWIR, along different features. This fusion didn't have a great impact over the false positive rate. The overall best results were obtained by the combination HOG, LGP and LBP on the SWIR domain, but very close results were obtained with just the combination of HOG and LGP.

A possible explanation for the obtained results is that, on the collected dataset, the SWIR images, although captured at a much lower resolution (320×256), have sharper edges than the Visible ones. It should be noted that the acquisition of the dataset was done in a cloudy day (therefore, a lower level of light). This might have an impact (increased noise) over the quality of images obtained from the Visible camera.

3.5   Conclusions

In this chapter, we have studied the problem of pedestrian classification and detection in the SWIR domain. Also, we have acquired a dataset with images in both SWIR and Visible, thus allowing as to perform a comparison of the two domains. Our tests show that the SWIR domain might be promising for ADAS applications, but more tests should be performed in different meteorological conditions, in order for a decisive conclusion to be drawn.

Also, further evaluations of the SWIR wavelengths should include night vision. Because the O-H molecules floating in the upper atmosphere radiates energy at various intensities throughout the night, night vision on moonless nights is possible in the long wavelengths. These emissions enable night-time vision under the passive illumination of the sky. This could make SWIR imagers very suitable for automotive applications as a valid alternative to current systems based on cameras sensible to Near InfraRed wavelengths (NIR) or thermal cameras sensible to the Far InfraRed ones (FIR). These sensors present some important disadvantages: NIR cameras need special IR illuminators integrated in the vehicle to illuminate the area in front of it, whereas FIR cameras do not have this limitation but are still inherently expensive sensors for high resolution specifications. The SWIR technology can be considered somewhat in between these two extremes, featuring good resolution images at affordable prices for current automotive applications and at the same time showing wider ranges scenarios than NIR cameras benefiting of the night sky's natural infrared glare, which shines within the SWIR range.

Until now, we have studied pedestrian classification in FIR and SWIR spectrums. While in FIR the pedestrian hypothesis search space can be reduced using for example intensity threshold (pedestrians will usually appear as hot regions in the image), in Visible and SWIR domains, this isn't the case. One technique that has the capability of generating fewer hypothesis, is the use of 3D vision. By using depth information, pixels found at a certain distance can be efficiently extracted. Moreover the extraction of objects of interest from noisy visual background can be greatly simplified. In the next chapter we are going to focus on the algorithms of depth computation through Stereo Vision.

But yield who will to their separation,

My object in living is to unite

My avocation and my vocation

As my two eyes make one in sight

Two tramps in mud time

Robert Frost

4

Stereo vision for road scenes

Contents

Stereo vision can represent a low cost solution for the problem of reducing the pedestrian hypothesis search space. The use of depth information can eliminate effects of shadows, distinguishing objects at different range distance from the camera (for example a pedestrian that is partially occluded by a passing car), identifying moving and stationary objects. In this chapter we are going to study more in depth the algorithms of stereo vision. After presenting an introduction

into this field of research, we are going to focus on improving different aspects of the algorithm of stereo matching, with a particular emphasis on road scene scenarios.

Stereo vision/Stereopsis (from the greek words: *stereos*[1] meaning *solid*, with reference to three-dimensionality, and *opsis* meaning *view*) refers to the extraction of depth information from a scene when viewed bye a two camera system (eg. human eyes). When an object is viewed from a great distance, the optical axes of both eyes are parallel, therefore the object's projections, as seen by each eye independently, is similar. On the other hand, when the object is placed near the eyes, the optical axes will converge. When a person looks at an object, the two projections converge so that the object appears at the center of the retina in both eyes resulting in a three-dimensional image[2].

From an evolutionary point of view, animals developed stereo vision in order to perceive relative depth rather than absolute depth [124]. Therefore, from a biological point of view, it seems that stereo vision is used mostly in recognition and less in controlling goal-directed movements.
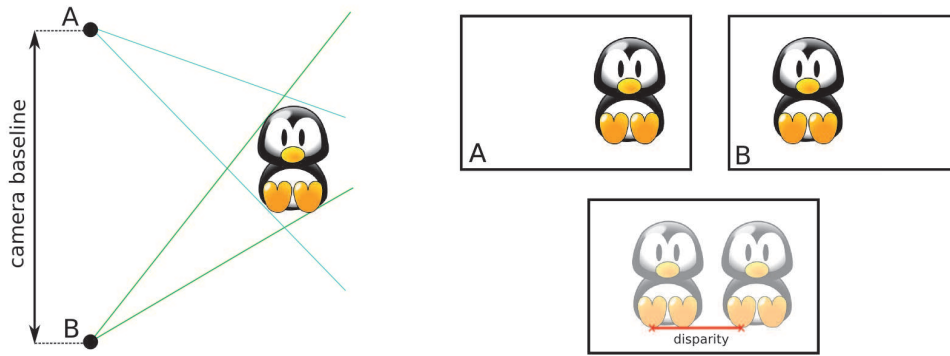
Figure 4.1: An object as seen by two cameras. Due to camera positioning the object can have different appearance in the constructed images. The distance between the two cameras is called a *baseline*, while the difference in projection of a 3D point scene in each camera perspective represents the *disparity*.

A task that is learned so easily by the human brain and performed unconsciously has proven to be difficult for computers. In traditional computer stereo vision, two cameras are placed horizontally at a certain distance in order to obtain different views of the scene (figure 4.1). The distance between the cameras is called baseline and influences the minimum and maximum perceived depth. The amount to which a single pixel is displaced in the two images is called disparity and it is inversely proportional to its depth in the scene: closer objects will have greater

---

[1]http://dictionary.reference.com/browse/stereo-

[2]A study published by Richards [108] shows that at least 3% of persons posses no wide-field stereopsis in one hemisphere

disparity than background objects.

Computer stereo vision has various applications, from studying planets and stars[3] to car navigation (Porter Car from VisLab intercotinental challenge) or robot navigation[77].

4.1 Stereo Vision Principles

4.1.1 Pinhole camera

As described by Forsyth and Ponce [51], a pinhole camera is the simplest model, where the lens are represented by a single point in 3D space. This will allow to exactly one light ray to pass through the pinhole, connecting a scene point to a single point in the image plane (see figure 4.2).
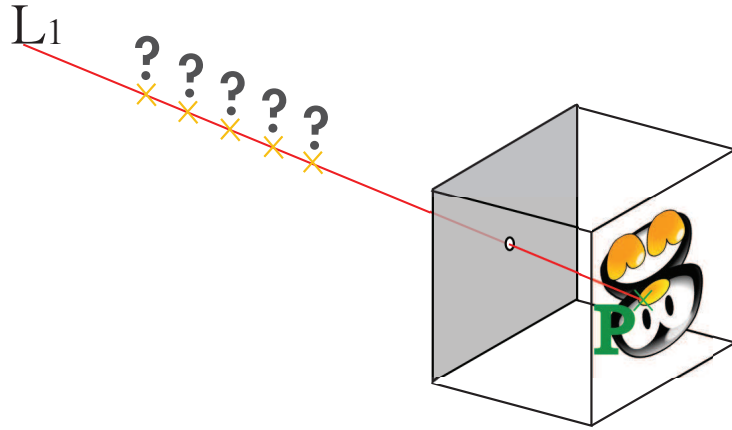
Figure 4.2: Pinhole camera. With a single camera, we cannot distinguish the position of a projected point (P) in the 3D space (L1).

In this model the position of the point in the three-dimensional space can not be approximated because it could lie anywhere on the line $L1$ as seen in figure 4.2. If we introduce into the model a second pinhole camera (figure 4.3) we are able to infer the position in space of a certain point in the image by intersecting the two corresponding rays, $L1$ and $L2$. Unfortunately, the difficult part of this approach is to match the corresponding points in the images obtained with the two cameras.

To solve the correspondence problem we need to search in a 2D image space. Unfortunately, this approach has an exponential running time. By introducing the constraint of rectification, the images are transformed by projection onto a common image plane. This will transform from a 2D search into one of finding corresponding points on the same line (epipolar constraint). This is why almost all the algorithms assume that the images have been rectified.

---

[3]NASA Solar TErrestrial RElations Observatory (STEREO): Studying the sun in 3D
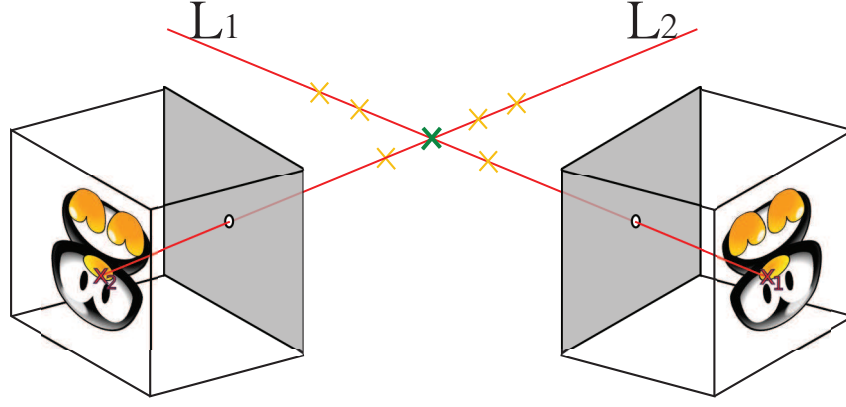
Figure 4.3: Stereo cameras. If we are able to match two projection points in the images as being the same, we can easily infer the position of the considered 3D point by simply intersecting the two light rays (L1 and L2)

4.1.2   Stereo vision fundamentals

Stereo matching is the process of inferring 3D scene structure from two or more images acquired from different viewpoints.

The output of the most stereo correspondence algorithms consists in a disparity map $d(x,y)$[4] that specifies the relative displacement of matching points between images. The (x,y) pair represents the coordinate of a disparity space and they coincide with the pixel coordinates for the reference image. To find the corresponding pair of coordinates (x',y') in the second image (the matching image), of the given pixel, we will use the equation 4.1:

Given that x'=x (epipolar constraint and rectified images),

$$y' = y + sign * d(x,y) \qquad (4.1)$$

where sign is +1 or -1, such that the disparity to be always positive.

The stereo matching algorithms could be divided into *feature-based* (which try to find features as edges and match them afterwards leading to a sparse disparity map) and area-based algorithms (which try to match each pixel leading to a dense disparity map). The main advantage of algorithms that produce sparse disparity map is usually their speed, while the main disadvantage is that even in the case of feature matching the error rate can be quite high and it tends to propagate in latter stages of the algorithms. In the case of algorithms that produce dense disparity maps they can have a significant running time depending on the accuracy of the disparity map

---

[4]Disparity was originally referring to the difference in image location of an object seen by the left and right eyes.

obtained, but good results in real-time were achieved using either CPU processing [64] or the most popular GPU[5] programming[93]. Still, designing a stereo matching system with good trade off between accuracy and efficiency remains a challenging problem. In what follows we are going to present some of the main difficulties faced by the stereo matching algorithms and also present a short state of the art of the current methods and techniques.

As presented in [112], most of the stereo matching algorithms are following four steps:

1. Computation of a matching cost function

2. Support zone cost aggregation

3. Disparity computation through cost minimisation

4. Disparity refinement

Figure 4.4 shows an example of a basic stereo matching algorithm. In this example the cost taken in consideration is the absolute difference of intensities. Because this cost is not very discriminative, an aggregation area represented by a squared window of 3×3 pixels is used. Inside the aggregation area all the pixels are considered to have the same disparity. Therefore, in order to compute the cost for a pixel to have a disparity d with the help of a squared aggregation area, the sum of individual costs is computed for each pixel in the aggregation area to have the disparity d using the absolute difference of intensities. The following step is to find the disparity at which the cost will be minimised. This is just a simple example of a stereo matching algorithm. In practice, because the problem of stereo matching is an NP complete one, even if we have found for each pixel the disparity that minimizes the cost for the pixel, this does not mean that the found disparity corresponds with the ground truth.

4.1.2.1 Stereo matching difficulties

The problem of stereo matching has an ill-posed nature [107] therefore it is still challenging to obtain an accurate disparity map. Some of most difficult situations are given by:

- **Radiometric distortions.** Radiometrical differences or distortions are the situations where corresponding pixels have different intensity values. The assumption that pixels, in the two stereo images, corresponding to the same scene will have same brightness holds only for the Lambertian surfaces, i.e. surfaces that have the same brightness regardless of the viewing angle. In practice, non-Lambertian surfaces are quite frequent. Moreover,

---

[5]GPU - Graphical Processing Unit. Currently the main framework for GPU programming is CUDA provided by NVIDIA
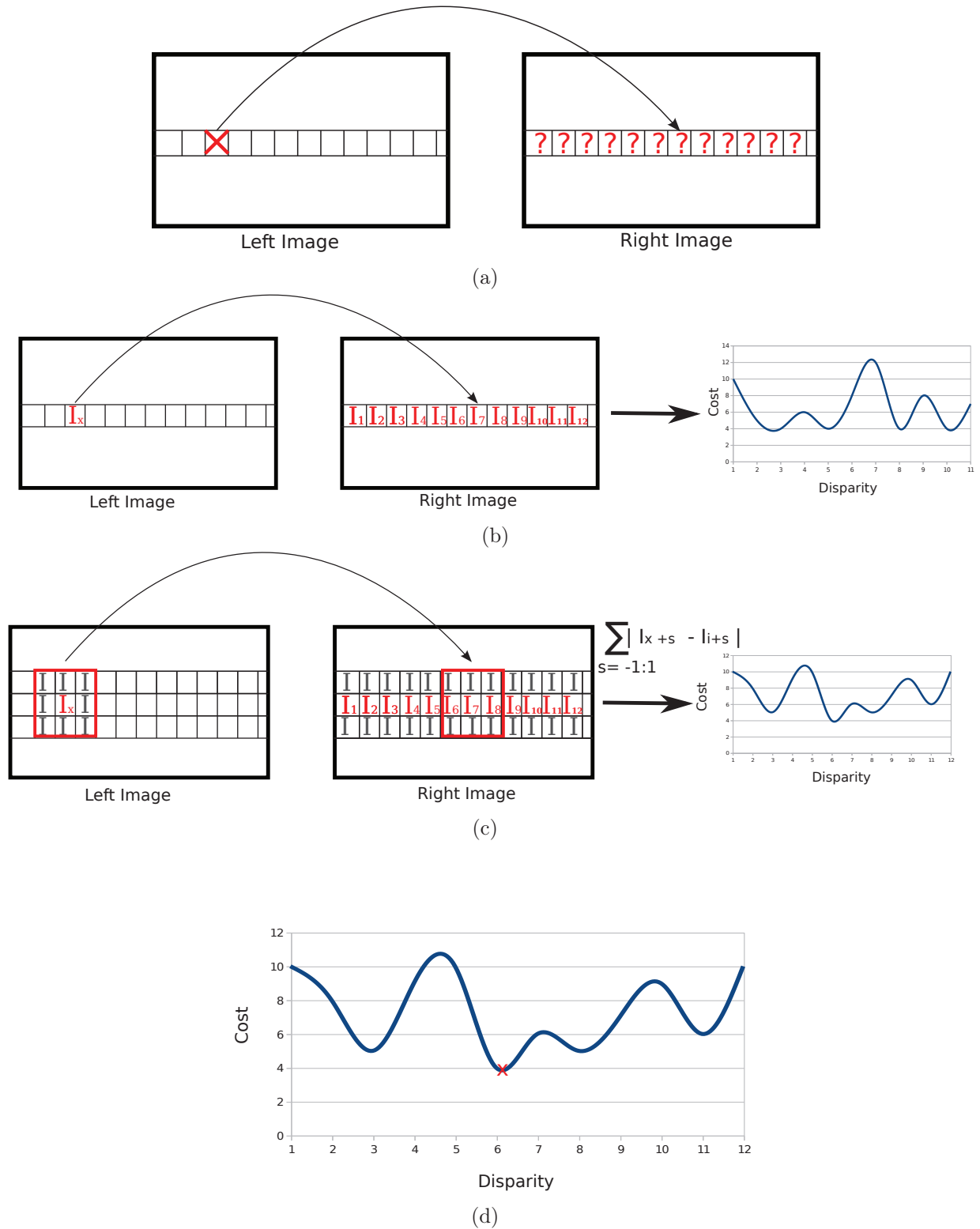
Figure 4.4: Basic steps of stereo matching algorithms assuming rectified images. a) The problem of stereo matching is to find for each pixel in one image the correspondent in the other image. b) For each pixel a cost is computed, in this example the cost is represented by the difference in intensities. c) A cost aggregation represented by a squared window of 3×3 pixels. d) The disparity of a pixel is usually chosen to be the one that will give the minimum cost.

radiometrical distortions are also caused by camera parameters (aperture, sensor) which can give different image noises or vignetting.

- **Ambiguity.** In order to find two corresponding pixels, a cost has to be used that discriminates the matching pair from the other possible matches. Unfortunately, it is difficult to find such a cost in order to match untextured regions, i.e. a white wall. Moreover, repetitive patterns pose also a problem due to the fact that several points become viable candidates for matching, thus creating an ambiguity.

- **Occlusions.** The problem of finding a corresponding pixel becomes even more difficult when in fact that pixel does not really exist. Occlusions, i.e. situations where a pixel is visible in one of the images but not in the other, are frequent at depth discontinuities. Also, an object that is situated close to the point of view will cause occlusions for an object situated behind it.

Therefore, due to the challenges of the stereo matching given by textureless areas, occluded regions, reflective surfaces, sun glares, a stereo matching algorithm that simply uses the intensity values of the pixels like illustrated in figure 4.4 will give a result with a high error rate.

A few examples of images taken in real road conditions, that we consider to be a challenge for stereo matching algorithms, like textureless areas, repetitive patterns, sun glares, high contrast or reflective surfaces, are presented in figure 4.5.

4.1.3 Stereo matching Algorithms

Computer stereo vision has been a domain studied for a long time, thus a considerable amount of literature exists. Like presented in subsection 4.1.2, the stereo matching algorithm will usually follow four main steps: cost computation, cost aggregation, disparity computation through cost minimisation and disparity refinement.

If we take into account only the cost minimisation/optimisation step, a division of the stereo matching algorithms into *local* and *global* can be performed. In order to explain the difference between local and global algorithms one has to understand the *smoothness assumption*.

Most of the images depicting natural scenes show objects with a smooth surface. Therefore the assumption that can be made is that across an object like a lamp or person, the disparity will be the same or similar. This is defined as the *smoothness assumption* [92], i.e. spatially close pixels that have similar or the same disparity. The smoothness assumption can be implicit as in the case of local stereo matching algorithms or explicit, as it is the case of global ones.

Figure 4.5: Challenging situations in stereo vision. The images a)-h) are extracted from the KITTI dataset[57], while the images i)-l) from HCI/Bosh Challenge [95]. The left column represents the left image from a stereo pair, and the right column the corresponding right image.: a)-b) Textureless area on the road caused by sun reflection; c)-d) Sun glare on the windshield produces artefacts; e)-f) "Burned" area in image where the white building continues with the sky region caused by high contrast between two areas of the image; g)-h) Road tiles produce a repetitive pattern in the images; i)-j) Night images provide fewer information; k)-l) Reflective surfaces will often produce inaccurate disparity maps

4.1.3.1   Local stereo matching

The implicit smoothness that is made by the local methods assumes the fact that all the pixels in the defined zone of aggregation have constant disparity. When searching for a match of a given pixel, a window (or the chosen zone of aggregation) is shifted across the corresponding scanline from the other view.

Most of the time, the final disparity is obtained by using the winner-takes-all strategy, i.e. finding the point that will minimize the matching cost (see equation 4.2).

$$d_p = min_{d_{min} \leq d \leq d_{max}} \sum_{q \in N_p} c(q, q - d) \tag{4.2}$$

where

- d_p is the final disparity assigned to pixel p

- d_{min} and d_{max} is the minimum possible disparity, respectively maximum.

- N_p represents the neighbourhood of pixel p that is taken as aggregation area

- $c(q, q - d)$ represents a cost between the pixel q in the left image and the corresponding pixel at disparity d in the right image

Because local stereo matching methods usually go hand in hand with the step of cost aggregation, we will describe the local stereo matching algorithms according to the aggregation area chosen.

Window-based aggregation

In the window-based aggregation approach the neighbourhood area is usually represented by a square window of user-defined size. The main advantage of this approach is the fast computation time.

Unfortunately, the approach has several disadvantages. The first problem with the window-based aggregation is in the disparity discontinuities regions as shown in figure 4.6. The main assumption of the local methods is that all the pixels in the defined aggregation area have the similar disparities. This assumption will not hold in disparity discontinuities regions and has as effect foreground fattening and implicitly errors in the disparity map.
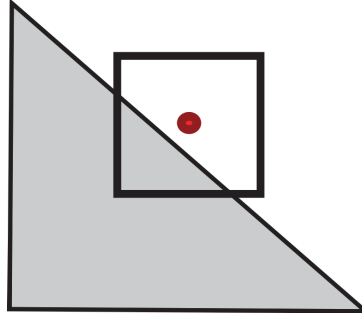
Figure 4.6: Disadvantage of square window-based aggregation at disparity discontinuities. In red is the pixel, and the square is the corresponding aggregation area.

Another problem is with choosing a good window size. A big window will increase the computation time, but it will capture more texture. A small window size will provide a fast running time but it is less likely to capture discriminative features. Moreover, *big* or *small* are relative concepts depending on the type of scene and image size.

Several algorithms have been proposed to resolve the problems of square window aggregation. A solution for choosing the right window size was proposed in the form of adaptive window size [53], [68], while for the systematic errors that can be found at disparity discontinuities a possible solution is offered by adaptive support [135],[69].

Adaptive Windows

Fusiello et al. [53] proposed a method that improved the classical window-based correlation by the use of nine different windows. The pixel, for which the disparity is computed, is no longer centred in the aggregation window, but it has different positions. The purpose is to find the best window that will not violate a disparity discontinuity, and thus the idea is that the smaller the cost error is, the greater is the chance that the window found covers a region of constant depth. The disparity with the smallest cost error per window is retained.

Another approach is not to have different windows, but to divide a centred aggregation window in nine parts, like proposed by Hirschmüller et al. [68]. The presumption is that not all the parts in an aggregation window are equally relevant. Therefore, the matching score is computed by retaining only the best five costs of the sub-windows.

The disadvantage of these approaches remains choosing of a good window size. Moreover, not always a window that does not violate the disparity discontinuity can be found or that five sub-parts are always relevant in an aggregation window.

Adaptive Support Weight Approach

Extending the idea proposed by Hirschmüller et al. [68] that not all the sub-parts of an aggregation window should contribute to the final score, techniques that associate to each sub-part a weight were proposed. Therefore, if in the classical window-based aggregation all the pixels have the same influence over the matching cost (equation 4.3), in the *adaptive support weight approach* a weight $w(p,q)$ is used to determine the likelihood of two pixels, p and q, to have the same disparity (equation 4.4).

$$C_{(p,d)} = \sum_{q \in N_p} c(q, q - d) \tag{4.3}$$

$$C_{(p,d)} = \sum_{q \in N_p} w(p,q) * c(q, q - d) \tag{4.4}$$

The main advantage of this method is that the foreground fattening is removed but another problem arises: *how to compute the weights?*

The usual assumption is that two points are likely to have the same disparity if they have similar colors and if they are similar in spatial positions.

Yoon and Kweon [135] proposed a function for the weight computation that takes advantage of both color similarity and the spatial distance between two pixels (equation 4.5). This method has as advantage the fact that it provides good results at disparity discontinuities regions, but unfortunately has a high computational cost.

$$w(p,q) = exp(-(\frac{\delta c_{pq}}{\gamma_c} + \frac{\delta g_{pq}}{\gamma_g})) \tag{4.5}$$

where

- δc_{pq} computes a color dissimilarity

- δg_{pq} computes the euclidean distance

- γ_c and γ_q are user defined parameters

Because the euclidean distance between two pixels does not enforce two pixels to actually be on the same surface, a solution was proposed in [69] by taking into consideration geodesic distances. A geodesic distance represents the shortest path that connect two pixels, p and q in color.

$$w(p,q) = exp(-\frac{D(p,q)}{\gamma}) \tag{4.6}$$

where

- $D(p, q)$ denotes the geodesic distances

- γ is a user defined parameter

Cross-based aggregation

The drawback of aggregation areas that take into consideration both color and euclidean or geodesic distances is the high computation time. Zhang et al. [137] proposed an efficient technique based on cross-zone aggregation for computing a pixel aggregation region, that takes into consideration both color and euclidean distances.

The idea behind is to construct a *cross* region for each pixel. For this, it is necessary to find only four pixels, corresponding to the end of the four arms: up, down, left and right (figure 4.7.a). Then, in order to construct a region of various shapes, for each pixel that lies on the vertical arm, the horizontal arm will give the region boundaries for the specific row (figure 4.7.b, 4.7.c).

In order to choose an arm endpoint p_e for a given pixel **p**, two rules are applied that pose limitations on color similarity and maximum arm length:

- $D_c(p_e, p) < \tau$. τ is a user-defined threshold value, while the color difference is defined to be $D_c(p_e, p) = max_{i \in R,G,B}|I_i(p_e) - I_i(p)|$.

- $D_s(p_e, p) < L$. L is a user-defined threshold value and represents a maximum length in pixels. $D_s(p_e, p)$ is a spatial distance given by $|p_e - p|$.

After having the cross region for each pixel, the next step is to compute the cost in the defined region. For this, the cost aggregation is computed in two steps. First the horizontal matching cost is computed and stored (figure 4.8.a), secondly the final cost is obtained by aggregating the intermediate results vertically (figure 4.8.b). The two steps can be efficiently computed using $1D$ integral images.

4.1.3.2 Global stereo matching

Global methods of stereo matching define the problem as a energy minimization problem. The most common form of the energy function is:

$$E(D) = E_{data}(D) + E_{smooth}(D) \tag{4.7}$$
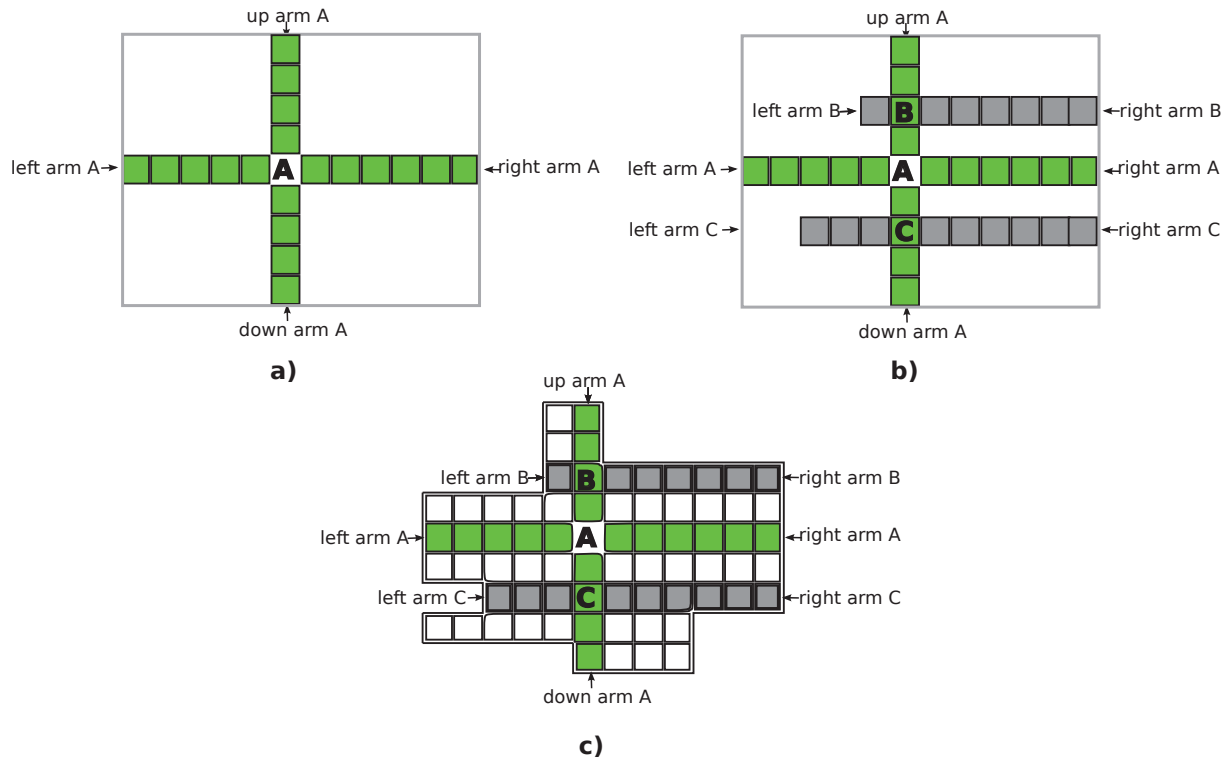
Figure 4.7: Cross region construction: **a)** For each pixel four arms are chosen based on some color and distance restrictions; **b)**,**c)** The cross region of a pixel is constructed by taking for each pixel situated on the vertical arm, its horizontal arm limits.
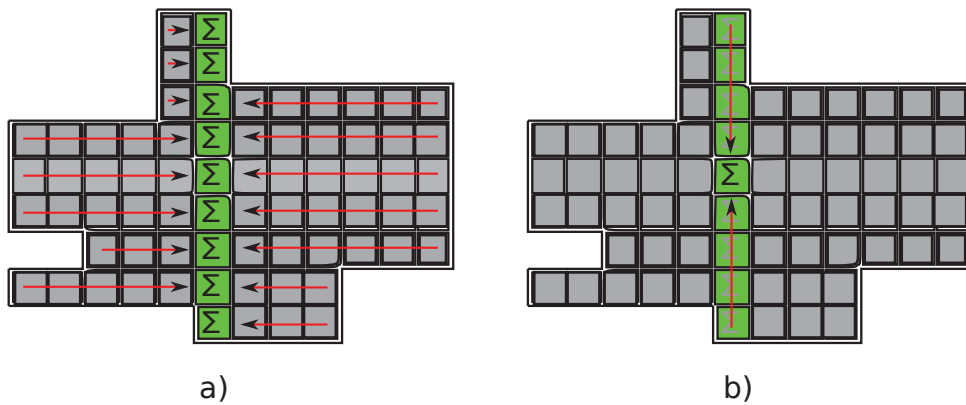
Figure 4.8: Cross region cost aggregation is perfomed into two steps: first the cost in the cross-region is aggregated horizontally **b)** and then vertically **b)**

where D is the disparity map of the image (left), E_{data} is the member that measures the consistency of the disparity map, and E_{smooth} is a term that computes the smoothness.

Usually the data term measures a color dissimilarity, but other cost functions can be considered.

$$E_{data}(D) = \sum_{p \in I} c(p, p - d_p) \tag{4.8}$$

, where d_p is the disparity of p in the disparity map D, and the $c(p, p - d_p)$ computes a cost (for example color dissimilarity) between pixels of left and right images.

In what concerns the smoothness term, which is computed explicitly in global methods, it is described by equation 4.9.

$$E_{smooth}(D) = \sum_{<p,q> \in N} s(d_p, d_q) \tag{4.9}$$

where N represents the set of neighbouring pixels and s is a smoothness function that imposes a penalty if two disparities are different.

$$s(d_p, d_q) = \begin{cases} 0 & \text{if } d_p = d_q \\ t & \text{otherwise} \end{cases} \tag{4.10}$$

where t is a user defined penalty. The form of the function s described here is the Potts function but other functions for the smoothness function could be used.
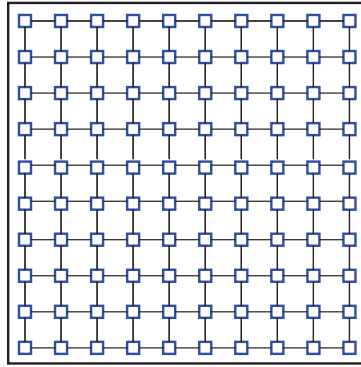
Figure 4.9: Four connected grid

Now the problem is posed: how to balance the data term and the smoothness term. One could think of smoothness term as modelling a four-connected grid as shown in figure 4.9, where each pixel has an edge connection with the immediate neighbours. This renders the problem of finding the minimum energy E(D) to be a NP-complete problem. The problem of global methods does not lie into the algorithms of energy minimization, but most likely into the problem of energy modelling. There are several optimisation algorithms that could be used:

Dynamic programming

Dynamic programming can be an efficient technique to compute the disparity map, frequently used for real-world applications with real-time constraints. The algorithm of dynamic programming on a tree (see figure 4.10) is just a generalization of dynamic programming on a linear array. First of all a root node r is chosen (can be randomly) in the tree. The optimal disparity for the root node r can be found using equation 4.11 [125].
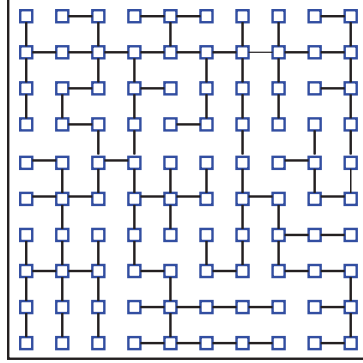
Figure 4.10: Tree example. If smoothness assumption is modeled as a tree instead of a four connected grid, the solution could be computed using dynamic programming

$$L(r) = min_{d_r \in D} \left(m(d_r) + \sum_{w \in C_r} E_w(d_r) \right) \tag{4.11}$$

where $m(d_r)$ is the data term and represents the cost of matching the pixel r at disparity d, C_r is the set of children of r, and $E_w(d_r)$ is the energy on a subset of the graph (see equation 4.12).

Equation 4.12 represents the energy of a subtree having the root at v and the parent at $p(v)$

$$E_v(d_{p(v)}) = min_{d_v \in D} \left(m(d_v) + s(d_v, d_{p(v)}) + \sum_{w \in C_v} E_w(d_v) \right) \tag{4.12}$$

where $s(d_v, d_{p(v)})$ is the smoothness penalty.

The problem is how to transform the four-connected grid (4.9) to a tree structure (for example as seen in figure 4.10). For this, several strategies could be employed.

Scanline Based Tree

One of the simplest way of transforming a four-connected grid to a tree is by deleting all the vertical edges. This has the advantage of being fast, but by doing this operation, we enforce just a horizontal smoothness assumption. Because the smoothness between neighbouring scanlines is

not enforced the disparity images will have *streaking* problems.
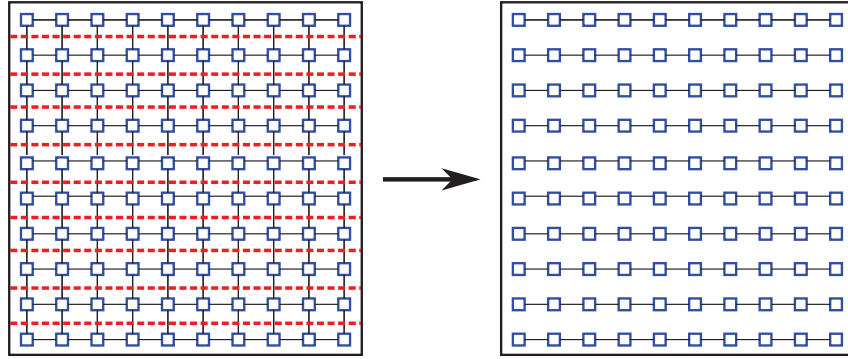
Figure 4.11: *From four-connected grid to tree:* Scanline based tree

Intensity Based Tree

In [125] a more efficient way of constructing the tree is proposed. For each edge in the four-connected grid, a weight $w(p,q)$ is computed (see equation 4.13). Based on this, a minimum spanning tree[6] is build. The advantage of this method is that the horizontal streaking are visibly reduced, but some vertical streaking might appear.

$$w(p,q) = |I(p) - I(q)| \tag{4.13}$$

where $I(p)$ is the intensity of pixel p.

Simple Tree Structures

Bleyer and Gelautz [20] proposed two simple tree structures as seen in figure 4.12. The two structures, horizontal and vertical tree, were designed to capture the texture otherwise missed by other techniques. The idea proposed by Bleyer and Gelautz [20] is to compute the optimal disparity for each point in the image by approximating the four-connected grid in each pixel using the two tree structured described. Streaking problem, that is inherent for most of the dynamic programming algorithms, is greatly reduced.

---

[6]A minimum spanning tree is a tree connecting all the nodes whose sum of weights is minimum among all such trees
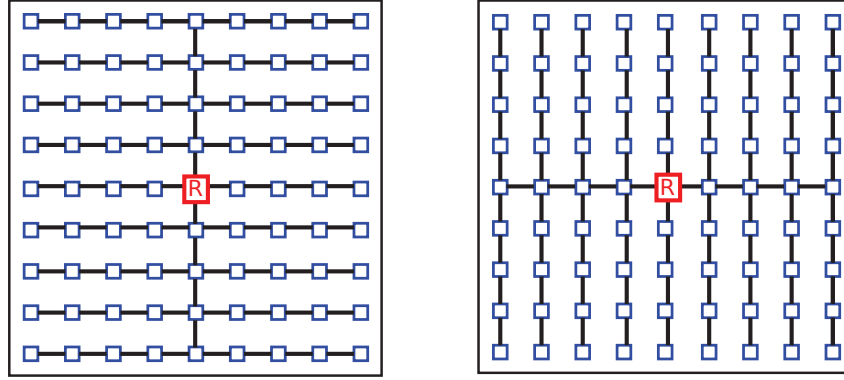
Figure 4.12: *Simple Tree structures:* Horizontal Tree and Vertical Tree

Belief Propagation

Sun et al. [119] has showed that an approximate solution for the energy minimization problem of stereo matching can be found using belief propagation. Belief Propagation is an energy minimization iterative algorithm that functions by passing messages within the directed-connected neighbouring pixels. Therefore the data cost term from the energy function is combined with four sets of message values corresponding to each possible disparity at each pixel. At each iteration an updated message value is sent to each four neighbouring pixels. After the iterations are completed, at each pixel the disparity value is estimated.

Due to the necessity of storing the data costs and message values for each possible disparity at each pixel the storage requirements are quite high. Moreover because it is an iterative process, it can be quite slow. This is why various methods of speeding up this algorithm have been developed.

One variant is hierarchical belief propagation [46]. A pyramid scheme is constructed in which the width and height are halved at each pyramid level. The message values of the lower levels are initialized by the the higher pyramid levels. Other speed ups of the algorithm are proposed by implementation on GPU [25],[61], [133]. Further speed up and reduction in the search space was proposed by Grauer-Gray and Kambhamettu [60].

Graph-Cuts

As described by Kolmogorov and Zabih [76], a graph cut is a partition of a graph with two distinguished terminals called source (s) and sink (t) into two sets V^s and V^t, such that $s \in V^s$ and $t \in V^t$. The cost of the cut is represented by the sum of the edges' weights between the two partitions. Finding the minimum cut (the cut of minimum costs among all possible cuts), and implicitly the minimum cost, can be resolved by computing a maximum flow between terminals.

An example of a minimum cut in a graph is shown in figure 4.13. In practice the global energy minimisation technique using graph cuts has been shown to be effective with the condition of having an appropriate cost function.
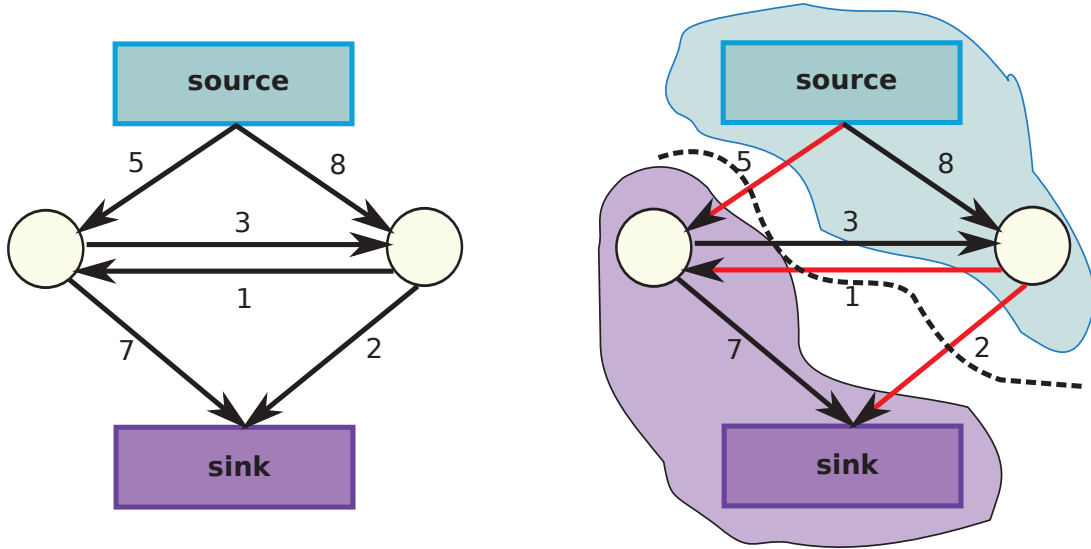
Figure 4.13: Example of a minimum cut in a graph. A cut is represented by all the edges that lead from the *source* set to the *sink* set (as seen in red edges). The sum of these edges represents the cost of the cut.

    Graph cuts can be applied for the algorithm of stereo matching by modelling the pixels in the image as nodes in the graph. In figure 4.14a is shown an example of such a graph: all the pixels in the image are represented as nodes and all the nodes on a given level belong to the same disparity. The edges starting directly from the source or going directly into sink are given an infinite cost. The vertical edges that can be viewed in figure 4.14a have as weight the cost of matching a pixel at a certain disparity. In this implementation graph-cuts will output the same result as a local matching method with winner-takes-all strategy. This is because the smoothness assumption was not explicitly modelled. In figure 4.14b a smoothness assumption between horizontal pixels is modelled, thus each horizontal edge will be given a weight that represents the smoothness penalty. The simplest way to define the smoothness penalty is to assign a user-defined weight w_p when two neighboured pixels have different disparities, and 0 otherwise.

    In practice, for the problem of stereo vision, the constructed graph is a three dimensional structure. If in figure 4.14b each layer represents just one scanline, in figure 4.15 each layer represents all the pixels in an image. The vertical edges represent the disparity edges, while all the horizontal edges represent the smoothness assumption.
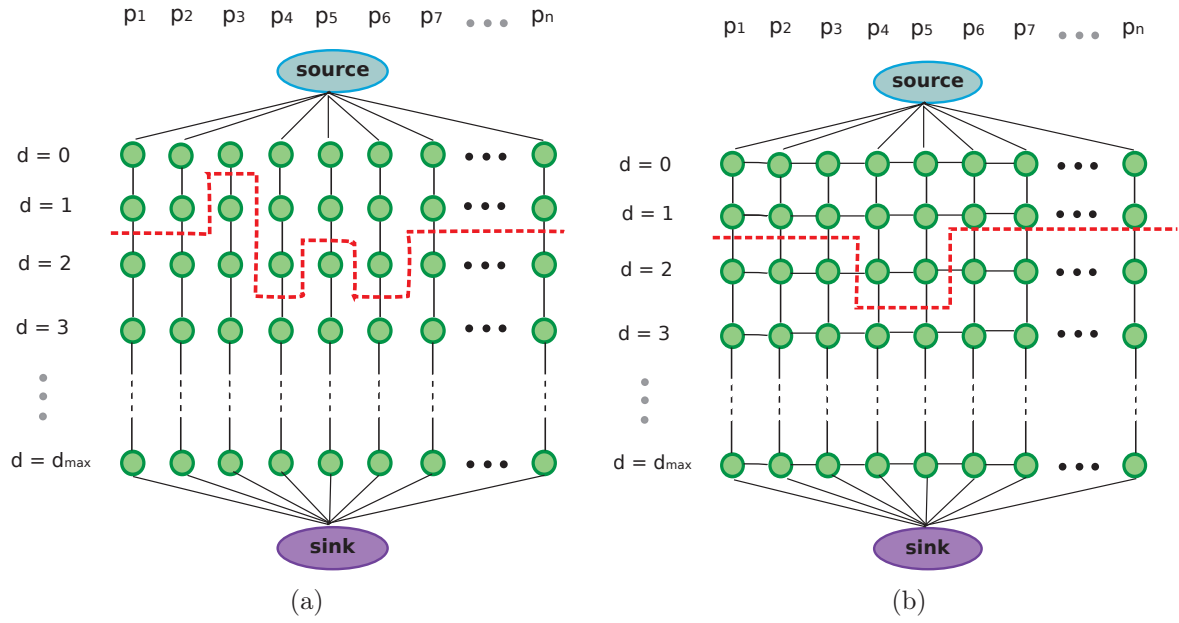
Figure 4.14: Graph cuts example on a scanline in stereo vision: a) without smoothness assumption; b) modelling smoothness assumption
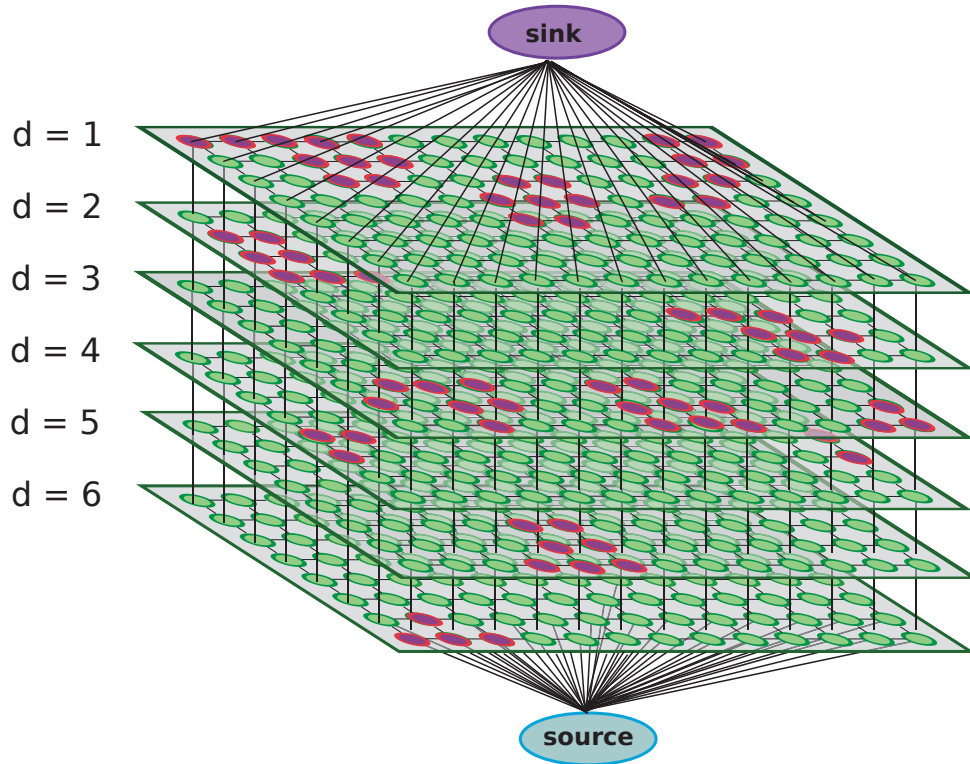
Figure 4.15: Graph Cuts applied to stereo vision algorithm.

4.2 Stereo Vision Datasets

There exist several challenging databases for testing the stereo matching algorithms (4.1), from simulated road scenes like *Van Synthetic stereo* [123] and EISATS [96], to real road scenes with

some degree of ground truth like KITTI [57], Make3D Stereo [111] or Ladicky[83]. Moreover one of the most well known benchmark for the stereo matching algorithms is the Middlebury[112] dataset.

The HCI/Bosch Challenge [95] contains some difficult situations for all the stereo matching algorithms like: reflections, flying snow, rain blur, rain flares or sun flares, thus giving an insight of where the algorithms might fail. Unfortunately, it does not come with a ground truth thus making difficult the evaluation of stereo matching algorithms. Nevertheless, it is an interesting dataset from the perspective of the challenging situations presented. The dataset contains 11 sequences, each with a particular challenging situation, with a total of 451 images.

Dataset	Number of Images	Ground truth	Scene	Image Type
KITTI [57]	389	YES (for 50% of px)	Road	Real
Middlebury[112]	38	YES (for 100% of px)	Indoors	Real
EISATS[96]	498	YES (for 100% of px)	Road	Synthetic
Make3D Stereo [111]	257	YES (for 0.5% of px)	Road	Real
Ladicky[83]	70	YES - manual labels	Road	Real
HCI/Bosch Challenge[95]	451	NO	Road	Real
Van Syntetic stereo[123]	325	YES (for 100% of px)	Road	Synthetic

Table 4.1: Datasets comparison for stereo matching evaluation

Datasets like Van Syntetic stereo [123] and EISATS [96] have the advantage of having ground truth for all the pixels, but they are composed of synthetic images. Other datasets containing real road images are Make3D Stereo [111] and Ladicky [83] but provide ground truth for a limited number of pixels.

One of the most popular datasets for comparison of stereo matching algorithms is the Middlebury dataset[112]. Although the dataset presents a lot of challenges from the perspective of different situations captured, the images are taken inside a laboratory in controlled conditions. In our experiments we have used this dataset for the validation of the stereo matching algorithms.

KITTI [57] dataset provides real road images with ground truth for around 50% of the pixels, thus making a good dataset for evaluating different stereo matching algorithms. The KITTI dataset contains 389 pairs of stereo images divided into 194 images for training and 195 for testing. The authors provide the ground truth only for the training sequences, while for the testing sequences an evaluation server should be used in order to have the results. The ground truth disparity map was obtained using a Velodyne laser scanner therefore for only about 50% of the pixels in the image the ground truth is available. The main challenges in the KITTI dataset are the radiometric distortions caused by sun flares, reflections and "burned" images (caused by

strong differences in intensity between light and shadow).

For our experiments we have chosen to work with the last two presented datasets: Middlebury, due to the considerable number of stereo matching algorithms that have been compared on these images, and KITTI, in view of our application context.

4.3 Cost functions

The matching cost function measures how *"good"* a correspondence is. It is important to make a difference between cost function, cost aggregation and the minimisation methods that use these costs. A typical classification of the matching costs is: parametric, non-parametric, and mutual information based costs [67].

4.3.1 Related work

To better understand these categories, they have to be explained in the context of radiometric distortions. Radiometrical similar pixels refer to those pixels that lie in different images, but in fact correspond to the same 3D scene point. Thus they should have similar or in a more ideal case the same intensity values in both images [65]. Radiometrical differences or distortions are therefore when corresponding pixels have in fact different intensities values. These are caused by: differences of camera parameters (aperture, sensor) that can induce different image noises and vignetting; surface properties like non-Lambertian surfaces[7]; difference in time of acquisition of the images (like is the case of some satellite imaging).

The parametric costs incorporate the magnitude of pixel intensity. Although usually simple to compute, the main disadvantage of the parametric costs is that they are often not robust to radiometric changes. The non-parametric costs incorporate just a local ordering of intensities, thus it is said that the latter are more reliable to radiometric distortions. The mutual information (MI) costs are computed on an initial disparity map. MI handles radiometric changes well [49] but it can only handle radiometric distortions that occur globally thus it has problems to local radiometric changes (which in practice are more common).

Choosing the right cost function is paramount for having a good disparity map. There exists several studies where comparison of cost functions is performed, the most extended ones being made in Hirschmuller and Scharstein [65], Hirschmuller and Scharstein [67]. In comparison with the study made in 2007, where six cost functions where tested, Hirschmuller and Scharstein [67] compared fifteen different stereo matching costs in relation with images affected by radiometric differences. These costs are compared using three different stereo matching algorithms: one

---

[7]Lambertian surfaces are the surfaces that reflect the light the same regardless of the observer's angle of view

based on global energy optimisation (Graph Cuts), one using semi-global matching [66] and a local window-based algorithm. They conclude that the cost based on CT gives the best overall performance.

In comparison with Hirschmuller and Scharstein [67] that use both simulated and real radiometric changes in a laboratory environment (Middlebury dataset [112]), we have chosen for the experiments to be performed on real road images from the KITTI dataset [57] which presents significant radiometric differences, as well as the well known Middlebury dataset. Besides the cost functions that provided the best results in Hirschmuller and Scharstein [67], we also test some recent functions based on CT that gave good results on the Middlebury dataset[8]. Moreover we propose two new cost functions: a fast function similar with the CT called Cross Comparison Census (CCC) and other function $C_{DiffCensus}$ that remains robust to radiometric changes.

4.3.2 State of the art of matching costs

In the following we present briefly existing cost functions. We divide them in parametric, non-parametric and mixed parametric costs. We call mixed parametric costs, those costs that try to enhance the discriminative power of a non-parameteric cost by incorporating extra information given usually by a parametric cost.

4.3.2.1 Parametric costs.

One of the most popular cost matching function is the *squared intensity differences (SD)* (see equation 4.14) like used by Kolmogorov and Zabih [76] or *absolute intensity differences (AD)* (see equation 4.15) which is typically combined with other information like used in Mei et al. [93], Klaus et al. [75]. SD and AD costs make the assumption of constant color therefore are sensitive to radiometric distortions.

Let p be a pixel in the left image with coordinates (x, y) and d the disparity value for which we want to compute the cost of p. Also $I_l(x, y)_i$ is the intensity value of pixel p in the left image on color channel i, while $I_r(x, y - d)_i$ is the intensity value of pixel given by coordinates $(x, y - d)$ in the right image. We consider n the number of color channels used ($n = 1$ for gray scale images and $n = 3$ for color images).

$$C_{SD}(x, y, d) = \frac{1}{n} \sum_{i=\overline{1,n}} (I_l(x, y)_i - I_r(x, y - d)_i)^2; \tag{4.14}$$

---

[8]http://vision.middlebury.edu/stereo/

$$C_{AD}(x, y, d) = \frac{1}{n} \sum_{i=\overline{1,n}} |I_l(x,y)_i - I_r(x, y - d)_i| \qquad (4.15)$$

If we consider $N(x, y)$ to be the neighbourhood of the pixel with coordinates (x, y), than the cost AD on this neighbourhood is defined like in equation 4.16. For the C_{SAD} the line between being a cost function or a cost aggregation technique is very fine.

$$C_{SAD}(x, y, d) = \sum_{(a,b) \in N(x,y)} C_{AD}(a, b, d) \qquad (4.16)$$

Filter based parametric costs include algorithms like *Laplacian of Gaussian* [78], *Mean*[6], *Bilateral background subtraction* [121] which apply a filter on the input images, after which the matching cost is computed with absolute difference. Other parametric costs that are computed inside a support window include *zero-mean sum of absolute differences(ZSAD), normalized cross-correlation (NCC)* and *zero-mean sum of normalized cross-correlation (ZNCC)*. The *ZSAD* subtracts the mean intensity of a support window from each intensity inside that window before computing the sum of absolute differences. *NCC* is a parameteric cost that can compensate for gain changes, while *ZNCC* is a variant that compensates both gain and offset within the correlation window [67]. Because *ZNCC* is a correlation function with values in $[0, 1]$, in order to obtain the cost we will subtract it from one (see equation 4.17).

$$C_{ZNCC}(x, y, d) = 1 - ZNCC(x, y, d) \qquad (4.17)$$

$$ZNCC(x, y, d) = \frac{\sum\limits_{(a,b) \in N_{(x,y)}} ZV(I_l, a, b) ZV(I_r, a, b - d)}{\sqrt{\sum\limits_{(a,b) \in N_{(x,y)}} (ZV(I_l, a, b))^2 \sum\limits_{(a,b) \in N_{(x,y)}} (ZV(I_r, a, b - d))^2}} \qquad (4.18)$$

$$ZV(I, x, y) = I(x, y) - \overline{I}_{N(x,y)}(x, y), \qquad (4.19)$$

where $\overline{I}_{N(x,y)}$ is the mean value computed in the neighbourhood $N(x, y)$.

In practice the parametric costs have proven to be less robust than the non-parametric ones [67], [7], with the exception of *ZNCC* [49],[120].

4.3.2.2 Non-parametric costs.

The most popular non-parametric costs include *Rank, Census* [136], and *Ordinal* [17], or pixelwise costs represented by *hierarchical mutual information* which were successfully applied by Sarkar and Bansal [110]. The costs based on gradient or non-parametric measures are more robust to

changes in camera gain and bias or non-lambertian surfaces while being less discriminative [75].

C_{CT}. As defined by Zabih and Woodfill [136] to compute the **C**ensus **T**ransform (CT) of a pixel p a window called the support neighbourhood ($n \times m$), must be centered on each pixel. Based on this, a bit-string is computed by converting the color values inside the window to value *one*, if the corresponding pixel has the value of the color greater than the center pixel's color value or *zero* otherwise. The local intensity relation is given by the equation 4.22, where p_1 and p_2 are pixels in the image. The census transform is given by equation 4.21, where $\otimes$ denotes a bitwise concatenation and $n \times m$ is the census window size. The CT cost is given by the Hamming distance (D_H) between the two bit strings (equation 4.20).

$$C_{CT}(x, y, d) = D_H(CT(x, y), CT(x, y - d)), \tag{4.20}$$

where CT is the bit string build like in eq. 4.21.

$$CT(u, v) = \otimes_{\substack{i=\overline{1,n} \\ j=\overline{1,m}}} (\xi(I(u, v), I(u + i, v + j))), \tag{4.21}$$

where $n \times m$ is the census support window, $\otimes$ denotes a bitwise concatenation, and ξ function is defined in eq. 4.22.

$$\xi(p_1, p_2) = \begin{cases} 1 & p_1 \le p_2 \\ 0 & p_1 > p_2 \end{cases} \tag{4.22}$$

CT can be computed on a dense (eq. 4.21) or sparse window (eq.4.23). In a sparse window [70], it is used only every second pixel and every second row as shown in figure 4.16. The filled blue pixels are the pixels used to compute CT.

$$CT_{Sparse}(u, v) = \otimes_{i=\overline{1:step:n}, j=\overline{1:step:m}} (\xi(I(u, v), I(u + i, v + j))) \tag{4.23}$$

where step is an empirical chosen value, usually *two*.

4.3.2.3 Mixed parametric costs.

Non-parametric costs are robust to radiometric distortions but they are less discriminative. That is why in recent works several combinations between parameteric and non-parameteric costs are proposed. In what follows we will present these functions. If the authors did not name the proposed cost functions we are going to use the first name on the article to name the cost.

C_{klaus}. One of the top three algorithms on the Middlebury dataset [75] proposes the function C_{klaus} (equation 4.24) that is a combination between C_{SAD} (equation 4.16) with a gradient based

(a) (b)
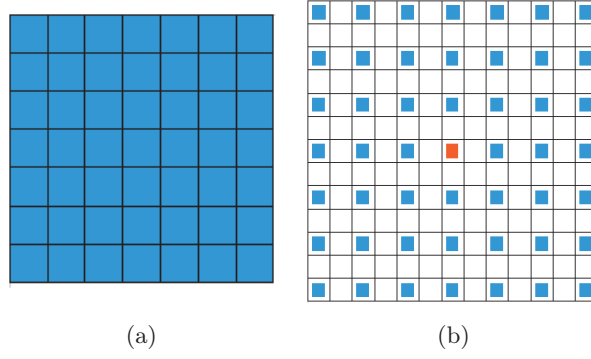
Figure 4.16: Census mask: a) Dense configuration of 7×7 pixels b) Sparse configuration for CT with window size of 13×13 pixels and *step 2*

.

measure C_{GRAD} (equation 4.25). The two costs are computed in a neighbourhood $N(x,y)$ of 3×3 pixels and are weighted by w.

$$C_{klaus}(x,y,d) = (1-w) * C_{SAD}(x,y,d) + w * C_{GRAD}(x,y,d) \tag{4.24}$$

where

$$C_{GRAD}(x,y,d) = \sum_{(a,b)\in N(x,y)} |\Delta_x I_l(a,b) - \Delta_x I_r(a,b-d)| + \\ \sum_{(a,b)\in N(x,y)} |\Delta_y I_l(a,b) - \Delta_y I_r(a,b-d)|, \tag{4.25}$$

where Δ_x and Δ_y are the horizontal and vertical gradients of the image.

Combinations based on CT became popular due to the good results obtained on the Middlebury dataset. For example one of the top algorithms on the Middlebury dataset[93], uses a combination between the C_{CT} and C_{AD} (eq. 4.26). The new cost, $C_{ADcensus}$, reduces the error in non-occluded areas, for the Middlebury dataset, in average with 1.3%.

$$C_{ADcensus}(x,y,d) = \rho(C_{CT}(x,y,d), \lambda_{census}) + \\ \rho(C_{AD}(x,y,d), \lambda_{AD}) \tag{4.26}$$

where λ_{census} and λ_{AD} control the influence of each cost, and ρ is defined in equation 4.27.

$$\rho(c,\lambda) = 1 - exp(-\frac{c}{\lambda}) \tag{4.27}$$

Another combination of a C_{CT} and C_{AD} (eq. 4.28), where both are computed on the gradient

images, is proposed by Stentoumis et al. [114]. It was shown that this new function, C_{cstent} (equation 4.28) can give up to 2.5% less erroneous pixels on Middlebury dataset.

$$
\begin{aligned}
C_{cstent}(x, y, d) = {} & \rho(C_{\Delta census}(x, y, d), \lambda_{census}) + \\
& \rho(C_{AD}(x, y, d), \lambda_{AD}) + \\
& \rho(C_{\Delta AD}(x, y, d), \lambda_{\Delta AD}),
\end{aligned}
\tag{4.28}
$$

where $\Delta census$ and ΔAD are the costs, CT and AD respectively, computed on gradient images.

4.3.3 Motivation: Radiometric distortions

For a stereo matching system to be functional in different conditions, it has to be robust to radiometrical differences. As previously stated, radiometrical similar pixels refers to those pixels that correspond to the same scene point and have similar or in an ideal case the same values in different images [65]. Radiometrical differences or distortions are therefore the situations where corresponding pixels have different values.
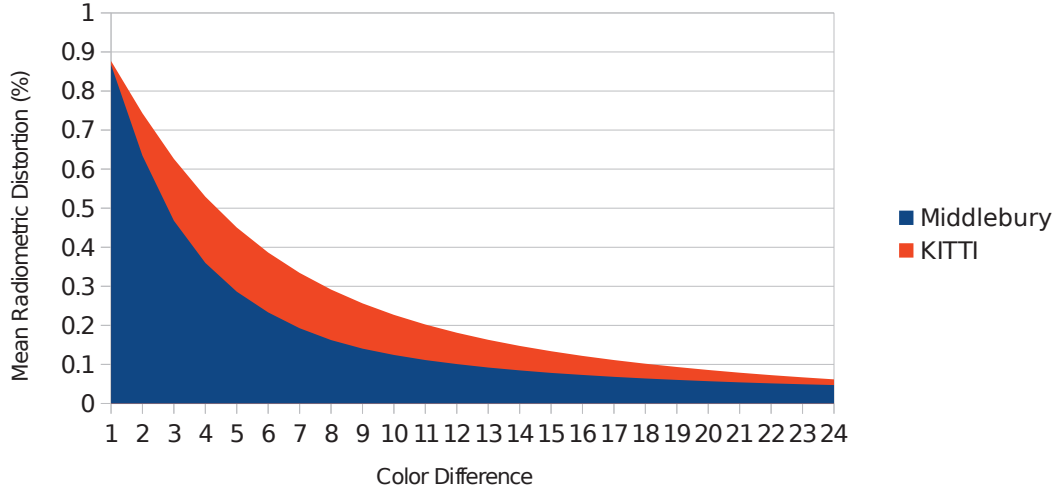
Figure 4.17: The mean percentage of radiometric distortions over the absolute color differences between corresponding pixels in KITTI, respectively Middlebury dataset .

In order to analyse the amount of radiometric distortions in different images, we have compared the dataset Middlebury and KITTI. In figure 4.17 is presented the mean percentage of radiometric distortions for the two datasets, over the absolute difference between corresponding pixels. As stated by Hirschmuller and Scharstein [65], the Middlebury dataset is taken inside a laboratory in controlled light conditions. Even so, for example at a color absolute difference of *five*, on the
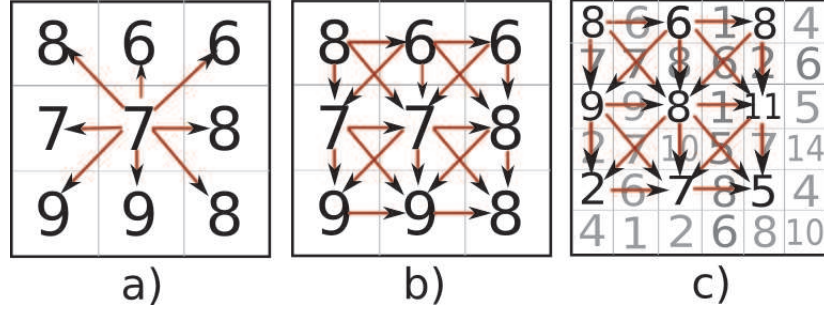
Figure 4.18: Bit string construction where the arrows show comparison direction for a) CT: '100001111', b) CCC: '00001111101111110100' in dense configuration, c) CCC in a sparse configuration

Middlebury dataset the average percentage of radiometric distortions is around 28%. On the other hand on KITTI dataset, where the images were collected outside, the average percentage of radiometric distortions at the same difference of color is larger than 45%. Therefore it is important to find a cost function that remains robust to radiometrical distortions.

4.3.4 Contributions

We have proposed two cost functions, one based on a modified CT that has the advantage of a small computational time while in the same time reducing the error, and the other one based on a combination between a CT-based cost and a mean sum of differences of intensities that will provide low errors in radiometrical affected regions.

4.3.4.1 Cross Comparison Census

We propose a new technique to compute the Census Transform bit string, that we named *Cross Comparison Census* (*CCC*). In comparison with *CT*, the bit string for *CCC* is obtained by comparing each pixel in the considered window with those in the immediate vicinity in a clockwise direction. For comparing the two bit-strings the Hamming distance is used like in the case of *CT*.

$$N(i, j, step) = \{(i, j + step); (i + step, j + step);$$
$$(i + step, j); (i + step, j - step)\}$$

(4.29)

where $(j + step) < m$ and $(i + step) < n$ and $(j - step) >= 0$

$$I_{CCCensus}(u, v) = \otimes_{i=\overline{0:step:n}, j=\overline{0:step:m}}(\xi(I(i, j), N(i, j, step)))$$

(4.30)

Figure 4.18.a shows the standard *CT*, while Figure 4.18.b and Figure 4.18.c show the *CCC*

principle in dense configuration and respectively in sparse configuration. The extra information that is captured in the CCC bit string will result in the possibility of using a smaller window size and fewer elements in the bit string while keeping all the robust results of the CT or even improving them.
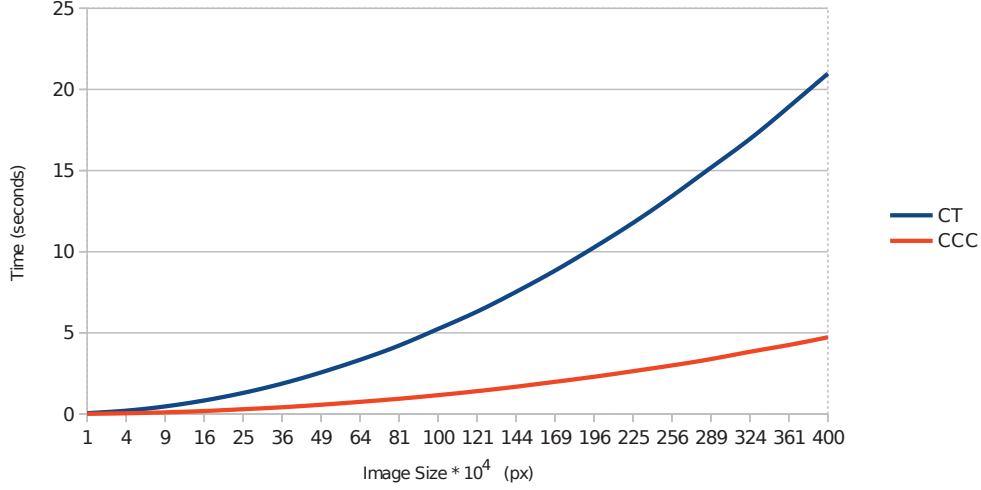
Figure 4.19: Computation time comparison between CT and CCC for different image sizes. In the figure an image size of $36 * 10^4$ corresponds to an image of 600×600 pixels. For both CT and CCC we used a window of 9×7 pixels, but CCC is computed using a step of two.

CCC can be computed in a very efficient way. First each pixel is compared with those in the immediate neighbourhood forming a mini bit string which is stored in a matrix. Secondly the final bit string of a given pixel is formed by the simple concatenation of the mini bit strings corresponding to the relevant pixels in the census window. These operations remove the redundant comparisons performed in the CT, making CCC very fast to compute. In the same time this method is friendly from a hardware perspective because it allows a greater degree of parallelism than CT. In figure 4.19 it is presented a comparison between computing time of CT and CCC in a single threaded configuration. It can be observed that when increasing the image size, defined as the total number of pixels in an image, the computation time for CT has a fast growing rate while for CCC the computation time increases with a lower rate. The same situation can be observed in the case of increasing the size of the neighbourhood window. In figure 4.20 we present comparison between computation time for CT and CCC when increasing the window size while keeping constant the image size.

4.3.4.2 DiffCensus

We propose a new function that combines the CT [136], or our proposed variant CCC, with the mean sum of relative differences of intensities inside a window (eq. 4.31). We consider CCC separately from CT due to its fast computation time. In comparison with functions like
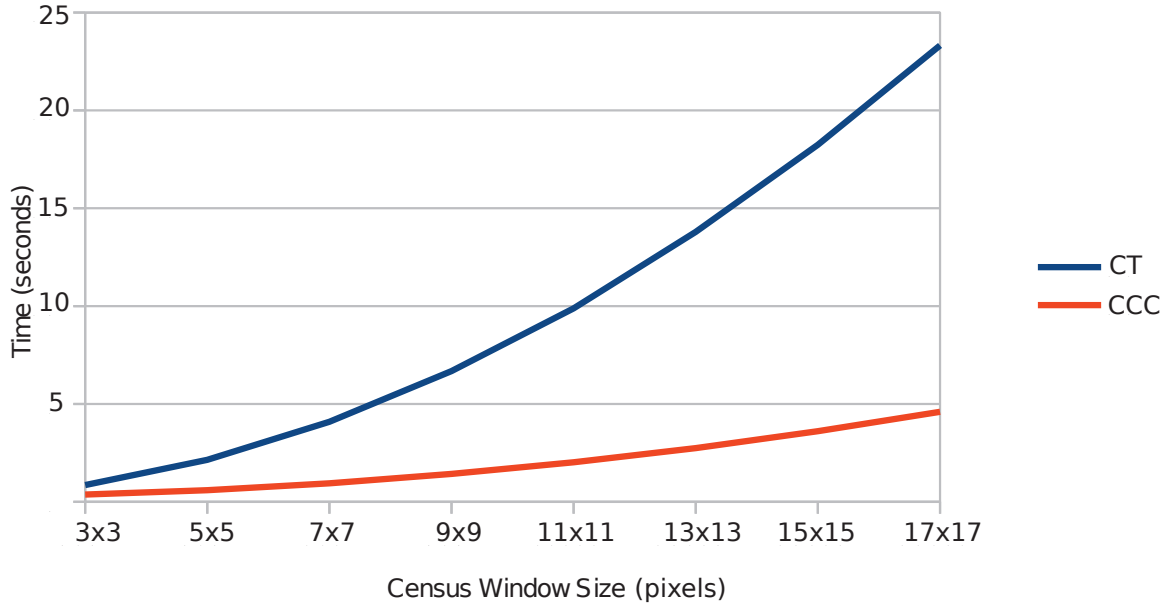
Figure 4.20: Computation time comparison between CT and CCC for different neighbourhood sizes for an image of 1000×1000 pixels.

$C_{ADCensus}$ or C_{cstent} that use the pixel intensities values, the $C_{DIFFCensus}$ does not rely on the value of the pixel intensity but on the difference of intensity between a considered pixel and its neighbourhood. This keeps the function as a non-parametric one while incorporating extra information.

$$
\begin{aligned}
C_{DIFFCensus}(x, y, d) = {} & \rho(C_{census}(x, y, d), \lambda_{census}) + \\
& \rho(C_{DIFF}(x, y, d), \lambda_{DIFF})
\end{aligned}
\tag{4.31}
$$

where C_{census} can be either C_{CT}, which will give C_{DIFFCT}, or C_{CCC}, which will give $C_{DIFFCCC}$; C_{DIFF} is defined in eq. 4.32.

$$
C_{DIFF}(x, y, d) = |\overline{DIFF_l}(x, y) - \overline{DIFF_r}(x, y - d)|
\tag{4.32}
$$

where $n \times m$ is the same support window that is used to compute the CT, and $DIFF_l$ is the $DIFF$ function applied to the left image, while $DIFF_r$ is the $DIFF$ function applied to the right image.

$$
\overline{DIFF}(u, v) = \frac{DIFF(u, v)}{CensusSize}
\tag{4.33}
$$

where $CensusSize$ is the size of the bit string given by the support window $n \times m$ and $step$ (eq. 4.29).

$$DIFF(u,v) = \sum_{\substack{i=\overline{1:step:n}\\ j=\overline{1:step:m}}} (|I(u,v) - I(u+i, v+j)|), \tag{4.34}$$

4.3.5 Algorithm

In order to test the proposed cost functions we use two different stereo matching algorithms: one based on graph cuts, and the other based on local cross aggregation.

4.3.5.1 Graph cuts

As described by Kolmogorov and Zabih [76], a graph cut is a partition of a graph with two distinguished terminals called source (s) and sink (t) into two sets V^s and V^t, such that $s \in V^s$ and $t \in V^t$. The cost of the cut is represented by the sum of the edges' weights between the two partitions. Finding the minimum cut, and implicitly the minimum cost, can be resolved by computing a maximum flow between terminals. In practice the global energy minimisation technique using graph cuts has been shown to be effective with the condition of having an appropriate cost function.

For the cost comparison, the energy function is used as described by Kolmogorov and Zabih [76]. The purpose is to find a disparity function f that minimizes a global energy $E(f)$ as seen in equation 4.35. The occlusion term E_{occ} imposes a penalty for occluded pixels, while E_{smooth} is the smoothness term which forces neighbouring pixels in the same image to have similar disparities. The data term $E_{data}(f)$ measures the cost of matching the function f.

$$E(f) = E_{data}(f) + E_{occ}(f) + E_{smooth}(f) \tag{4.35}$$

The data term used by Kolmogorov and Zabih [76] is defined as the cost of squared intensity differences (C_{SD}). For the following experiments, we will only modify the data term, while keeping E_{smooth} and E_{occ} as defined by Kolmogorov and Zabih [76].

4.3.5.2 Cross-Zones Aggregation & Histogram Voting

For the local technique of energy minimisation we chose to test a cross-based aggregation as described by Zhang et al. [137]. The algorithm consists in finding for each pixel a cross support zone. In the first step, a cross is constructed for each pixel. Given a pixel p, its directional arms (left, right, up or down) are found by applying the following rules:

- $D_c(p, p_a) < \tau$. The color difference (D_c) between the pixel p and an arm pixel p_a should be less than a given threshold τ. The color difference is defined as $D_c(p, p_a) = max_{i=\overline{1,n}}|I_i(p) - $

$I_i(p_a)|$, where $I_i(p)$ is the color intensity of the pixel p at channel i, and n are the number of color channels considered.

- $D_s(p, p_a) < L$, where D_s represents the euclidean distance between the pixels p and p_a and L is the maximum length threshold.

Each pixel in the image has a cost given by the considered cost functions. The cost values in the support region are summed up efficiently using integral images. To select the disparity, the minimum cost value is selected using a Winner-Take-All strategy. Then a local high-confidence voting scheme for each pixel is used as described by Lu et al. [90].

4.3.6 Experiments

4.3.6.1 Cost function Parameters

We have optimised each cost function by performing a grid search for the parameters on the first three images from the KITTI training dataset. For this, we have applied the algorithm of local stereo matching based on cross zone aggregation. Based on the obtained results, we have found the parameter values that minimize the error rate as follows:

- $\boldsymbol{C_{DiffCT}}$: $\lambda_{census} = 55$; $\lambda_{Diff} = 95$

- $\boldsymbol{C_{DiffCCC}}$: $\lambda_{census} = 55$; $\lambda_{Diff} = 95$

- $C_{ADcensus}$: $\lambda_{census} = 90$; $\lambda_{AD} = 90$

- C_{klaus}: $w = 0.2$

- C_{cstent}: $\lambda_{census} = 80$; $\lambda_{AD} = 35$; $\lambda_{\Delta AD} = 80$

Figure 4.21 shows the sensitivity of the cost function C_{DiffCT} for the three images, by varying the parameters λ_{census} and λ_{Diff}, in the interval $(0, 100]$. Darker values in the figure show smaller error rate. For the studied function the standard deviation of the error is of 0.52%. The optimised parameters were use throughout the experiments.

In what concerns the other parameters specific for the two stereo matching algorithms used, details are given in appendix B, tables B.1 and B.2.

In what follows, we use the KITTI stereo images for all the numerical experiments. KITTI dataset is divided into 194 images in the training set for which the ground truth images is provided, and 195 images in the testing set for which an evaluation server should be used in order to obtain the results. The following experiments are performed only on the 194 images in the training set[9]

---

[9]At the moment of performing the tests, only one submission in 72 hours was allowed on the evaluation server. Thus having an important number of situations to be tested, we have opted to use just the training set.
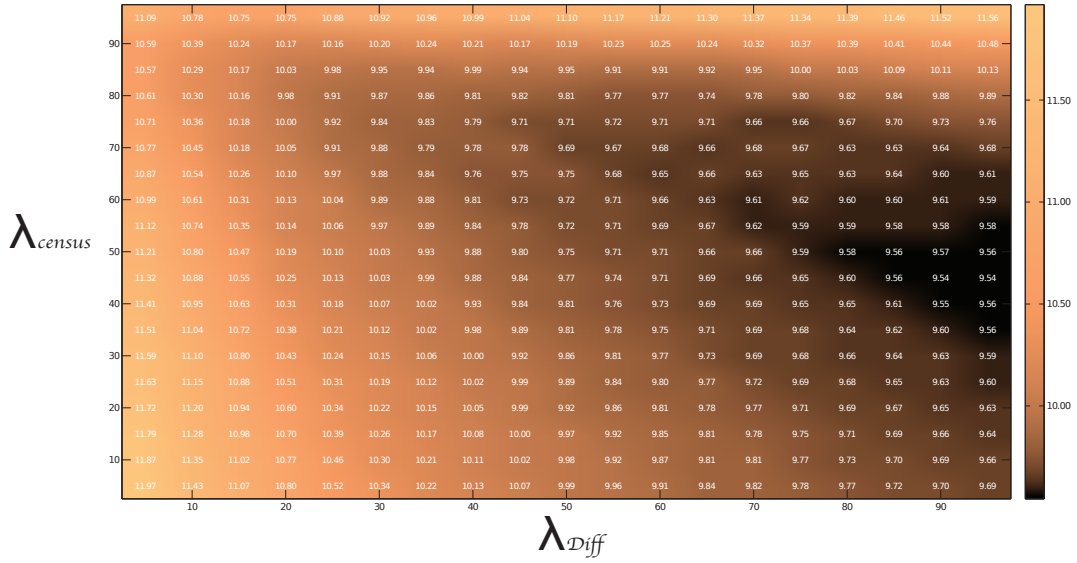
Figure 4.21: Cost function (C_{DiffCT}) sensitivity to different parameters values

All the cost functions in this section are evaluated by the average percentage of erroneous pixels in all zones, occlusions included, and computed at 3 pixels error threshold.

4.3.6.2 Discriminative power of cost functions

In order to quantify how pertinent the information given by each cost function is, we have compared all the cost functions in relation to all the possible disparities. This is the equivalent of computing the error rate of stereo matching using only these functions without any cost aggregation technique. Because some of the cost functions are defined in a neighbourhood, thus having an advantage in report with the others, we also compute the error given by each function when using a fixed aggregation window. The results for an error threshold of three pixels are presented in table 4.2.

Table 4.2: Error percentage of stereo matching with no aggregation (NoAggr) and window aggregation (WAggr).

Function	C_{AD}	C_{SD}	C_{CT}	C_{ADCT}	C_{CCC}	C_{ADCCC}	C_{cstent}	C_{klaus}	C_{ZNCC}	$C_{DiffCCC}$	C_{DiffCT}
Error NoAggr	85.8%	86.22%	71.9%	74.5%	62.3%	71.6%	68.05%	57.52%	**39.97%**	58.96%	66.51%
Error WAggr	42.20%	43.56%	26.92%	23.49%	26.51%	23.49%	27.29%	31.28%	28.68%	22.36%	**21.60**%

For the cost functions we compare C_{AD}, C_{SD}, C_{CT} with a support window of 7×9 pixels (bit string of 63 elements), C_{CCC} with a support window of 7×9 pixels and a step of 2 (bit string of 55 elements), C_{ADCT} and C_{ADCCC}, C_{cstent}, C_{klaus}, C_{ZNCC}, $C_{DiffCCC}$ and C_{DiffCT}.

For the results obtained with an aggregation window we have used one of 9×7 pixels. With no aggregation and winner takes it all strategy, the most discriminative function is the cost given by the $ZNCC$ with an error of 39.97%, followed by C_{klaus} with 57.52%. From the census based functions, $C_{DiffCCC}$ provides the best results with an error of 58.96% followed by C_{CCC} with 62.3%. The combination of AD with either CT or CCC, overall increases the error rate at 71.9% and 71.6% respectively. Therefore from a discriminative point of view, C_{ZNCC}, C_{klaus} and C_{CCC} are the most competitive.

For the results obtained using a window aggregation and winner takes it all strategy, the proposed function based on mean sum of relative differences provides the best results: C_{DiffCT} with 21.60%, followed by $C_{DiffCCC}$ with 22.36%. These are followed by the functions based on $ADCensus$: C_{ADCT} and C_{ADCCC} both with 23.49%.

4.3.6.3   Results with graph cuts stereo matching

The graph cuts minimisation algorithm was used as described by Kolmogorov and Zabih [76] and section 4.3.5.1. Graph cuts minimisation is an iterative process, with the error decreasing when increasing the number of iterations. One iteration takes around six minutes[10] to complete for an image of size 1241×376 pixels. We have started the experiments using *six* iterations but we did not observed any significant improvement over using just one iteration, while the running time was considerably increased. Therefore all the experiments presented in this section were carried out with one iteration.

In order to show the importance of the data term for the energy function, we have tested the nine cost functions presented in section 4.3.2: C_{AD}, C_{Census}, $C_{CCCensus}$, C_{klaus}, $C_{ADcensus}$, C_{cstent}, C_{ZNCC}, $C_{DIFFCCC}$ and C_{DIFFCT}. This functions were used without an aggregation window with the except of C_{klaus} where a neighbourhood of 3×3 pixels is required by the algorithm and C_{ZNCC} where, for the same reasons, a neighbourhood of 9×7 pixels was used.

Figure 4.22 presents the mean error rate on all the 194 images from the training KITTI dataset. The error with C_{SD} is quite large, while with the other cost functions the error decreases significantly. The best overall performance is given by the proposed $C_{DiffCCC}$ function with an error of 12.26%, followed by C_{DiffCT} with 12.97% and very closely by C_{ZNCC} with 12.98%. In terms of computing time the C_{ZNCC} is the slowest function taking in average ten times longer to compute in comparison with the other two functions.
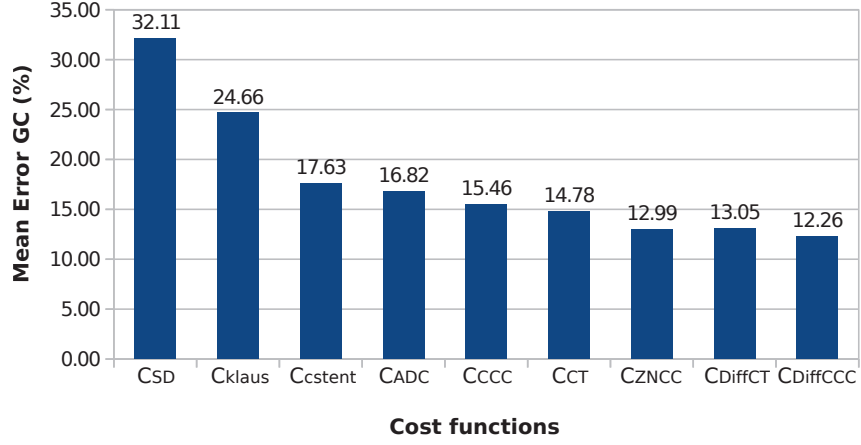
Figure 4.22: Mean error for each cost function using **graph cuts** stereo matching.
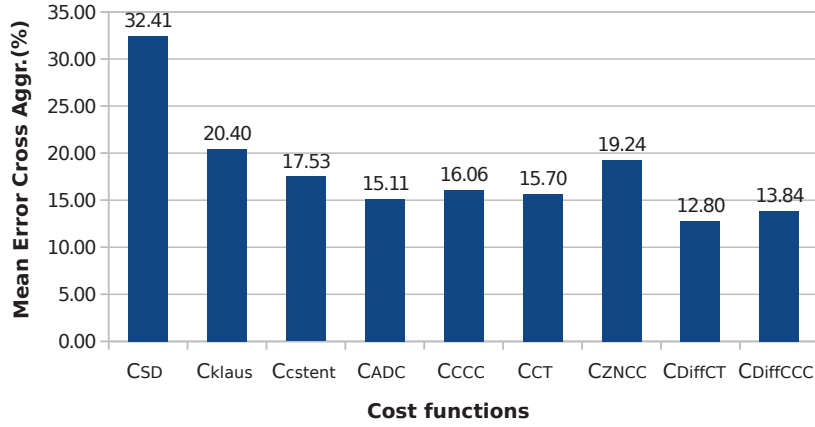
Figure 4.23: Mean error for each cost function using **local cross aggregation** stereo matching.

4.3.6.4 Local energy optimisation based on cross zone aggregation

Without a real time constraint, the global energy optimisation technique can give very accurate disparity maps. In comparison, local techniques could achieve real time running with some trade-off concerning the quality of the disparity map. We have chosen to compare with the global energy optimisation based on graph cuts a local optimisation based on cross zone aggregation and local high confidence voting [137] due to the promising results obtained on the Middlebury [112] dataset.

The same cost functions tested with the graph cuts were evaluated with the local energy optimisation. The color threshold for cross zone construction used is $\tau = 20$, as chosen by Zhang et al. [137]. For the maximum arm length two different thresholds were used, vertical arm $L_{vertical} = 10$ and horizontal arm $L_{horiz} = 17$, due to an observed predilection in the considered dataset of objects to have the same disparity in horizontal. The results obtained on the KITTI dataset are presented in figure 4.23.

---

[10]Our tests were performed on a computer with Dual Core 2.4 GHz single threaded

The overall results are better than those obtained with the graph cuts method (tested in a reasonable running time situation). When comparing the functions, the best results are obtained by our proposed functions based on sum of differences: $C_{DiffCCC}$ and C_{DiffCT}. C_{DiffCT}, with a 12.8% error rate, gives better results than the $C_{DiffCCC}$, with a 14.07% error rate, but the latter has a smaller running time of around 40%. The $DIFF$ based functions are followed as results by the $C_{ADCensus}$ and standard C_{CT} based cost functions.

4.3.7 Discussion

Even though the tested cost functions show different discriminative power, as seen in subsection 4.3.6.2 where C_{CCC} has proven to be the most discriminative, a cost aggregation or cost minimisation algorithm can change the ranking. For each minimisation method must be chosen a specific cost function. In figure 4.25 a visualisation of the output disparity map for each function in combination with the two stereo algorithms is shown. Columns one and three show the results obtained using the local stereo matching based on cross zone aggregation, while columns two and four the results obtained with graph cuts. The output results for two images is presented. While for the first image, results in columns one and two, a satisfactory disparity map is obtained with both stereo matching algorithms, the second image presented is more challenging due to large regions without texture. For a better visualisation of the disparity map results, we refer the reader to appendix C.

For the graph cuts algorithm the proposed $C_{DiffCCC}$ function provided the best results with very smooth disparity results in the road region but still erroneousness pixels could be found in textureless areas.

The local stereo matching algorithm gives comparable results with those of graph cuts at a much lower time cost. In this situation the best results are given by our proposed function C_{DiffCT}. The disparity map is not as smooth as in the case of the graph cuts algorithm because we did not used any method of post-filtering. The main problems of the local minimisation technique based on cross-aggregation lies in big regions of similar color. The assumption when using an aggregation area is that in the considered region all the pixels have the same disparity. In practice large areas of same or similar color will not have the same disparity (for example road region and slanted walls).

Concerning the sensitivity of the cost functions in the presence of radiometric distortions, distortions quantified as absolute color difference of corresponding pixels, a comparison of different cost functions is performed (see figure 4.24). For this, at each level of radiometric distortion, for all the 194 images from the training set, the error of the pixels belonging to that level was

measured. As it can be observed from the figure the proposed cost functions, $C_{DiffCCC}$ and C_{DiffCT}, give the lowest error rate even in the presence of radiometric distortions.

In what concerns the function behaviour in texture less areas, due to the nature of the function, it will not improve the results in these regions no more than the other cost function will. For instance, in a white wall region all the cost functions will not, in general, be able to provide discriminative values. Therefore it seems that, in texture less areas, the problem does not lay in the cost function, rather than in the aggregation area or the energy minimisation algorithm used.
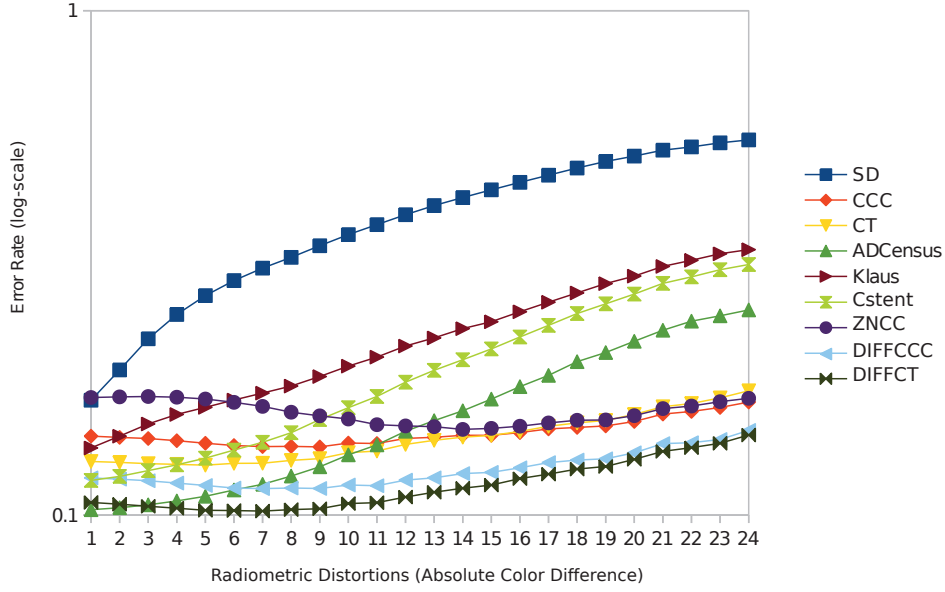
Figure 4.24: Output error (logarithmic-scale) for different cost functions in presence of radiometric distortions

4.4 Choosing the right color space

In the process of stereo matching using grayscale images, ambiguity could arise in situation where objects of different colors, for example red and green, produce pixels of similar intensities. Thus intuitively, color should contribute for stereo matching due to the fact that it provides additional information in comparison with grayscale.

4.4.1 Related work

There exist a few surveys that study the impact of color information in the stereo matching algorithms. Some studies show that the use of color leads a major improvement by reducing the error rate like shown in Chambon and Crouzil [28], Okutomi et al. [101], Mühlmann et al. [97] or Bleyer et al. [21], others by contrary Hirschmuller and Scharstein [67] report that color

a1) Visible left image *0*   **b1)** Ground truth image *0*   **c1)** Visible left image *2*   **d1)** Groud truth image *2*

a2)CZA: C_{SD}: 19.36%   **b2)**GC: C_{SD}: 24.501%   **c2)**CZA: C_{SD}: 51.22%   **d2)**GC: C_{SD}: 55.25%

a3)CZA: C_{CCC}: 11.55%   **b3)**GC: C_{CCC}: 5.27%   **c3)**CZA: C_{CCC}: 14.24%   **d3)**GC: C_{CCC}: 17.78%

a4)CZA: C_{CT}: 12.50%   **b4)**GC: C_{CT}: 5.83%   **c4)**CZA: C_{CT}: 12.82%   **d4)**GC: C_{CT}: 15.31%

a5)CZA: $C_{ADCensus}$: 8.81% **b5)**GC: $C_{ADCensus}$: 9.20% **c5)**CZA:$C_{ADCensus}$: 11.27%**d5)**GC: $C_{ADCensus}$: 16.20%

a6)CZA: C_{klaus}: 11.99%   **b6)**GC: C_{klaus}: 22.09%   **c6)**CZA: C_{klaus}: 14.96%   **d6)**GC: C_{klaus}: 34.82%

a7)CZA: $C_{DiffCCC}$: 8.65% **b7)**GC: $C_{DiffCCC}$: 7.22% **c7)**CZA: $C_{DiffCCC}$: 13.08%**d7)**GC: $C_{DiffCCC}$: 15.04%

a8)CZA: C_{DiffCT}: 7.89%   **b8)**GC: C_{DiffCT}: 8.05%   **c8)**CZA: C_{DiffCT}: 11.56%   **d8)**GC: C_{DiffCT}: 14.22%

a9)CZA: C_{cstent}: 9.08%   **b9)**GC: C_{cstent}: 14.92%   **c9)**CZA: C_{cstent}: 15.27%   **d9)**GC: C_{cstent}: 15.53%

a10)CZA: C_{ZNCC}: 9.45%   **b10)**GC: C_{ZNCC}: 5.88%   **c10)**CZA: C_{ZNCC}: 20.21%   **d10)**GC: C_{ZNCC}: 13.18%

Figure 4.25: Comparison between cost functions. On first row there are presented two left visible images (**a1** and **c1**) from the KITTI dataset with the corresponding ground truth disparity images (**b1** and **d1**). On the following lines are the output disparity maps corresponding to different functions: on the first (a2-a10) and third column (b2-b10) the output obtained with the cross zone aggregation (CZA) algorithm, while on columns two (b2-b10) and fourth (d2-d10) the output of the graph cuts algorithm. Images a2-a10 and b2-b10 correspond to the disparity map computed for image a1 while the images c2-c10 and d2-d10 correspond to the disparity map computed for image c1.

does not help, especially when using in combination with radiometric insensitive cost functions. Bleyer and Chambon [19] reports that color has consistently led to performance degradation, particularly with radiometric insensitive cost functions. Also in [19] there is shown the particular inefficiency of color stereo matching when the output images from the stereo system present some color discrepancies.

In the field of autonomous vehicles some stereo matching algorithms using color exist. For instance Cabani et al. [26] explored color gradient to detect edges in the stereo image pair. The stereo matching is carried out by computing the photometric distance between the feature point with its neighbour. This approach remains, however, sensitive to any lighting condition variations due to a fixed camera gain. In comparison with Cabani et al. [26] and Bleyer and Chambon [19], we will combine different color spaces with several stereo matching cost functions using different stereo matching algorithms.

A color space is an mathematical model that describes different ways in which the *colors* can be represented. When acquiring color images, because of the natural outdoors lighting conditions, the same object may have important discrepancies of color intensities in the stereo image pair. This makes hard the stereo matching task and hence the disparity computation. In order to choose an appropriate color space, we will evaluate the error given by the disparity map obtained using eight different color spaces: RGB, XYZ, LUV, LAB, HLS, YCrCb, HSV and the gray scale space, as presented in table 4.4.

4.4.2 Experiments

In order to compare different color spaces, we have chosen as database the Middleburry dataset. It is the only dataset that provides color stereo images along with ground truth values. Performance of different color spaces can be influenced by the cost function used and also the stereo matching algorithm. For example the local stereo matching based on *cross zones aggregation* uses color thresholds to construct the aggregation region.

For tests we have compared nine different algorithms. In table 4.3 is presented the mean error rate for each color space and for each cost function across all the algorithms. Results for individual algorithms across different color spaces and different cost functions are presented in appendix A.

Name	Comments
XYZ	$$\begin{bmatrix} X \\ Y \\ Z \end{bmatrix} = \tfrac{1}{0.17697} \begin{bmatrix} 0.49 & 0.31 & 0.20 \\ 0.17697 & 0.81240 & 0.01063 \\ 0 & 0.01 & 0.99 \end{bmatrix} \begin{bmatrix} R \\ G \\ B \end{bmatrix}$$
LUV	$$L^* = \begin{cases} (\tfrac{29}{3})^3 Y/Y_n, & Y/Yn \le (\tfrac{6}{29})^3 \\ 116(Y/Y_n)^{\frac{1}{3}} - 16 & Y/Yn > (\tfrac{6}{29})^3 \end{cases}$$ where Y_n is point luminance $$u = 13L*(u'-u'_n), v = 13L*(v'-v'_n)$$ where $u' = \frac{4X}{X+15Y+3Z}, v' = \frac{9Y}{X+15Y+3Z}$
LAB	$$L = 116f(Y/Y_n) - 16$$ $$a = 500[f(X/X_n) - f(Y/Y_n)]$$ $$b = 200[f(Y/Y_n) - f(Z/Z_n)]$$ $$where f(t) = \begin{cases} t^{\frac{1}{3}} & \text{if } t > (\tfrac{6}{29})^3 \\ \tfrac{1}{3}(\tfrac{29}{6})^3 + \tfrac{4}{29} & \text{otherwise} \end{cases}$$
HLS	$$C = max(R,G,B) - min(R,G,B)$$ $$H' = \begin{cases} 0 & \text{if C=0} \\ \frac{G-B}{C} mod 6 & \text{if M=R} \\ \frac{B-R}{C} + 2 & \text{if M=G} \\ \frac{R-G}{C} + 4 & \text{if M=B} \end{cases}, H = 60°H'$$ $$L = \tfrac{1}{2}(M+m)$$ $$S = \begin{cases} 0 & \text{if C=0} \\ \frac{C}{1-|2L-1|} & \text{otherwise} \end{cases}$$
YCrCb	$$\begin{bmatrix} Y \\ C \\ C \end{bmatrix} = \begin{bmatrix} 1/3 & 1/3 & 1/3 \\ 1 & -1/2 & -1/2 \\ 0 & -\sqrt{3}/2 & \sqrt{3}/2 \end{bmatrix} \begin{bmatrix} R \\ G \\ B \end{bmatrix}$$
HSV	H - similar to H component from HLS $$V = max(R,G,B)$$ $$S = \begin{cases} 0 & \text{if C=0} \\ \frac{C}{V} & \text{otherwise} \end{cases}$$
Gray	I = 0.3*R+0.59*G+0.11*B

Table 4.4: Color Spaces used for comparison

	RGB	XYZ	LUV	LAB	HLS	YCrCb	HSV	GRAY
C_{SD}	26.19	27.09	**25.94**	26.09	37.28	25.56	37.10	30.51
C_{AD}	**24.40**	24.54	25.15	25.36	31.93	24.89	30.82	29.57
C_{CCC}	15.81	**14.37**	21.73	19.87	34.62	21.66	38.93	15.69
C_{CT}	18.12	**16.81**	23.89	21.88	35.63	23.26	39.51	18.20
C_{ADCT}	16.28	**15.40**	20.09	18.79	27.97	19.53	28.74	16.54
C_{ADCCC}	15.01	**14.13**	19.14	17.83	27.71	18.84	28.49	15.18
C_{DIFFCT}	16.31	**15.17**	20.48	19.03	30.57	20.20	32.10	15.41
$C_{DIFFCCC}$	17.60	**16.40**	21.05	19.98	30.45	20.84	31.22	16.74

Table 4.3: Average error

4.4.3 Discussion

As shown in table 4.3, the color space that consistently provided slightly better results is the *XYZ*. Between *RGB* and *GRAY* the difference is quite negligible, with the exception of the *SD* cost for which the improvement was of 4.3% and *AD* cost for which the the improvement was of 5.2%. Therefore we back up the claims made by Bleyer and Chambon [19]: in the context of radiometric insensitive the cost functions the color does not bring an improvement. Nevertheless it doesn't degenerate the performance. Moreover, the costs that incorporate some kind of color information like ADCCC, ADCT, DIFFCT, DIFFCCC, provided better results that the classical census transform (CT).

We have only tested the performance of different color spaces for stereo matching on the Middlebury dataset, where images were acquired with the same type of cameras. Further tests should include color images taken in different conditions with a variety of cameras in order to insure a diversity that will make the findings statistical relevant.

4.5 Conclusion

In this chapter we have proposed several cost functions robust to radiometric distortions. These were compared against other state of the art function using two different stereo matching algorithms: a global method based on graph cuts and a local method based on cross zone aggregation with high confidence voting.

Experiments show that on KITTI dataset the results of local methods are comparable with those of global methods. In addition local methods have a high computing speed. From the tested functions, the proposed function gives the smallest error rate and has proven to be more robust to radiometric distortions. Consequently, in the context of real time constraint of the intelligent vehicle application, our choice as a stereo matching algorithm is for the local method in combination with a cost function based on $DIFF$ ($C_{DiffCT}, C_{DiffCCC}$).

KITTI dataset for stereovision contains only grayscale information, but color could provide further discriminative information about the scene, as shown by the experiments performed Middlebury dataset. Therefore, as future work it would be interesting to test the functions on color road stereo images.

In the next chapter we are going to study the performance of a multi-modal classifier, Intensity, Disparity and even Motion, for the task of pedestrian classification. As stereo matching algorithm for the experiments performed in the next chapter we chose the local stereo matching algorithm based on cross zone aggregation with high confidence voting and the cost function C_{DiffCT} .

<div style="text-align: right;">*5*</div>

Multi-modality Pedestrian Classification in Visible and FIR

Contents

In the field of pedestrian classification and detection, the main focus was on using the intensity/color information from the Visible domain. This is proven by the large number of existing datasets and features developed specifically for the visible domain. Nevertheless, pedestrian classification in particular, and object classification in general, is still a challenging problem for computers, whereas for the human perception is a rather easy task. Humans do not use just the intensity information from the scene, rather employ also cues like *depth* and *motion*.

In this chapter we study the performance of different features computed on modalities like depth and motion, in comparison with the intensity information from Visible domain, along with different fusion strategies. Moreover, we extend the analysis to the intensity information from Far Infrared domain.

5.1 Related work

A new direction of research for pedestrian classification and detection is represented by the combination of different features and modalities, extracted from Visible Domain, such as intensity, motion information from optical flow and depth information given by the disparity map.

Visible Domain.

Most of the existing research is using depth and motion just for hypothesis generation, by constructing a model of the scene geometry. For example, Bajracharya et al. [5] use stereovision in order to segment the image into regions of interest, followed by the use of geometric features computed from a 3D point cloud. Enzweiler et al. [38] use motion information in order to extract region of interest in the image, followed by shape based detection and texture based classification. Ess et al. [43] integrate stereo depth cues, ground-plane estimation, and appearance-based object detection. Gavrila and Munder [55] use (sparse) stereo-based ROI generation, shape-based detection, texture-based classification and (dense) stereo-based verification. Nedevschi et al. [99] propose a method for object detection and pedestrian hypothesis generation based on 3D information, and use a motion-validation method to eliminate false positives among walking pedestrians.

Rather than just using depth and motion as cues for the hypothesis generation, a few research works began integrating features extracted from these modalities directly into the classification algorithm. For example, Dalal et al. [31] proposed the use of histogram of oriented flow (HOF) in combination with the well known HOG for human classification. Rohrbach et al. [109] propose a high level fusion of depth and intensity utilizing not only the depth information in the pre-processing step, but extracting discriminative spatial features (gradient orientation histograms and local receptive fields) directly from (dense) depth and intensity images. Both modalities are represented in terms of individual feature spaces. Wojek et al. [132] incorporates motion estimation, using HOG, HAAR and Oriented Histograms of Flow. Walk et al. [127] proposed a combination of HOF and HOG, along with other intensity based features, with very good results on a challenging monocular dataset: Caltech[36]. Walk et al. [128] proposed the combination of HOG, HOF, and a HOG-like descriptor applied on the disparity field (HOS), along with a proposed Disparity statistics (DispStat) feature. Most of these articles have used just one feature applied on different modalities and they lack an analysis of the performance of different features computed from a given modality.

Enzweiler et al. [41], [40] proposed a new dataset for pedestrian classification and combine different modalities, eg. intensity, shape, depth and motion, extracting HOG, LBP and Chamfer distance features. Moreover they propose a mixture-of-expert framework in order to integrate all

these features.

FIR domain.

In addition of multi-modality fusion in the Visible domain, several studies use Stereovision in the Far-Infrared domain. For example, Krotosky and Trivedi [81] use a four-camera system (two visible cameras and two infrared) and compute two dense disparity maps: one in visible and one in infrared. They use the information from the disparity map through the computation of v-disparity [82] in order to detect obstacles and generate pedestrian hypothesis. This work is extended in [80], where HOG-like features are computed on Visible, Infrared and Disparity map and then fused. Unfortunately, the tests performed by Krotosky and Trivedi [81],[80] were on a relative small dataset where no other obstacles beside the pedestrians were present.

Bertozzi et al. [14],[11] proposed a system for pedestrian detection in stereo infrared images based on warm area detection, edge based detection and v-disparity computation. Stereo information is used just to refine the hypothesis generated and compute the distance and size of detected objects, but it is not used in the classification process.

5.2 Overview and contributions

In comparison with Enzweiler and Gavrila [40] we extend the analysis of the impact of different modalities (Intensity, Depth and Motion) in combination with different features, along with several fusion strategies: between same features but different modalities, different features same modality, different features different modalities, of "best features" fusion for each modality. All these results are presented in section 5.5.

Moreover, in section 5.7, we extend the same feature analysis, but this time comparing the modalities: Far-Infrared, Intensity, Depth and Motion. In addition, we present some insights into the impact of different stereo vision algorithms for the classification task.

5.3 Datasets

There exists several datasets that are publicly available and commonly used for pedestrian classification and detection in the visible domain. Table 5.1 presents an overview of existing datasets in the Visible Domain.

Visible Domain.

INRIA [30] is a well established dataset, but in comparison with newer datasets, it has a relative small number of people. NICTA dataset [105] consists mostly of images taken with a digital camera having as training and testing set cropped BB containing people.

Dataset	Properties					Training		Testing	
	Acquisition Setup	Environment	Colour	Occlusion Label	Stereo	No. Img.	No. Ped.	No. Img.	No. Ped.
Caltech [36]	Mobile	Road Scene	Yes	Yes[a]	No	128 k	192k	155k	121k
Daimler Monocular [39]	Mobile	Road Scene	No	No	No	-	15 560	56.492	21 790
Daimler Multi-Cue [41]	Mobile[b]	Road Scene	No	Yes[c]	Yes	-	52k	11k	-
ETH [43]	Mobile	Sidewalk	Yes	No	Yes	490	1 578	12k	2 293
INRIA [30]	Photos	-	Yes	No	No	-	1 208	566	-
KITTI [57]	Mobile	Road Scene	Yes	Yes	Yes	7481	4487	Online Evaluation	7518
NICTA [105]	Photos	Road Scene	Yes	Yes	Yes	-	18.7k	6.9k	-
TUD-Brussels [132]	Mobile	Road Scene	Yes	No	No	1 284	1 776	1 498	508
ParmaTetravision	Mobile	Road Scene	No	Yes[d]	Yes	10240	11554	11451	8338

Table 5.1: Datasets comparison for pedestrian classification and detection

[a] Complete occlusion labels
[b] Only cropped BB are provided
[c] Non-occluded and partially occluded labels provided
[d] Just two class label: occluded and non-occluded

124

In comparison with these two datasets, Caltech [36], Daimler Monocular [39], Daimler Multi-Cue [41] , ETH [43] and KITTI [39] are all captured in an urban scenario with a camera mounted on a vehicle or stroller (as in the case of ETH).

Caltech [36] is one of the most challenging monocular databases having a huge number of annotated pedestrians for both training and testing datasets. Daimler Monocular [39] provides cropped BB of pedestrians in the training set, but road sequences of images for the testing.

Daimler Multi-Cue [41] is a multi modal dataset that contains cropped pedestrian and non-pedestrian BB, but with information from visible, depth and motion. ETH [43] is a dataset acquired mostly on a side walk using a stroller and a stereovision setup, thus it has both temporal information (images are provided in a sequence) and the possibility of using the disparity information. KITTI object dataset [57] is a newer dataset that contains stereo images with annotated pedestrians, cyclists and cars. Although it does not have the possibility of using temporal information, there is the possibility of using 3D laser data.

Infrared Domain.

Aside from the datasets from the Visible domain, we have considered also the dataset ParmaTetravision. This contains images from both Visible and Infrared. Moreover the dataset contains stereo-images, thus making an interesting dataset for comparing different domains and modalities. An overview of available datasets in Infrared Domain is given in chapter 2.2.

In what follows, we are going to use for the experiments the dataset Daimler Multi-Cue for Visible domain, and ParmaTetravision for Infrared domain. The reason why we didn't chose for Infrared domain RIFIR dataset, is because it does not contain stereo images.

5.4   Preliminaries

Throughout this chapter, for the experiments we are going to use the following configuration:

Classifier.   In terms of classifier we have chosen to work with Support Vector Machine. For this, we have used the library LibLinear[44].

Domains.   This chapter contains two major parts: section 5.5 that focuses on Visible domain and section 5.7 that deals with Far-Infrared domain.

Modalities.   As modalities we will study Intensity, from Visible and Infrared domain, and Depth and Motion computed using the information from the Visible domain.

Features. In terms of features we compare HOG (as presented in section 1.4.1), ISS (as presented in section 2.3), LBP (as presented in section 1.4.2), LGP (as presented in section 1.4.3), HaarWavelets (as presented in section 1.4.5) and MSVZM (Mean Scale Value Zero Mean).

In what concerns MSVZM we have implemented a variation based on the feature MSVD described in section 1.4.6. MSVD is a feature proposed specially for Disparity modality. The difference between our implementation and the one proposed by Walk et al. [128] is that we compute a zero-mean and perform $L1$ normalization, which results in a better performance.

5.5 Multi-modality pedestrian classification in Visible Domain

For the dataset used for the first set of experiments, that of feature comparison for the problem of pedestrian classification in Visible domain, we have used the dataset Daimler Multi-cue proposed by Enzweiler et al. [41]. The dataset is publicly available and contains cropped pedestrians at a dimension of 96×48 pixels, along with manually annotated negative examples. It is a good benchmark for feature comparison in different modalities due to available information from intensity, flow and disparity.

	Pedestrians (labeled)	Pedestrians (jittered)	Non-Pedestrians
Train Set	6514	52112	32465
Partially Occluded Test Set	620	11160	16235
Non-Occluded Test Set	3201	25608	16235

Table 5.2: Training and test set statistics for Daimler Multi-Cue Dataset

5.5.1 Individual feature classification

For this experiment, we use each feature independently, HOG, ISS, LBP, LGP, Haar Wavelets and MSVZM, operating in each modality (intensity, depth or motion).

First of all, we have compared MSVD and MVDZM by drawing the ROC curves corresponding to the classification of the Daimler non-occluded dataset using only Depth information (see figure 5.1). Based on the ROC curve, at a classification rate of 90%, the false positive rate for MSVD is of 0.391, while for the MVDZM is of 0.36. Even if we use $L1$ normalization for MSVD the false positive rate remains at 0.39 therefore it seems that the process of zero mean lowers the error.
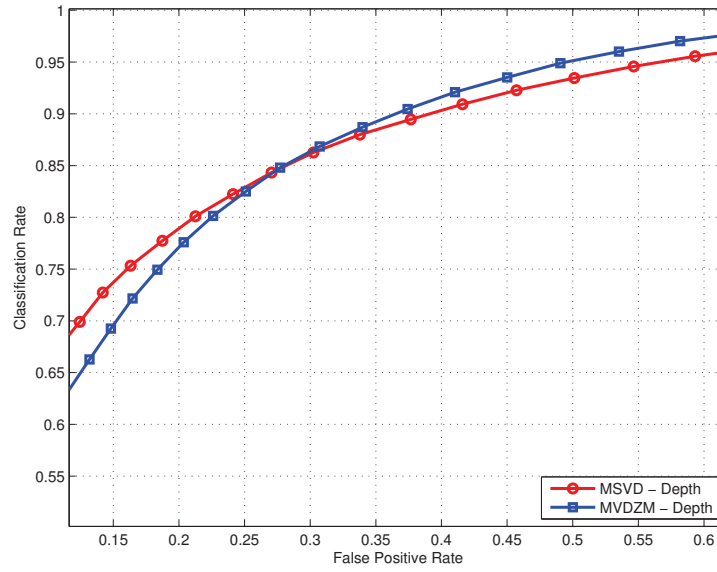
Figure 5.1: Comparison of Mean Scaled Value Disparity and Mean Value Disparity Zero Mean

In figure 5.2 are presented the performance of different features, independently on each domain, and on obtained testing set with no occlusions, while in figure 5.4 the same experiments are performed on the partially occluded testing set.

Enzweiler and Gavrila [40] have also compared HOG and LBP features independently on each modality and have drawn the conclusion that classifiers in the intensity modality have the best performance, by a large margin. Overall, we draw the same conclusions, but in a different light. Several features computed on Intensity domain indeed give the best overall performance (HOG, LBP and LGP), but other features perform better in the depth domain (ISS, Haar Wavelets and MSVZM). On the whole, the best performance is obtained by HOG features on the intensity domain, but followed very closely by LGP computed also on Intensity. In the Depth domain, ISS attains the lowest error rate, followed closely by LGP. HOG, even if on the Intensity gave the best results, in the Depth domain proves to be less robust than ISS or the texture based features like LGP and LBP. Haar Wavelets and MSVZM have overall, on all three domains, a poor performance in comparison with the other features.

In figure 5.3, to better visualize differences between features, we plot for each modality the results obtained with different features, along with the best performing feature on each modality.

By caring on the same set of experiments on the testing set with partial occlusions, we could observed that this time there is a turnover: the best domain is the depth one, giving the best results for HOG, ISS, LBP and LGP, while for Haar Wavelets and MSVZM the motion has the best results. ISS features, although had a very good performance on the Depth domain for the non-occluded testing set, in the presence of occlusion are less robust, being outperformed by LGP,

LBP and HOG. The most robust feature is LGP computed on the Depth domain, by quite a large margin in comparison with the other considered features. Of course, in order to treat occlusions there exist better techniques [41],[47], [48], [59], than the holistic one employed here, but our desired was to test the robustness of each feature across different modalities. Further results on the partially occluded testing set using different features are presented in appendix F.1.
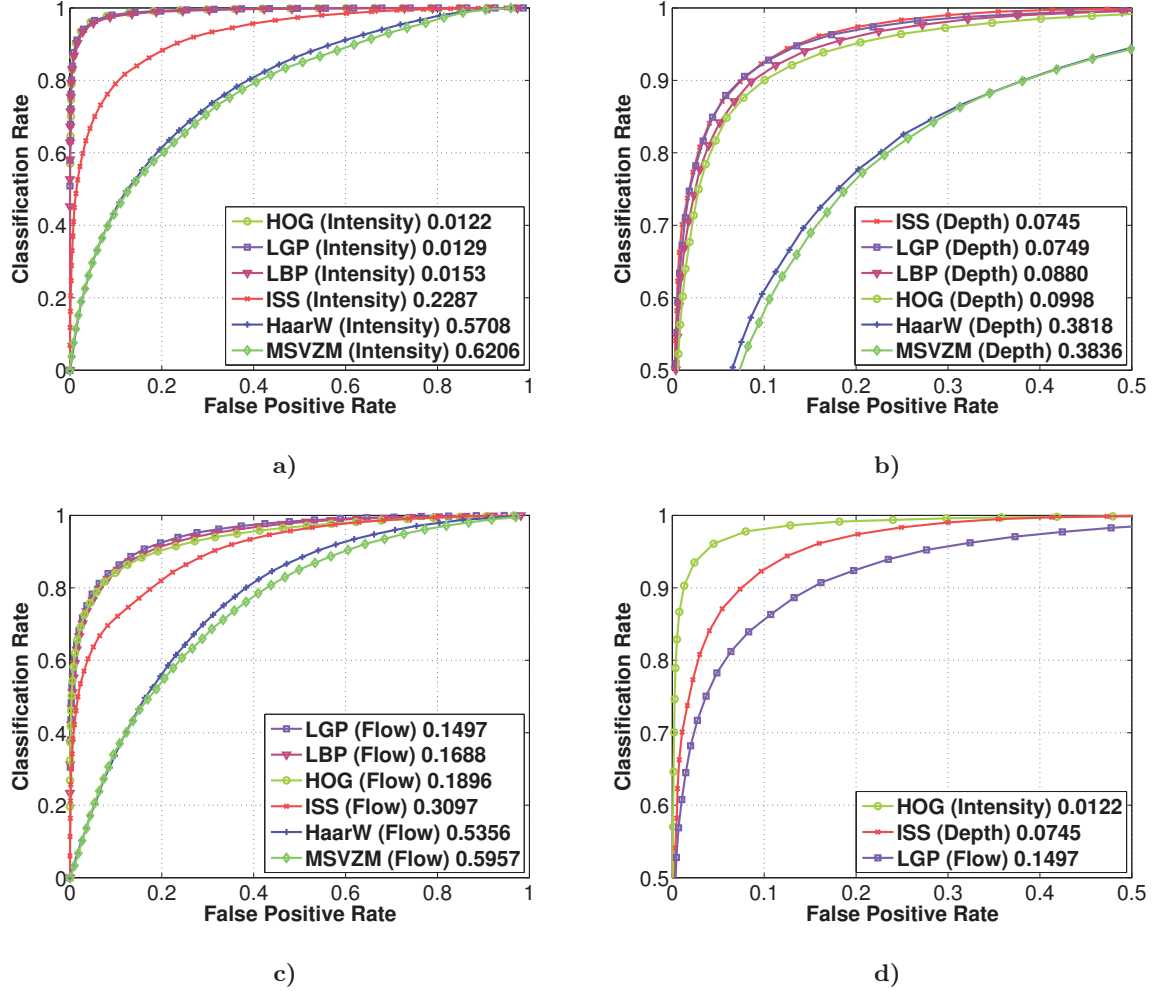
Figure 5.3: Individual classification performance comparison of different features in the three modalities: a) Intensity; b) Depth; c) Motion; d) Best feature on each modality

5.5.2 Feature-level fusion

After having analysed the effect of each modality independently for different features, we now evaluate the effect of using for a given feature, *modality fusion*. Results are given in figure 5.5. For all features, one can always observe an improvement when fusing the information provided by different modalities.

The best single modality for HOG, LBP and LGP is the Intensity. But, by fusing Depth and Motion modalities, is obtained a similar performance with that given by Intensity. In what
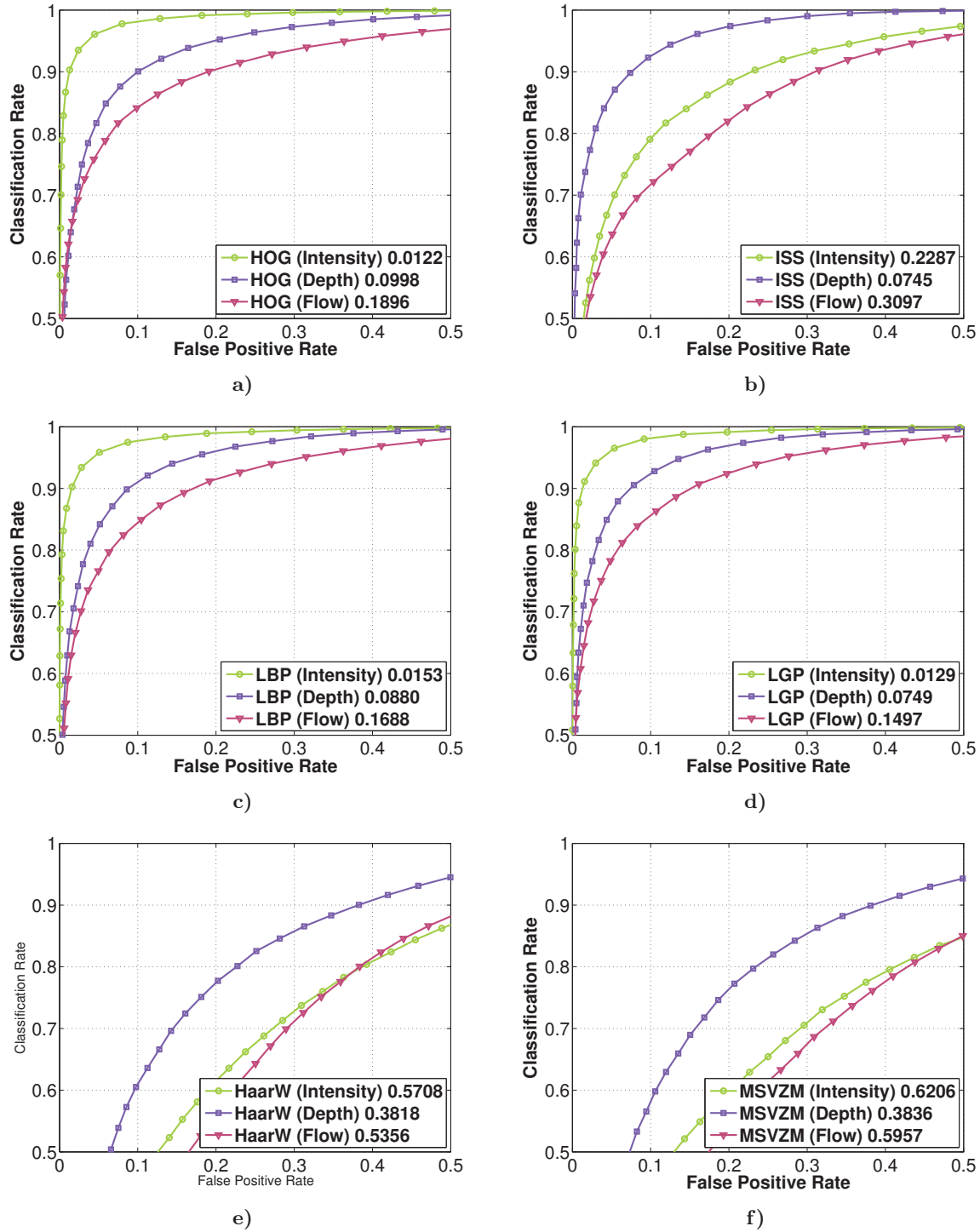
Figure 5.2: Individual classification (intensity, depth, motion) performance of on non-occluded Daimler dataset a) HOG; b) ISS; c) LBP; d) LGP; e) Haar Wavelets; f) MSVZM . The reference point is considered the obtained false positive rate for a classification rate of 90%.
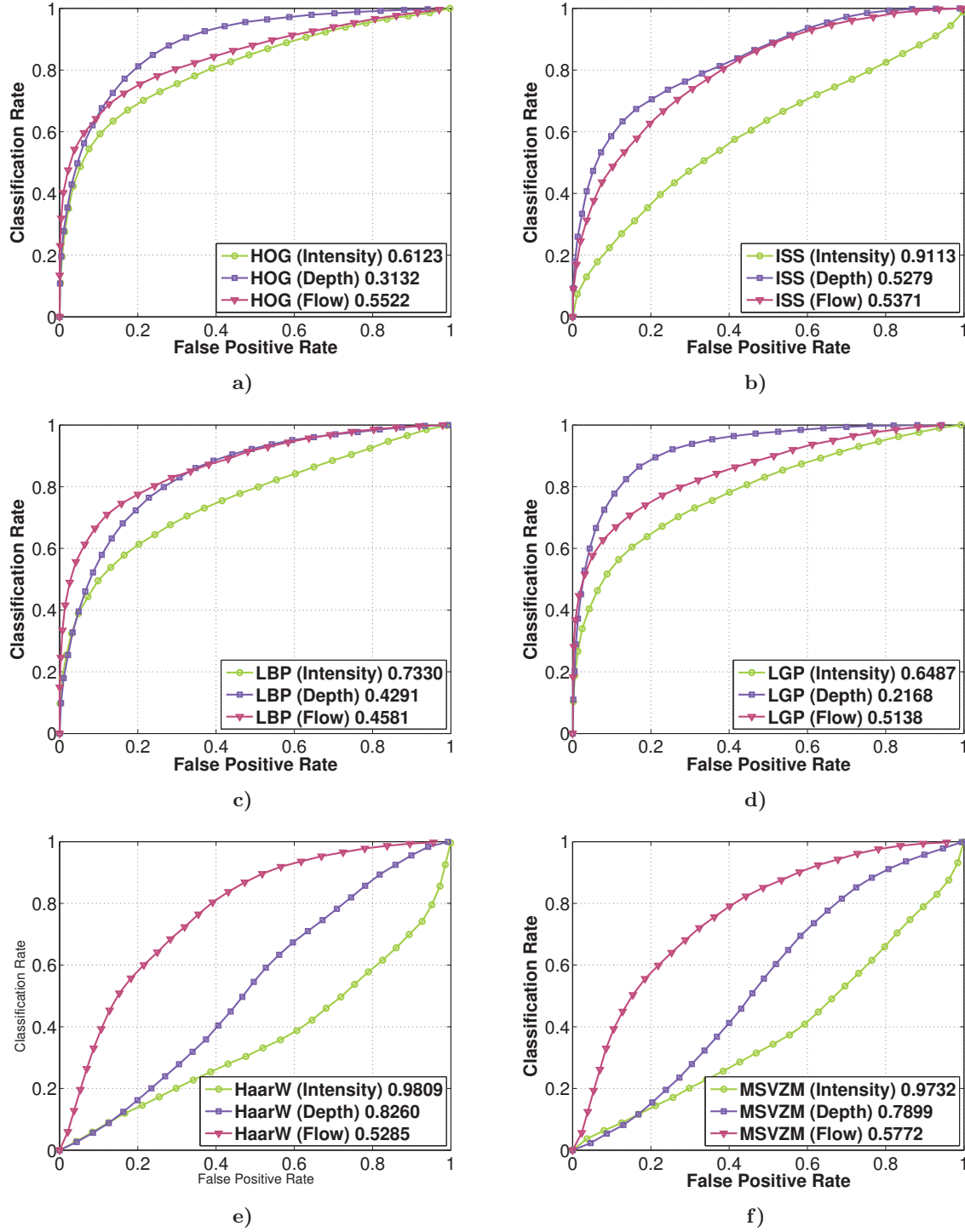
Figure 5.4: Individual classification (intensity, depth, motion) performance on the partial occluded testing set of a) HOG; b) ISS; c) LBP; d) LGP; e) Haar Wavelets; f) MSVZM

concerns the other possible fusions per feature, they always provide a smaller false positive rate than any modality used alone.

As a single modality, Depth always performed better than Motion. When used in combination with Intensity, the fusion of Intensity and Motion seems to give lower error rate than the combination Intensity and Depth for the features HOG, LBP and LGP. For ISS features, because they have a good performance on Depth, the situation is reversed. For the other two considered features, Haar Wavelets and MSVZM, the fusion of Intensity and Depth also has a better performance than Intensity and Flow, even if it is at a relative higher overall error.

Fusing Intensity with Depth using a HOG classifier has approximative a factor of 2.6 of less false positives than a comparable HOG classifier using intensity only; a Intensity and Motion fusion has a factor of 4.5 less false positives, while all three channels fusion has a factor of approximative 11 less false positives than the HOG classifier based on Intensity. Taking as reference the same HOG classifier based on Intensity, the fusion of Depth with Intensity using LBP based classifier has also a factor of 2.6 less false positives, while an LGP based classifier has a factor of 3.

Using modality fusion for ISS feature also lowers the error rate in comparison with a single modality ISS, but the diminishement in the false positive rate is less significant. The same behaviour is for Haar Wavelets and MSVZM features.

No matter what is the feature employed, the fusion of all three modalities always lowers the false positive rate. In figure 5.6.a) is showed a comparison of performance when using all modalities fusion for different features. The best features in term of performance are HOG, LGP and LBP with a difference in the false positive rate extremely low. These are followed by ISS feature, but with a factor of approximately *ten* of higher false positive rate.

While the fusion of all three modalities of HOG feature has the lowest false positive rate at a classification rate of 90%, the fusion of best feature on each modality seems to be slightly more robust overall. These results are presented in figure 5.6.b).

In figure 5.7 we compare a classifier based on the best feature on each modality (HOG on Intensity, ISS on Depth and LGP on Motion), with inter-feature fusion on all modalities. The best performing system is a classifier trained on four features (HOG, ISS, LGP and LBP) and all three modalities, having an approximative factor of 50 less positives than a comparable HOG classifier using Intensity.
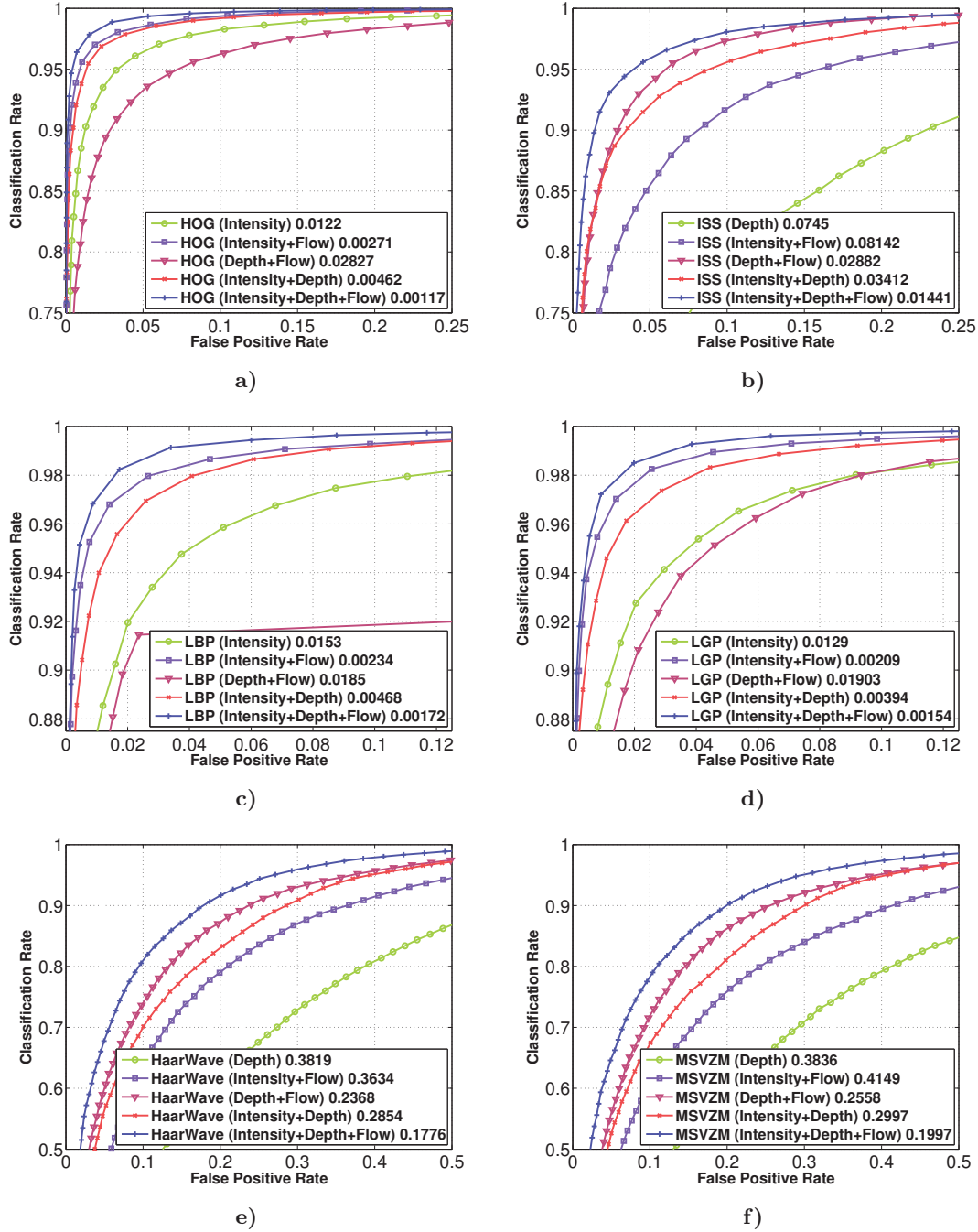
Figure 5.5: Classification performance comparison for each feature using different modality fusion (Intensity+Motion; Depth+Motion; Intensity+Depth; Intensity+Depth+Flow) and the best single modality for each feature: a) HOG; b) ISS; c) LBP; d) LGP; e) Haar Wavelets; f) MSVZM.
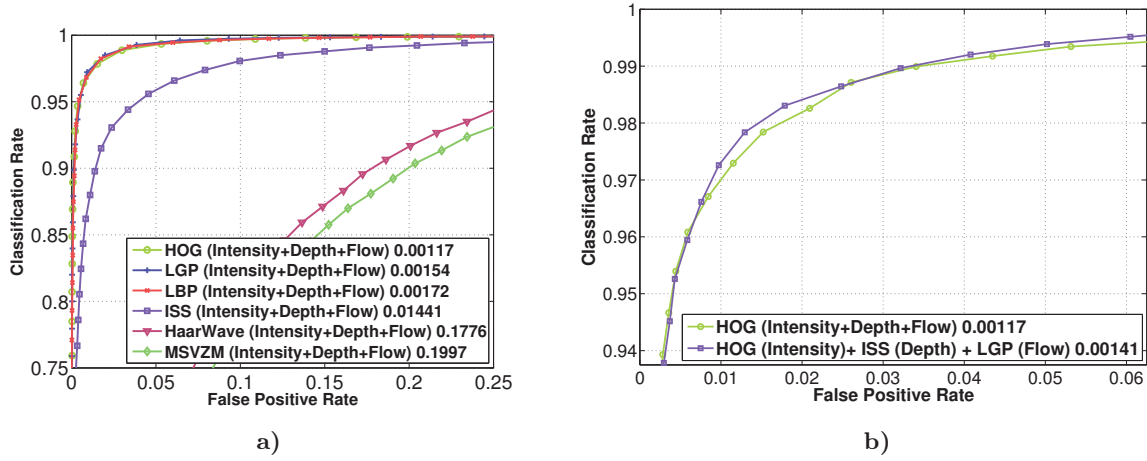
Figure 5.6: Classification performance comparison between different features using all modality fusion per feature **(a)** along **(b)** with a comparison between the best feature modality fusion (HOG on Intensity, Depth and Flow) and the best performing feature on each modality (HOG on Intensity, ISS on Depth and LGP computed on Motion)
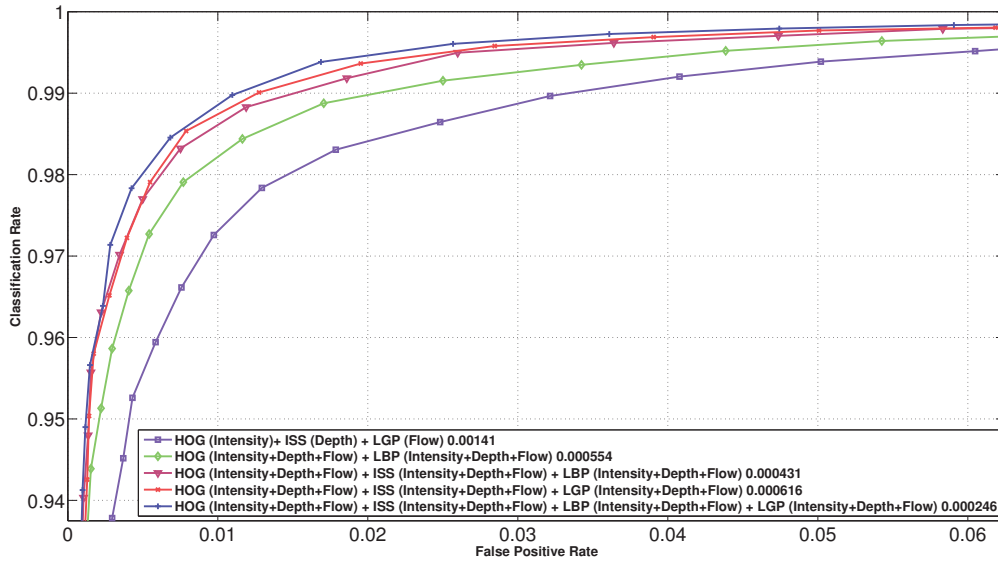
Figure 5.7: Classification performance comparison between the fusion of best performing feature on each modality (HOG on Intensity, ISS on Depth and LGP on Motion) with all modalities fusion of different features (HOG and LBP; HOG, ISS and LBP; HOG, ISS and LGP; HOG, ISS, LBP and LGP)

5.6 Stereo matching algorithm comparison for pedestrian classification

In the same way as different features yield different performance in the classification task, different stereo matching algorithms can lead to a variation in the error rate for the same feature.

In the previous section, for the experiments performed on Daimler Multi-cue dataset, the Disparity was pre-computed by the authors using a semi-global matching algorithm [66]. Since they don't provide the initial Stereo images, there is no possibility of recomputing the Depth map using another stereo matching algorithm. Thus, in order to be able to compare different stereo matching algorithms, we have used as dataset ParmaTetravision.
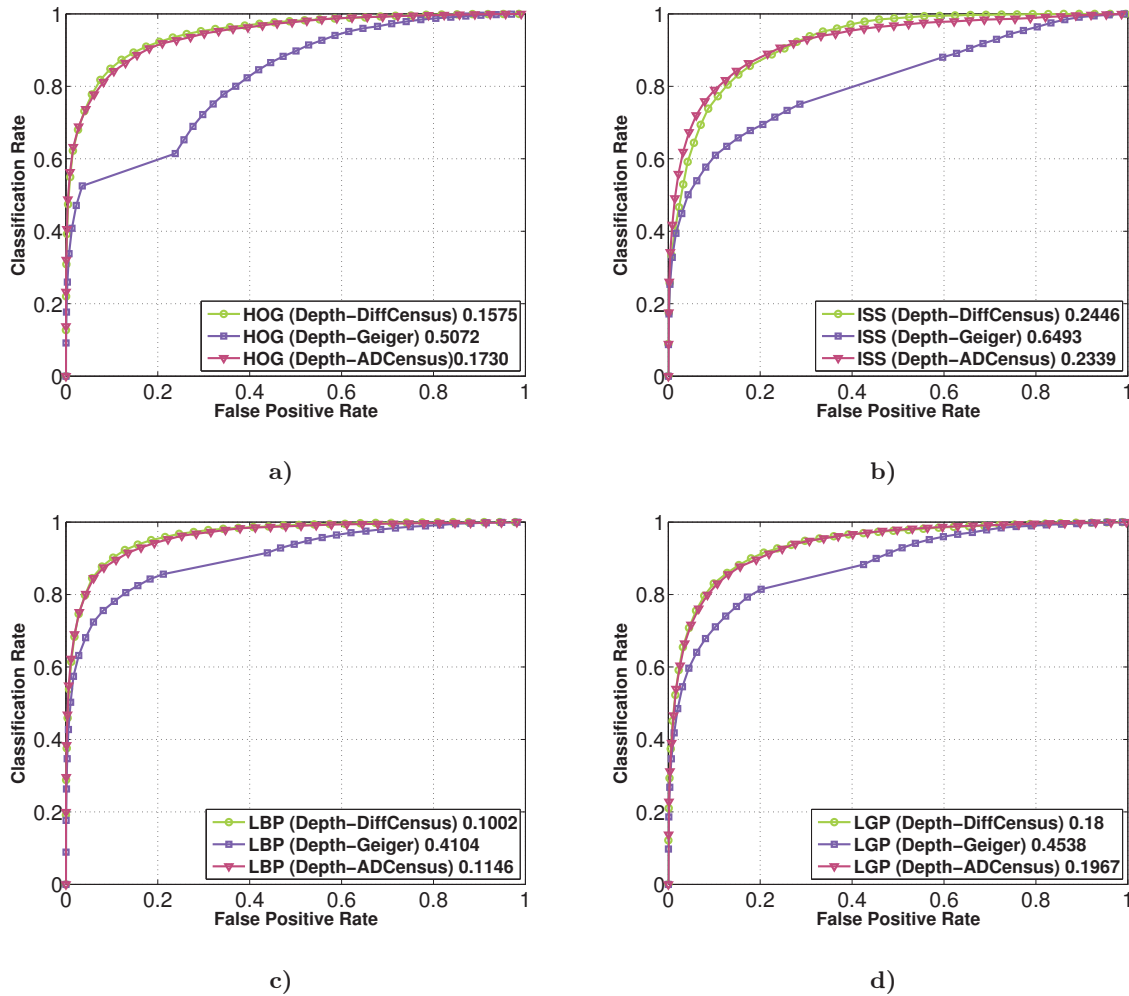
Figure 5.8: Classification performance comparison of three stereo matching algorithms from the perspective of four features: a) HOG , b) ISS, c) LBP, d) LGP.

Three different Disparity maps were computed on ParmaTetravision using three different stereo matching algorithms in combination with different features. The purpose of this is to test if the error difference between these algorithms found in the Disparity map reflects in an error

difference when using Depth information for the classification task.

We have chosen the following stereo matching algorithms:

- Local stereo matching based on a cost function of DiffCensus computed in a square window aggregation and used in combination with cross zone voting (as proposed in chapter 4.3.5.2).

- The same algorithm as described above, but this time just changing the cost function with ADCensus [93].

- An efficient stereo matching algorithm proposed by Geiger et al. [56], which is based on triangulation on a set of support points that can be robustly matched. This algorithm achieved good results on the KITTI dataset, while in the same time has a fast running time.

a)

b)

c)
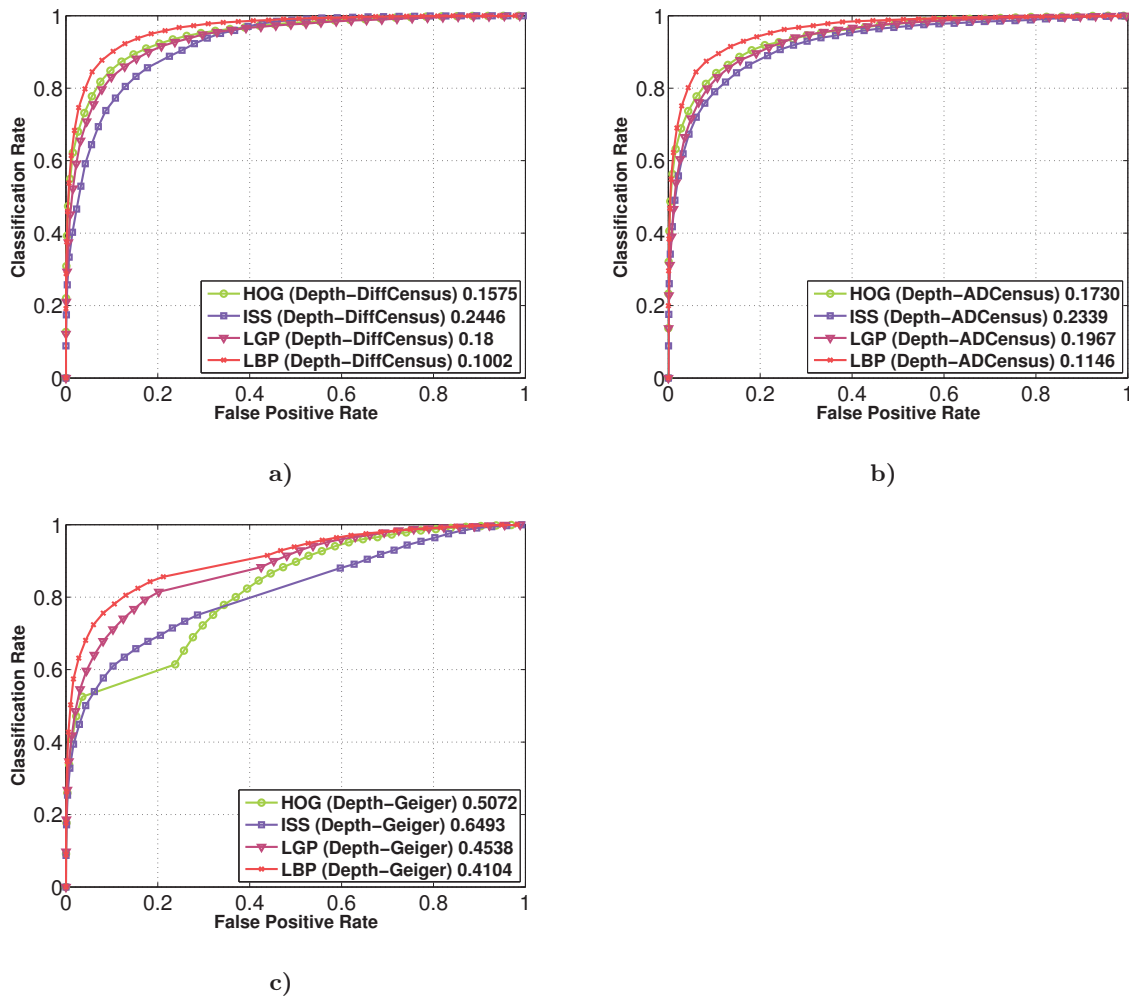
Figure 5.9: Classification performance comparison between different features (HOG, ISS, LGP, LBP) for Depth computed with three different stereo matching algorithms: a) Local stereo matching using DiffCensus cost, b) Local stereo matching using ADCensus cost, c) Stereo matching using the algorithm proposed by [56]

The results of comparison in performance of the stereo matching algorithm for different

features are presented in figure 5.8. Overall, the lowest false positive rate is obtained by the DiffCensus-based stereo matching algorithm, followed closely by the same algorithm but this time using as cost function ADCensus. The stereo matching algorithm proposed by Geiger et al. [56] has a higher false positive rate for all the considered features.

In figure 5.9 we present the same results but in a different light. This time we consider separately each stereo matching algorithm, and we plot the results obtained with different features for that algorithm. We can observe that LBP gives consistently a lower error rate for all three stereo matching algorithms. This is followed by HOG feature in the case of the cross-based stereo matching using DiffCensus or ADCensus, while for the algorithm proposed by Geiger et al. [56], LGP gives better results than HOG.

In general the stereo matching algorithm proposed by the Geiger et al. [56] provides slightly better results than the cross-based algorithm in terms of disparity error[1]. Nevertheless, due to the fact that Geiger et al. [56] only considers the robust regions, for the task of classification, this leads a loss in information in the regions for which is difficult to compute the disparity map. In the case of the cross-based stereo matching algorithm using DiffCensus or ADCensus, we don't disregard the regions for which the disparity map has a high error rate. Thus, in our opinion, even if we extract features on a disparity map where some errors exist, the classification algorithm manages to learn and even extract information from these errors.

5.7 Multi-modality pedestrian classification in Infrared and Visible Domains

In section 2.4 we have presented experiments comparing the visible domain and the far-infrared domain on two datasets: ParmaTetravision and RIFIR. ParmaTetravision dataset in comparison with RIFIR, provides information from two visible cameras, therefore the possibility of performing Stereo matching.

In this section, we extend the experiments on the ParmaTetravision classification dataset, by evaluating the performance of Depth modality in comparison with Intensity from Visible and Intensity from FIR domain.

In the same way that we have done the analysis for the Daimler database, we firstly compare each feature individually on each modality. We have chosen for comparison four features: HOG, ISS, LBP and LGP and four modalities: Intensity given by Visible Domain, Depth computed from pair of Visible Stereo Images (using the Stereo matching algorithm based on Cross zone and

---

[1]The assessment was done visually, since we don't have a ground truth for the disparity map

DiffCensus cost function - see section 5.6), Motion using Visible images and Intensity values give by Far-Infrared Domain. The later will be further referenced as simply IR.

For the experiments shown in section 5.7.1 and 5.7.2 we have computed a disparity map based on the algorithm proposed in chapter 4: for fast computation we employed a square aggregation window of 7×11 pixels, combined with a voting strategy in a cross window, and a DiffCensus cost function. In what concerns the dense optical flow algorithm we have used the implementation provided by Sun et al. [116].

5.7.1 Individual feature classification

In figure 5.10 are presented the performance of each feature on each individual modality. For each feature, the best performing modality is that of Infrared, followed by Visible and Depth.

The best performing feature on Visible is LBP with a factor of *two* of less false positives than a comparable HOG classifier on Visible. This is in comparison with the dataset Daimler, where HOG had the best performance.

On the Infrared modality, the best performing feature is LGP, followed closely by LBP. HOG and ISS features on Infrared have also a similar performance but they have a larger error rate: LGP has a factor of *five* of less false positives than the comparable HOG classifier on Infrared.

On Depth modality, the best performing feature is LBP, followed this time by HOG. Even if on Daimler dataset ISS feature had the best results on Depth, on the ParmaTetravision it is not very robust, having a factor of *two* more false positives than the LBP.

In what concerns the Motion modality, in comparison with the experiments performed on Daimler dataset where LGP gave the best results, on these images the best performing feature was HOG. We believe that this variation in results is given by the quality of the dense optical flow image obtained. Nevertheless, because of the important difference in performance between Flow and Intensity modalities, for the fusion of modalities we will consider for now only Infrared Intensity (IR) , Visible Intensity, and Depth.
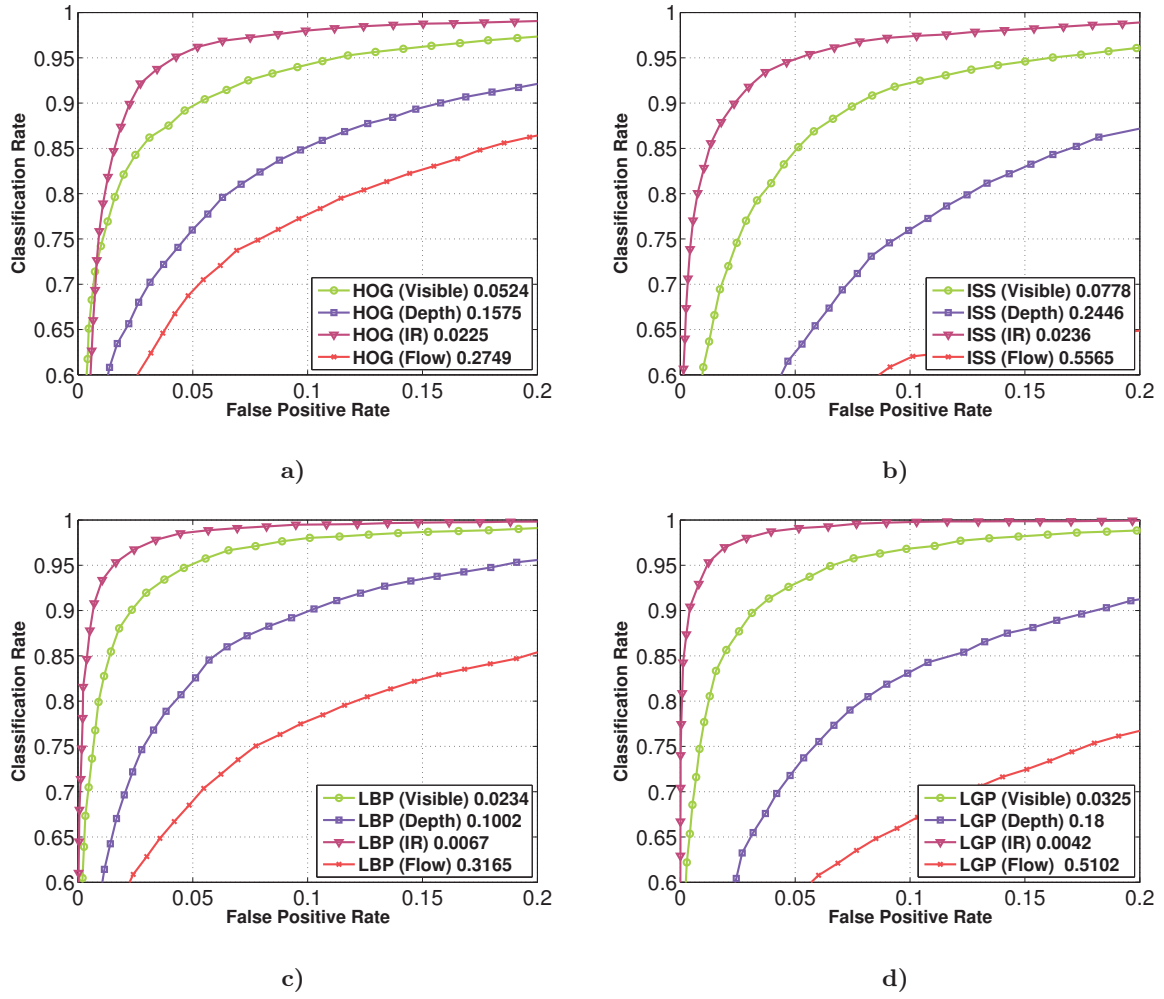
Figure 5.10: Individual classification (visible, depth, flow and IR) performance of a) HOG; b) ISS; c) LBP; d) LGP;
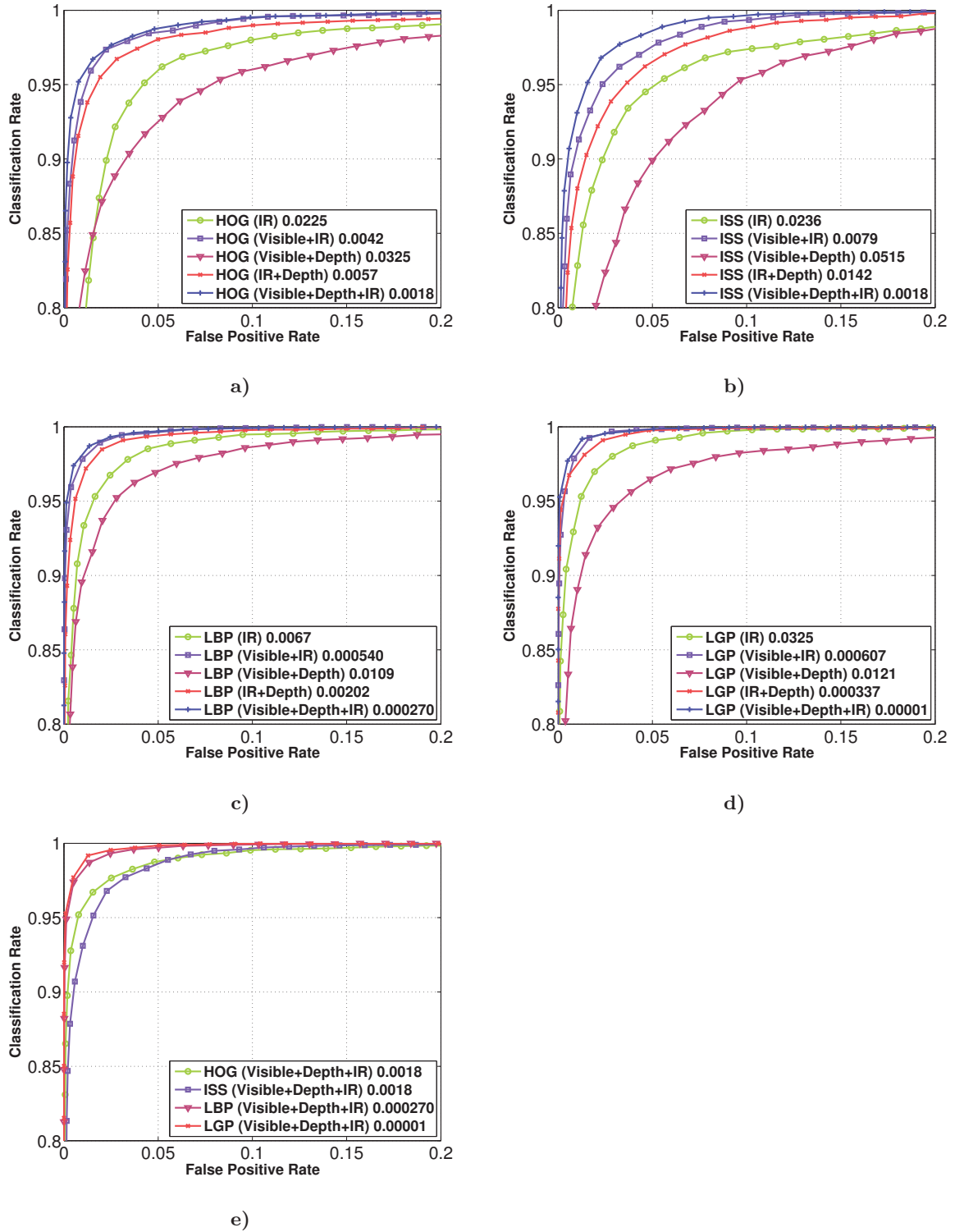
Figure 5.11: Classification performance comparison for each feature using different modality fusion (Visible+IR; Visible+Depth; IR+Depth; Intensity+Depth+IR) and the best single modality for each feature: a) HOG; b) ISS; c) LBP; d) LGP. In order to highlight differences between different features, in e) is plotted for comparison of all modality fusion for different features.

5.7.2 Feature-level fusion

In figure 5.11 we compare for each feature different modality fusions: Visible with Infrared, Visible and Depth, Infrared and Depth, along with all three modalities fusion: Visible, Depth and Infrared. The fusion of Visible and Depth lowers the false positive rate for all features in comparison with the results obtained just on Visible Modality. This result are consistent with the results obtained on Daimler dataset. Unfortunately, they are still not as good as those obtained just by the Infrared modality.

Fusing Infrared and Depth on the other hand, lowers the false positive rate in comparison with just the Infrared modality. For the fusion of Infrared and Depth with HOG feature there is a factor of approximately of *four* less false positives than the just the HOG on Infrared. For ISS, the factor is just of 1.6 and for LBP the factor is of 3.3. The biggest improvement in the context of fusion of Infrared and Depth, is for LGP feature with a staggering factor of 96 less false positives than just the LBP feature on Infrared.

The fusion of all three modalities Visible, Infrared and Depth provides the overall best results for all features. In comparison with Daimler dataset where HOG features had the best results, on ParmaTetravision HOG and ISS modality fusion have a similar false positive rate. However, the family of local binary features are much more robust. LBP on Visible, Depth and IR has a factor of *nine* less false positives than the similar HOG classifier trained on the same three modalities. LGP on the other hand has a factor of over 100 less false positives than the HOG classifier.

5.8 Conclusions

In this chapter we have studied the impact of multi-modality (intensity, depth, motion) usage over the pedestrian classification results. Various features have different performances across modalities. As single modality, Intensity has the best performance on both tested datasets (Daimler and ParmaTetravision), followed by Depth. Nevertheless, the fusion of modalities provides the most robust pedestrian classifier. As single features, local based patterns features (LGP, LBP) have consistently given robust results, but overall a fusion of complementary features as well as modalities had the best performance.

Even if the fusion of Intensity and Depth lowers the false positive rate for all features in comparison with the results obtained just on Intensity in Visible Modality, on the tested dataset, the Intensity values from the FIR domain had consistently lower error rate. On the other hand, a fusion between the two domains, FIR and Visible, along with information given by the disparity map has given the best results on the ParmaTetravision dataset.

6

Conclusion

In this thesis we have focused on the problem of pedestrian detection and classification using different domains (FIR, SWIR, Visible) and different modalities (Intensity, Motion, Depth Map), with a particular emphasis on the Disparity map modality.

FIR. We have started by analysing Far-Infrared Spectrum. For this, we have annotated a large dataset, ParmaTetravision. Because this dataset is not publicly available, we have also acquired a new dataset called RIFIR. This has allowed us to construct a benchmark in order to analyse the performance of different features, and in the same time tof compare FIR and Visible spectrums. Moreover, we have proposed a feature adapted for thermal images, called ISS. Altough ISS has a similar performance with that of HOG in the far infrared spectrum, local-binary features like LBP or LGP proved to be more robust. Moreover, in our tests, FIR consistently proved to be superior to Visible domain. Nevertheless, the fusion between Visible and FIR gave the best results, lowering the false positive rate with factor of ten in comparison with just using the FIR domain.

Since one of the main advantages of thermal images is the fact that the search space for possible pedestrians can be reduced to hot regions in the image, future work should include a benchmark of ROI extraction algorithms. Moreover, we can extend the feature comparison by testing different fusion techniques in order to find the most appropriate configuration.

SWIR With the advent of new camera sensors, a promising new domain is represented by Short-Wave Infrared (SWIR). In this context, we have experimented with two types of cameras. The preliminary experiments that were performed on a dataset that we have annotated, ParmaSWIR. This contains images taken using different filters with the purpose of isolation of different bandwidths. Since the results were promising, we have acquired another dataset, RISWIR, this time using both a SWIR and a Visible camera. On RISWIR, the short-wave infrared provided

better results than the Visible one. In our opinion, this is due to the fact that acquired images in SWIR spectrum are sharper, having well-defined edges.

Further tests in SWIR domain should include different meteorological conditions, along with an evaluation during night conditions. Moreover, we believe for the results to be conclusive, SWIR cameras should be compared against several Visible cameras.

StereoVision Since Visible domain represents a low cost alternative to other spectrums, we give a special attention to Depth modality obtained by constructing the disparity map using different stereo matching algorithms. In this context, we have worked to improve existing stereo matching algorithms by proposing new cost function robust to radiometric distortions. As future work we plan on analysing the impact that post-processing algorithms have over the disparity map. In addition, in order to incorporate the findings of chapter 5, we should improve the information contained in the areas subject to occlusions.

Multi-domain, multi-modality. In a similar manner with the way human perception uses clues given by depth and motion, a new direction of research is the combination of different modalities and features. A lot of articles tacked this problem from different features point of view for the Visible domain. Daimler Multi-cue dataset provides a way to centralize this analysis. In this context we have extended the number of features compared on the dataset with different modalities, along with several fusion scenarios. The best results were always obtained by fusing different modalities. Moreover, we extended the analysis multi-modality to a multi-domain approach, comparing Visible and FIR on ParmaTetravision dataset. Even if the FIR spectrum continues to give the best results, the fusion between Visible and Depth manages to perform close to the results given by FIR. Moreover, the fusion between Visible, Depth and FIR lowers the false positive rate by a factor of *thirty*, than just the use of FIR information.

As future work, we want to extend the analysis to include more datasets (like ETH [43]), along with a comparison of different new features. Moreover, in the multi-modalities experiments we have only treated the problem of pedestrian classification, but we plan of extending the analysis in a pedestrian detection framework.

There exist various approaches used for the task of pedestrian detection and classification task. In this thesis, we have showed that a multi-modality, multi-domain approach, and furthermore multi-feature, is essential for a good pedestrian classification system.

Table A.1: Color space comparison using **No Aggregation and a Winner takes it all strategy.**

Cost Function	RGB	XYZ	LUV	LAB	HLS	YCrCb	HSV	GRAY
C_{SD}	**66.16**	74.94	66.91	67	70.13	66.52	78	75.64
C_{ADCCC}	34.76	**32.12**	43.07	40.35	53.63	43.32	55.94	34.11
C_{AD}	**66.57**	67.88	67.09	67.28	69.86	66.71	69.11	75.64
C_{CCC}	41.49	**37.35**	53.49	50.01	63.41	54.55	67.13	40.64
C_{CT}	51.43	**48.07**	61.49	58.63	68.99	61.9	72.01	51.09
C_{ADCT}	42.22	**40.01**	49.43	47.33	57.68	49.51	59.33	42.65
$C_{DiffCCC}$	38.77	**35.43**	47.02	44.36	58.67	48	61.39	36.50
C_{DiffCT}	46.94	43.14	52.73	50.81	63.82	53.67	65.67	**42.73**

Table A.2: Color space comparison using **No Aggregation and Window Voting strategy.**

Cost Function	RGB	XYZ	LUV	LAB	HLS	YCrCb	HSV	GRAY
C_{SD}	**30.00**	31.7675	32.4208	32.3042	35.1031	31.7288	33.8995	48.17
C_{ADCCC}	14.76	**13.42**	21.8807	20.0289	28.1008	21.4795	29.8935	15.77
C_{AD}	**31.21**	32.6914	33.4616	33.5808	35.4658	33.0343	34.2492	48.17
C_{CCC}	17.1627	**14.90**	27.2618	24.4854	37.0718	27.575	42.1272	17.16
C_{CT}	19.7743	**17.67**	29.8086	27.1517	38.7429	29.9694	43.5671	20.37
C_{ADCT}	15.6836	**14.45**	21.7888	20.1423	27.3889	21.2061	28.984	16.58
$C_{DiffCCC}$	16.2719	**14.60**	23.938	22.1868	31.8153	23.5583	34.4055	16.40
C_{DiffCT}	16.7015	**15.10**	22.817	21.5034	30.8558	22.8666	32.6899	16.69

Table A.3: Color space comparison using **No Aggregation and Cross Voting strategy.**

Cost Function	RGB	XYZ	LUV	LAB	HLS	YCrCb	HSV	GRAY
C_{SD}	23.1853	24.6221	23.8924	23.4984	35.6116	**21.74**	34.5799	43.62
C_{ADCCC}	9.8853	**9.53**	12.0777	11.057	23.8956	11.8662	25.0917	10.26
C_{AD}	25.2124	25.9624	24.8991	24.6209	35.9399	**23.36**	35.1634	43.62
C_{CCC}	10.8492	**9.98**	14.0195	12.6536	32.452	14.0836	38.5133	10.35
C_{CT}	13.8631	**12.78**	18.4191	17.1274	36.3517	17.6975	42.7936	13.76
C_{ADCT}	10.6197	**10.33**	13.0203	11.9332	24.2607	11.8536	25.0075	11.31
$C_{DiffCCC}$	11.0843	**10.47**	13.4342	12.2978	27.4328	13.1517	29.6087	10.50
C_{DiffCT}	12.3039	**11.28**	14.3126	13.553	28.2325	13.6517	29.7005	11.50

Table A.4: Color space comparison using **Window Aggregation and Winner take it all strategy.**

Cost Function	RGB	XYZ	LUV	LAB	HLS	YCrCb	HSV	GRAY
C_{SD}	28.843	26.8752	24.0554	24.6697	45.5687	24.0179	45.0384	**22.47**
C_{ADCCC}	16.3617	**15.22**	22.4926	20.8911	27.7786	21.7776	28.7909	16.85
C_{AD}	21.56	**20.52**	22.2395	22.938	27.83	22.2445	26.7601	21.55
C_{CCC}	16.3865	**14.55**	25.6282	23.1288	35.0064	25.1609	39.2748	16.51
C_{CT}	16.9811	**15.27**	25.6533	23.0397	34.0793	25.0693	37.9766	17.26
C_{ADCT}	16.7156	**15.52**	22.5112	20.8071	27.5222	21.9147	28.5869	17.13
$C_{DiffCCC}$	17.2878	**15.92**	23.7943	22.164	30.5305	23.1127	32.0148	16.77
C_{DiffCT}	17.2317	**16.02**	22.6881	21.4227	29.0603	22.3661	29.624	17.20

Table A.5: Color space comparison using **Window Aggregation and Window Voting strategy.**

Cost Function	RGB	XYZ	LUV	LAB	HLS	YCrCb	HSV	GRAY
C_{SD}	26.135	24.3667	20.9516	21.3165	43.0206	20.7607	42.8491	**19.04**
C_{ADCCC}	14.897	**14.09**	20.0291	18.7216	24.6324	19.4426	25.3579	15.31
C_{AD}	18.0667	**17.20**	18.6889	19.1435	23.1094	18.6812	22.1849	18.00
C_{CCC}	14.4862	**13.22**	22.1633	20.1229	30.6773	21.5609	34.4548	14.62
C_{CT}	14.8307	**13.66**	21.6604	19.4697	28.9722	20.9686	32.296	14.99
C_{ADCT}	14.9334	**14.10**	19.6912	18.0869	23.8878	19.0941	24.6584	15.14
$C_{DiffCCC}$	15.668	**14.64**	21.2967	19.7834	27.1354	20.6203	28.3192	15.13
C_{DiffCT}	15.5516	**14.72**	20.1489	18.8904	25.4204	19.7925	25.8481	15.36

Table A.6: Color space comparison using **Window Aggregation and Cross Voting strategy.**

Cost Function	RGB	XYZ	LUV	LAB	HLS	YCrCb	HSV	GRAY
C_{SD}	12.6762	**12.42**	12.918	13.0423	21.5226	12.5993	20.6503	12.92
C_{ADCCC}	10.8963	**10.34**	12.7115	11.4688	20.31	12.2459	20.3794	10.99
C_{AD}	12.268	**12.13**	12.707	12.9205	19.3606	12.4246	18.5638	12.96
C_{CCC}	10.4625	**9.66**	12.8513	11.6512	25.5045	12.6764	28.9731	10.36
C_{CT}	11.005	**10.50**	13.7054	11.8693	24.1079	12.7627	26.1566	11.35
C_{ADCT}	11.2006	**10.74**	13.168	11.9889	19.8799	12.2537	20.0019	11.53
$C_{DiffCCC}$	11.5268	**10.75**	13.5024	12.1339	22.7681	12.814	23.7329	10.76
C_{DiffCT}	11.7755	**11.16**	13.8078	12.6727	21.3157	12.977	21.5008	11.62

Table A.7: Color space comparison using **Cross Aggregation and Winner Takes it all strategy.**

Cost Function	RGB	XYZ	LUV	LAB	HLS	YCrCb	HSV	GRAY
C_{SD}	18.7188	**18.65**	19.503	19.7141	35.7187	19.4803	33.4478	19.89
C_{ADCCC}	12.3434	**11.86**	14.6939	13.8241	27.9153	14.3914	28.259	11.94
C_{AD}	17.1391	**16.88**	17.495	17.7178	31.9723	17.5203	30.1517	17.37
C_{CCC}	11.9277	**11.03**	15.7659	14.0439	35.0787	15.1236	40.6607	11.52
C_{CT}	14.2699	**13.18**	18.4644	16.1716	38.1547	17.039	43.9023	13.63
C_{ADCT}	13.1236	**12.50**	15.4782	14.3622	29.2378	14.8011	29.6902	12.70
$C_{DiffCCC}$	13.2558	12.6632	15.1867	14.0014	30.1137	14.8062	31.3186	**11.67**
C_{DiffCT}	14.1111	13.3458	15.9304	15.0104	30.7311	15.586	30.9725	**12.99**

Table A.8: Color space comparison using **Cross Aggregation and Window Voting strategy.**

Cost Function	RGB	XYZ	LUV	LAB	HLS	YCrCb	HSV	GRAY
C_{SD}	**15.22**	15.3307	16.6239	16.863	24.2304	16.821	22.4271	16.76
C_{ADCCC}	10.9851	**10.64**	13.3125	12.596	21.8262	13.0357	21.6177	10.93
C_{AD}	**13.98**	13.9967	15.0722	15.2701	21.9465	15.2162	20.5315	14.70
C_{CCC}	10.0924	**9.64**	13.0713	11.9509	26.597	12.7037	30.164	10.22
C_{CT}	10.878	**10.43**	13.8252	12.3969	25.7543	12.701	28.6817	10.97
C_{ADCT}	11.3643	**10.84**	13.5748	12.6573	21.0923	12.9682	21.3276	11.15
$C_{DiffCCC}$	11.8087	11.415	13.8045	12.7777	23.6381	13.5168	24.1776	**10.75**
C_{DiffCT}	12.348	11.806	14.1029	13.4131	22.3486	13.8942	22.5228	**11.62**

Table A.9: Color space comparison using ***Cross Aggregation and Cross Voting strategy.***

Cost Function	RGB	XYZ	LUV	LAB	HLS	YCrCb	HSV	GRAY
C_{SD}	**14.77**	14.8463	16.2026	16.3635	24.611	16.4097	22.9833	16.11
C_{ADCCC}	10.2129	**9.92**	11.9966	11.5529	21.2961	12.0302	21.0467	10.49
C_{AD}	**13.57**	13.6026	14.6569	14.809	21.8622	14.8233	20.642	14.11
C_{CCC}	9.41481	**8.92**	11.3475	10.7914	25.775	11.47	29.0424	9.80
C_{CT}	10.077	**9.68**	11.9903	11.0646	25.4984	11.2415	28.2317	10.39
C_{ADCT}	10.6396	**10.08**	12.1749	11.8233	20.7813	12.1242	21.0541	10.68
$C_{DiffCCC}$	11.0808	10.6242	12.3572	11.5996	23.064	12.2227	23.917	**10.22**
C_{DiffCT}	11.4388	10.9748	12.9124	12.5185	22.282	12.7513	22.4395	**10.94**

Parameters algorithms stereo vision

Parameter	Value
Subpixel Computation	false
I_threshold1	5
I_threshold2	8
Interaction Radius	6
Lambda 1	15
Lambda 1	5
K	25
Occlusion Penalty	10000
Maximum number of iterations	1
Randomize every iteration	true

Table B.1: Parameters Algorithms Graph Cuts

Parameter	Value
Arm Length Vertical	10
Arm Length Horizontal	17

Table B.2: Parameters Algorithms Cross Zone Aggregation

Disparity Map image examples

a) Visible left image *0*
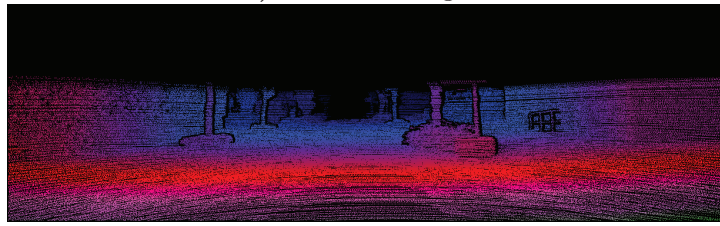
b) Ground truth image *0*
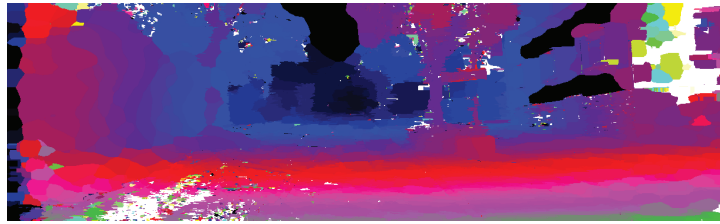
c)CZA: C_{CT}: 12.50%
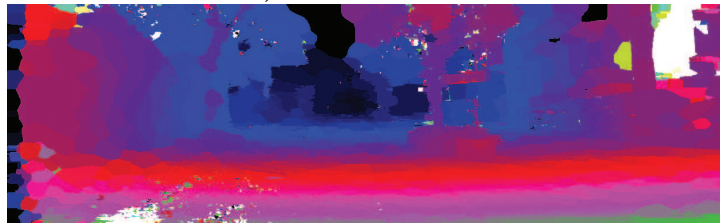
d)CZA: C_{DiffCT}: 7.89%

Figure C.1: Comparison between cost functions. On first row there are presented the left visible image number 0 (**a**) from the KITTI dataset with the corresponding ground truth disparity (**b**). On the following lines are the output obtained with the cross zone aggregation (CZA) algorithm with two different functions: c) Census Tranform; d) the proposed DiffCT
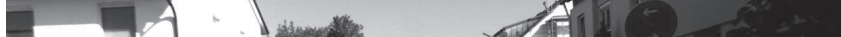
a) Visible left image *0*
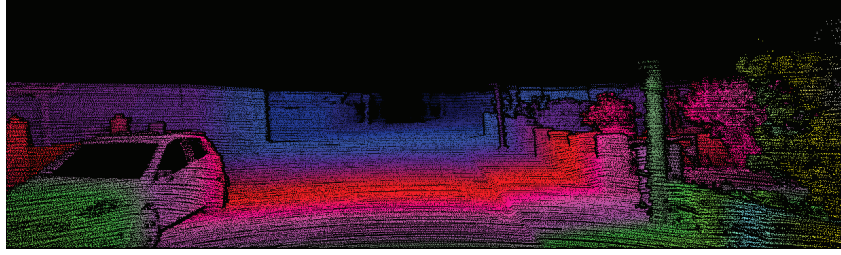
b) Ground truth image *0*

c)CZA: C_{CT}: 15.31%
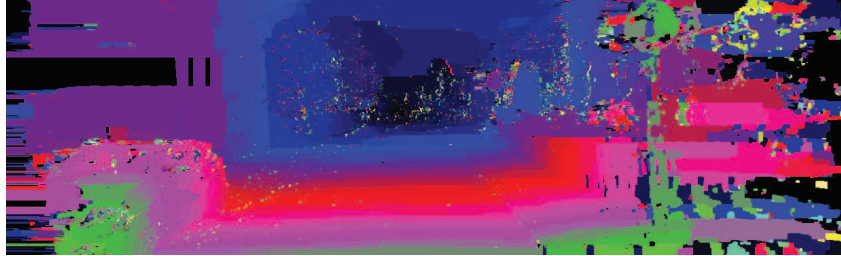
d)CZA: C_{DiffCT}: 14.22%

Figure C.2: Comparison between cost functions. On first row there are presented the left visible image number 2 (**a**) from the KITTI dataset with the corresponding ground truth disparity (**b**). On the following lines are the output obtained with the graph cuts (GC) algorithm with two different functions: c) Census Tranform; d) the proposed DiffCT

Cost aggregation

Aggregation area is a very important step for the local algorithms of stereo matching. Global stereo matching algorithms model in an explicit way the smoothness term (which enforces that spatially close pixels to have similar disparity). Local algorithms having to model the smoothness term in an implicit way, the pixels found in the same aggregation area will have a similar disparity.

As presented in subsection 4.1.3.1 there exist a great variety of methods for construction a cost aggregation area, from the window aggregation areas to adaptive windows or cross-zone aggregation.
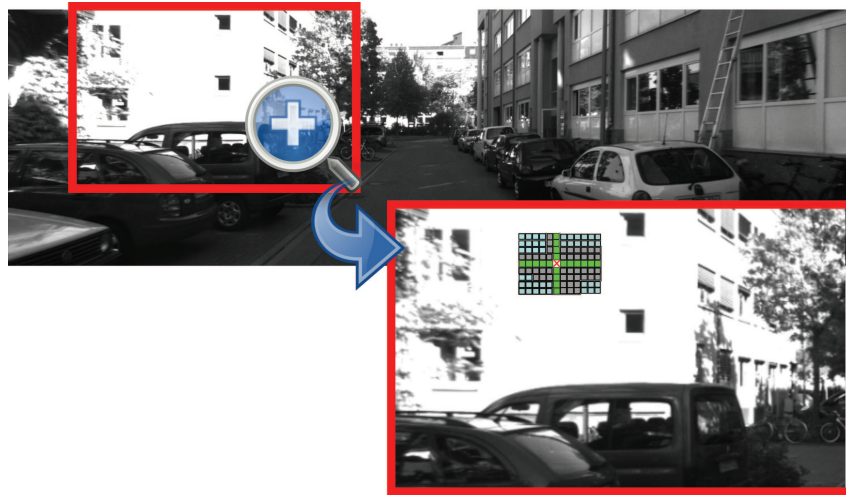
Figure D.1

In section 4.3.5.2 we described the method proposed by Zhang et al. [137]. Mei et al. [93] proposed an extension for the algorithm of cross-zone aggregation, by using two thresholds for the maximum area of aggregation:

1. $D_c(p_l, p) < \tau_1$ and $D_c(p_l, p_l + (1,0)) < \tau_1$

2. $D_s(p_l, p) < L_1$

(a) Left Image

(b) Ground Truth

(c) Zhang et al. (2009) (7.73%)

(d) Mei et al. (2011) (10.58%)
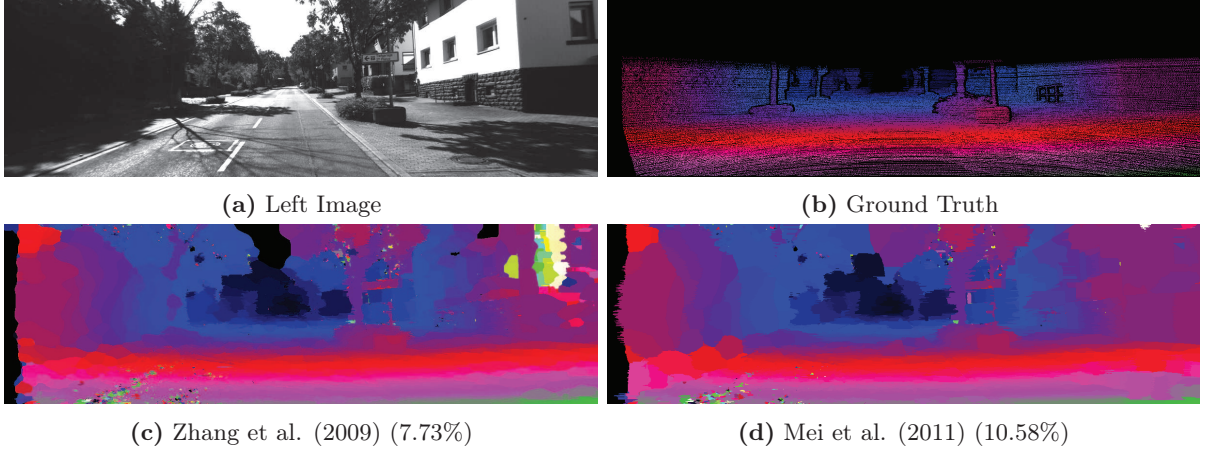
Figure D.2: Different cost aggregation strategies: a) Left Image; b) Disparity Ground Truth; c) Disparity map computed using the strategy proposed by Zhang et al. [137]; d) Disparity map computing using the strategy proposed by Mei et al. [93]

    3. $D_c(p_l, p) < \tau_2$ if $L_1 < D_s(p_l, p) < L_2$

where L_1, L_2 are distance thresholds, τ_1, τ_2 are color thresholds, $D_c(p_l, p)$ is a color difference of two pixels, while $D_s(p_l, p)$ is a spatial distance between two pixels.

Based on the above rules, the arms of the cross zones are contructed in the following way: the first color threshold (τ_1) and first size threshold (L_1) are used the same way as by Zhang et al. [137]; in order for the arm to not run across edges a color restriction is enforced between p_l and its predecessor $p_l + (1, 0)$ on the same arm; for second size threshold (L_2) should be large enough in order to cover the large textureless areas, but in this case a second color threshold much more restricive is used (τ_2). This strategy gives very good results on the Middlebury dataset therefore we have tested it on KITTI dataset as well.

Unfortunately, this method of constructing the cross area does not improve the results. The overall error on the training set from KITTI database is of 21% in comparison with 12.70% obtained using the strategy of Zhang et al. [137]. We don't deny the impact of the strategy proposed by Mei et al. [93] in the textureless areas parallel with the camera plane (see figure D.2, window area in the right side of the image), but this comes at a higher error rate in the inclined areas, as that of the road regions.

$\mathcal{E}$

Voting-based disparity refinement

In section 4.3.5.2 we have briefly presented the cross-based cost aggregation proposed by Zhang et al. [137]. The initial disparity is selected for each pixel using a Winner Takes-All (WTA) method. Because the aggregated costs can be usually similar at different disparities, the WTA will not give very good results. Moreover, WTA strategy has difficulties to handle pixels in the occluded regions. The refinement scheme proposed by Lu et al. [90] and use also by Zhang et al. [137] consists in a local voting method.

For every pixel p, having a disparity estimate d_p cumputed with WTA, a histogram h_p of disparities is build as showed by equation E.1:

$$h_p(d) = \sum_{q \in U(p)} \delta(d_q, d) \qquad (E.1)$$

where $U(p)$ represents the set of all aggregation areas that contain the pixel p, and the function δ is defined as follows:

$$\delta(d_a, d_b) = \begin{cases} 1 & \text{if } d_a = d_b \\ 0 & \text{otherwise} \end{cases}$$

$$d_p^* = argmax(h_p(d)) \qquad (E.2)$$

where $d \in [0, d_{max}]$.

Different from Zhang et al. [137], we propose an extension for the voting algorithm. Due to the fact that different but close disparities have similar matching costs, the surface of inclined objects will not appear very smooth. Our proposal is for the voting scheme to not only consider the disparity d_p obtained with WTA, but also the disparities in the interval $[d_p - v, d_p + v]$.

(a) Ground Truth

(b) WTA (9.77 %)

(b) Voting Zhang et al. (2011) (7.49%)

(c) Our proposed voting (4.50%)
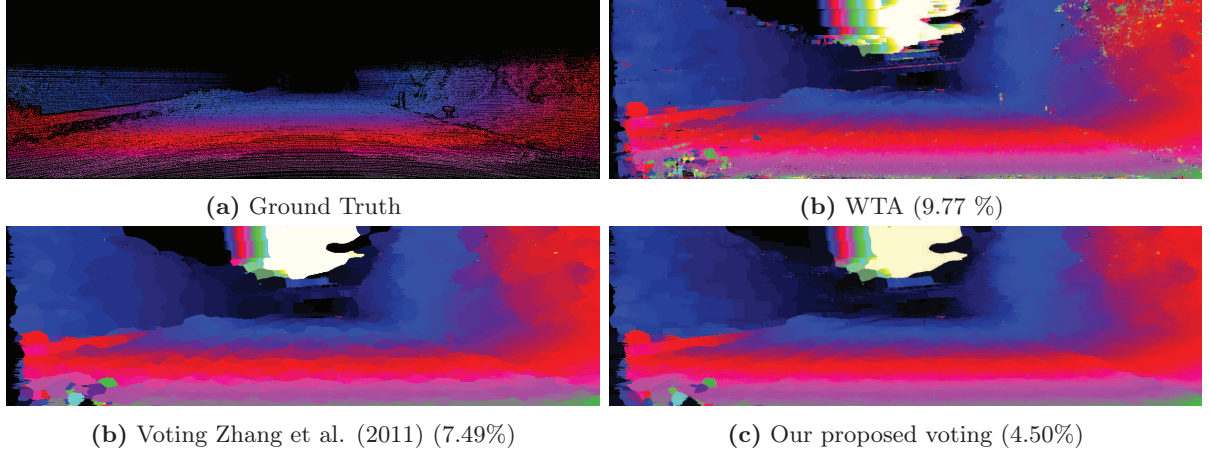
Figure E.1: Different Voting Strategies for the same image

$$h_p(d) = \sum_{d \in [d-v, d+v]} \sum_{q \in U(p)} \delta(d_q, d) \qquad \text{(E.3)}$$

Disparity Decision Strategy	Error Rate
Winner Takes-All	15.05%
Voting Zhang et al. [137]	12.70%
Proposed Voting (v=2)	10.50%

Table E.1: Comparison of different strategy methods for choosing the disparity

In table E.1 is presented a comparison of obtained error rates on the KITTI dataset using cross-zone aggregation, the cost C_{DIFFCF}, and three strategies for deciding the final disparity: WTA, the voting method proposed by Zhang et al. [137], and our proposed voting. It can be observed that by simply adding the votes to a disparity interval rather than just one disparity values the error rate decreases with 2.2%.

F.1   Daimler-experiments - Occluded dataset
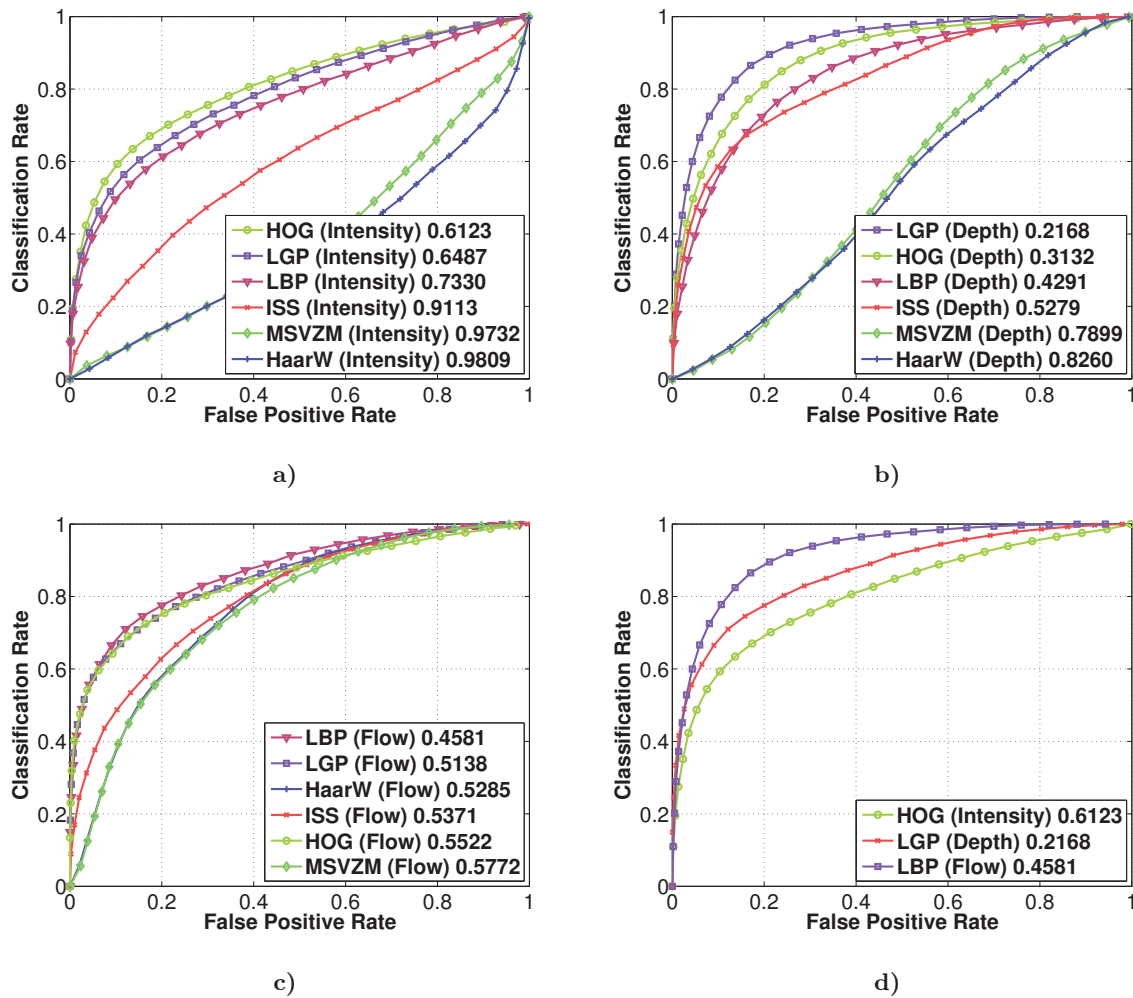
Figure F.1: Individual classification performance comparison of different features in the three modalities for *partially occluded* testing set: a) Intensity; b) Depth; c) Motion; d) Best feature on each modality
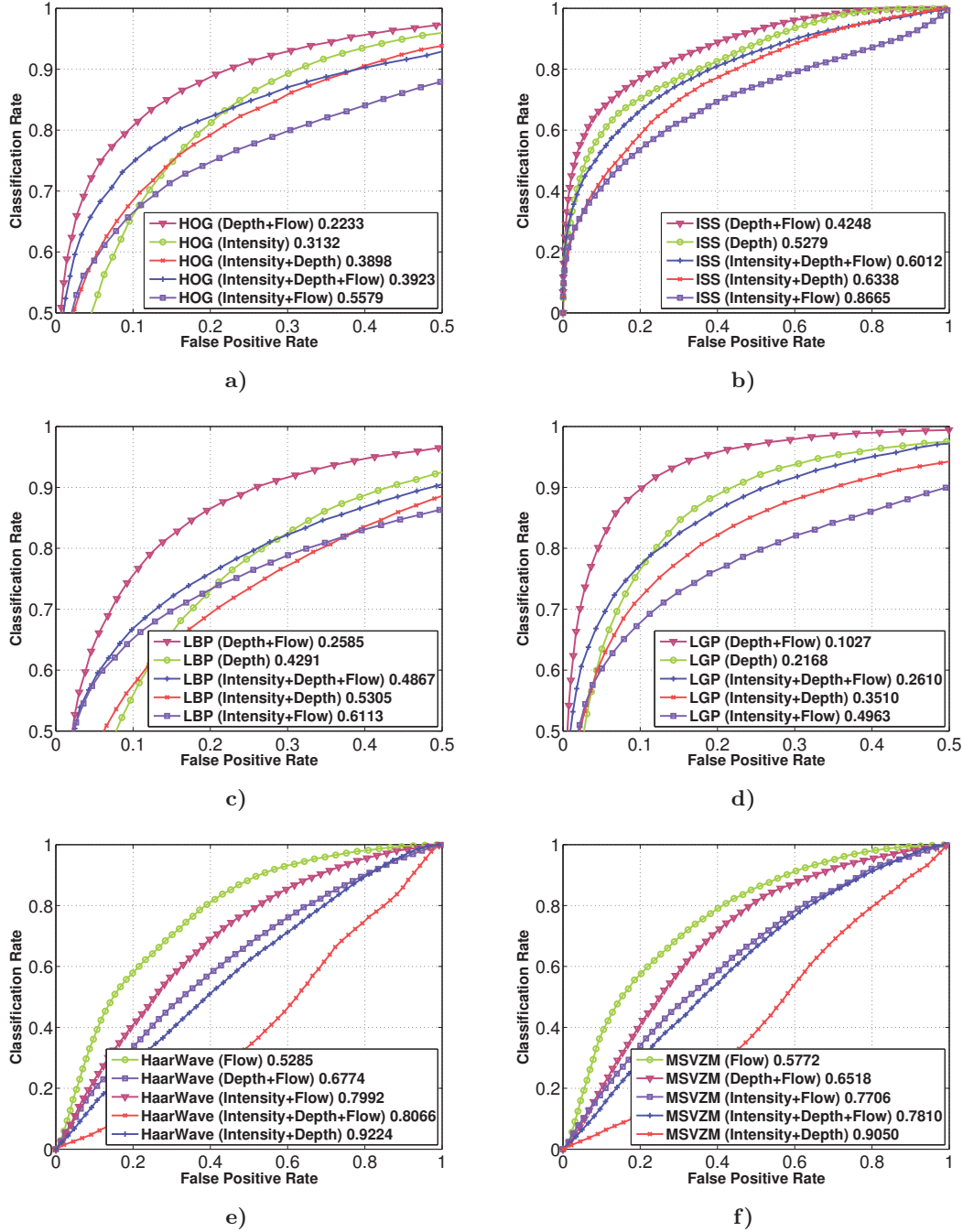
Figure F.2: Classification performance comparison for each feature using different modality fusion on **partially occluded testing set** (Intensity+Motion; Depth+Motion; Intensity+Depth; Intensity+Depth+Flow) and the best single modality for each feature: a) HOG; b) ISS; c) LBP; d) LGP; e) Haar Wavelets; f) MSVZM.
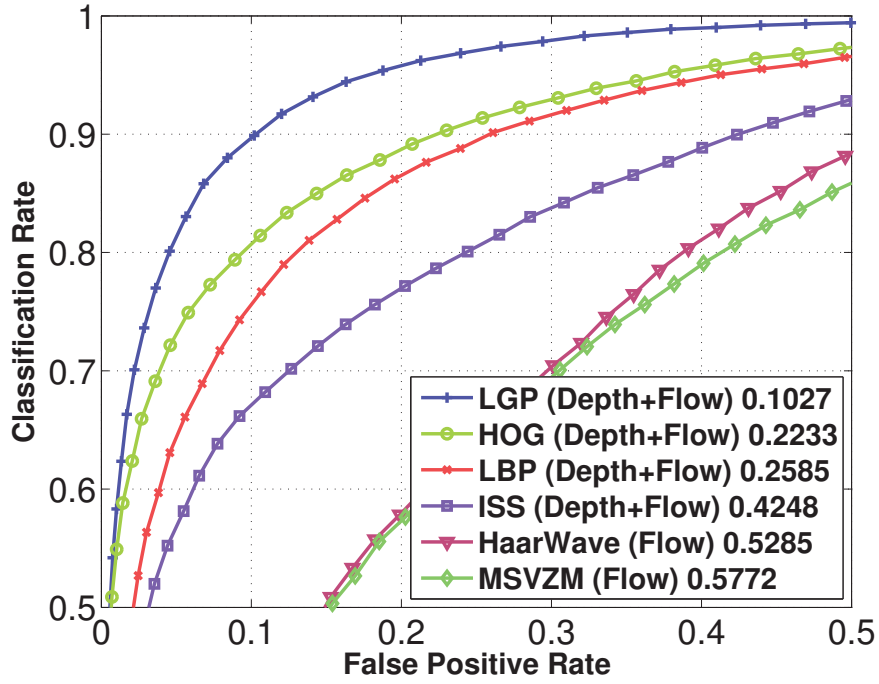
Figure F.3: Classification performance comparison on the partially occluded testing sets between different features using the best modality fusion per feature
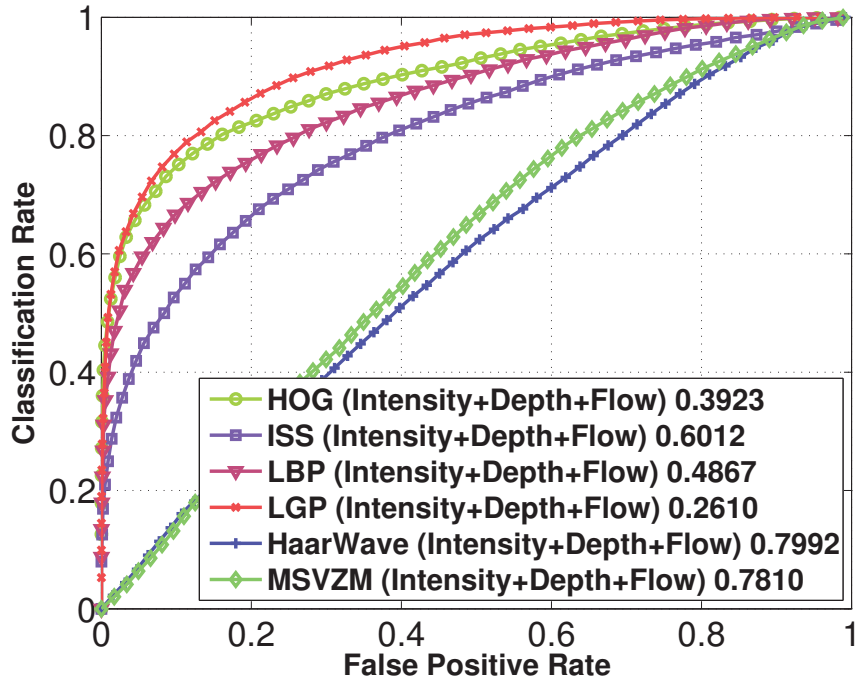
Figure F.4: Classification performance comparison on the partially occluded testing sets between different features using the all modality fusion per feature

Bibliography

[1] The vislab intercontinental autonomous challenge. *http://viac.vislab.it/*, 2010.

[2] L. Andreone, F. Bellotti, A. De Gloria, and R. Lauletta. Svm-based pedestrian recognition on near-infrared images. In *Proceedings of the 4th International Symposium on Image and Signal Processing and Analysis*, pages 274–278. IEEE, 2005.

[3] A. Apatean, A. Rogozan, and A. Bensrhair. Objects recognition in visible and infrared images from the road scene. In *IEEE International Conference on Automation, Quality and Testing, Robotics, 2008*, volume 3, pages 327–332, 2008.

[4] Gregory P Asner and David B Lobell. A biogeophysical approach for automated swir unmixing of soils and vegetation. *Remote Sensing of Environment*, 74(1):99–112, 2000.

[5] Max Bajracharya, Baback Moghaddam, Andrew Howard, Shane Brennan, and Larry H Matthies. A fast stereo-based system for detecting and tracking pedestrians from a moving vehicle. *The International Journal of Robotics Research*, 28(11-12):1466–1485, 2009.

[6] Emmanuel P Baltsavias and Dirk Stallmann. *SPOT stereo matching for Digital Terrain Model generation*. Citeseer, 1993.

[7] Jasmine Banks and Peter Corke. Quantitative evaluation of matching methods and validity measures for stereo vision. *The International Journal of Robotics Research*, 20(7):512–532, 2001.

[8] Rodrigo Benenson, Radu Timofte, and Luc Van Gool. Stixels estimation without depth map computation. In *IEEE Conference on Computer Vision Workshops (ICCV Workshops)*, pages 2010–2017, 2011.

[9] Rodrigo Benenson, Markus Mathias, Radu Timofte, and Luc Van Gool. Pedestrian detection at 100 frames per second. In *IEEE Conference on Computer Vision and Pattern Recognition (CVPR)*, pages 2903–2910, 2012.

[10] M. Bertozzi, A. Broggi, A. Fascioli, T. Graf, and M.M. Meinecke. Pedestrian detection for driver assistance using multiresolution infrared vision. *IEEE Transactions on Vehicular Technology*, 53(6):1666–1678, 2004.

[11] M Bertozzi, A Broggi, A Lasagni, and MD Rose. Infrared stereo vision-based pedestrian detection. In *Intelligent Vehicles Symposium*, pages 24–29. IEEE, 2005.

[12] M Bertozzi, A Broggi, M Felisa, G Vezzoni, and M Del Rose. Low-level pedestrian detection by means of visible and far infra-red tetra-vision. In *Intelligent Vehicles Symposium*, pages 231–236. IEEE, 2006.

[13] M Bertozzi, A Broggi, C Hilario Gomez, RI Fedriga, G Vezzoni, and M Del Rose. Pedestrian detection in far infrared images based on the use of probabilistic templates. In *Intelligent Vehicles Symposium*, pages 327–332. IEEE, 2007.

[14] Massimo Bertozzi, Emanuele Binelli, Alberto Broggi, and MD Rose. Stereo vision-based approaches for pedestrian detection. In *IEEE Computer Society Conference on Computer Vision and Pattern Recognition-Workshops*, pages 16–16. IEEE, 2005.

[15] Bassem Besbes, Alexandrina Rogozan, and Abdelaziz Bensrhair. Pedestrian recognition based on hierarchical codebook of surf features in visible and infrared images. In *IEEE Intelligent Vehicles Symposium (IV)*, pages 156–161, 2010.

[16] Bassem Besbes, Sonda Ammar, Yousri Kessentini, Alexandrina Rogozan, and Abdelaziz Bensrhair. Evidential combination of svm road obstacle classifiers in visible and far infrared images. In *Intelligent Vehicles Symposium*, pages 1074–1079. IEEE, 2011.

[17] Dinkar N. Bhat and Shree K. Nayar. Ordinal measures for image correspondence. *IEEE Transactions on Pattern Analysis and Machine Intelligence*, 20(4):415–423, 1998.

[18] E. Binelli, A. Broggi, A. Fascioli, S. Ghidoni, P. Grisleri, T. Graf, and M. Meinecke. A modular tracking system for far infrared pedestrian recognition. In *Intelligent Vehicles Symposium*, pages 759–764. IEEE, 2005.

[19] M. Bleyer and S. Chambon. Does Color Really Help in Dense Stereo Matching? In *Proceedings of the International Symposium on 3D Data Processing, Visualization and Transmission (3DPVT)*. Citeseer, 2010.

[20] Michael Bleyer and Margrit Gelautz. Simple but effective tree structures for dynamic programming-based stereo matching. In *International Conference on Computer Vision Theory and Applications (VISAPP)*, pages 415–422, 2008.

[21] Michael Bleyer, Sylvie Chambon, Uta Poppe, and Margrit Gelautz. Evaluation of different methods for using colour information in global stereo matching approaches. *Int. Society for Photogrammetry and Remote Sensing*, pages 63–68, 2008.

[22] Alberto Broggi, Massimo Bertozzi, Alessandra Fascioli, and Massimiliano Sechi. Shape-based pedestrian detection. In *Proceedings of the IEEE Intelligent Vehicles Symposium*, pages 215–220. Citeseer, 2000.

[23] Alberto Broggi, Massimo Bertozzi, and Alessandra Fascioli. Self-calibration of a stereo vision system for automotive applications. In *IEEE International Conference on Robotics and Automation*, volume 4, pages 3698–3703, 2001.

[24] Matthew Brown and Sabine Susstrunk. Multi-spectral sift for scene category recognition. In *IEEE Conference on Computer Vision and Pattern Recognition (CVPR)*, pages 177–184. IEEE, 2011.

[25] Alan Brunton, Chang Shu, and Gerhard Roth. Belief propagation on the gpu for stereo vision. In *The 3rd Canadian Conference on Computer and Robot Vision*, pages 76–76. IEEE, 2006.

[26] I. Cabani, G. Toulminet, and A. Bensrhair. A Fast and Self-adaptive Color Stereo Vision Matching; a first step for Road Obstacle Detection. In *Intelligent Vehicles Symposium*, pages 58–63. IEEE, 2006. ISBN 490112286X.

[27] Pietro Cerri, Luca Gatti, Luca Mazzei, Fabio Pigoni, and Ho Gi Jung. Day and night pedestrian detection using cascade adaboost system. In *13th International IEEE Conference on Intelligent Transportation Systems (ITSC)*, pages 1843–1848. IEEE, 2010.

[28] S. Chambon and A. Crouzil. Colour correlation-based matching. *International Journal of Robotics and Automation*, 20(2):78–85, 2005. ISSN 0826-8185.

[29] Corinna Cortes and Vladimir Vapnik. Support-vector networks. *Machine learning*, 20(3): 273–297, 1995.

[30] Navneet Dalal and Bill Triggs. Histograms of oriented gradients for human detection. In *IEEE Computer Society Conference on Computer Vision and Pattern Recognition*, volume 1, pages 886–893, 2005.

[31] Navneet Dalal, Bill Triggs, and Cordelia Schmid. Human detection using oriented histograms of flow and appearance. In *European Conference on Computer Vision*, pages 428–441. Springer, 2006.

[32] James W Davis and Mark A Keck. A two-stage template approach to person detection in thermal imagery. In *WACV/MOTION*, pages 364–369. Citeseer, 2005.

[33] James W Davis and Vinay Sharma. Background-subtraction using contour-based fusion of thermal and visible imagery. *Computer Vision and Image Understanding*, 106(2):162–182, 2007.

[34] P. Dollár, Z. Tu, P. Perona, and S. Belongie. Integral channel features. *BMVC 2009, London, England*, 2009.

[35] Piotr Dollár, Serge Belongie, and Pietro Perona. The fastest pedestrian detector in the west. In *British Machine Vision Conference*, volume 55, 2010.

[36] Piotr Dollar, Christian Wojek, Bernt Schiele, and Pietro Perona. Pedestrian detection: An evaluation of the state of the art. *IEEE Transactions on Pattern Analysis and Machine Intelligence*, 34(4):743–761, 2012.

[37] Nick A Drake, Steve Mackin, and Jeff J Settle. Mapping vegetation, soils, and geology in semiarid shrublands using spectral matching and mixture modeling of swir aviris imagery. *Remote Sensing of Environment*, 68(1):12–25, 1999.

[38] M Enzweiler, P Kanter, and DM Gavrila. Monocular pedestrian recognition using motion parallax. In *Intelligent Vehicles Symposium*, pages 792–797. IEEE, 2008.

[39] Markus Enzweiler and Dariu M Gavrila. Monocular pedestrian detection: Survey and experiments. *IEEE Transactions on Pattern Analysis and Machine Intelligence*, 31(12): 2179–2195, 2009.

[40] Markus Enzweiler and Dariu M Gavrila. A multilevel mixture-of-experts framework for pedestrian classification. *IEEE Transactions on Image Processing*, 20(10):2967–2979, 2011.

[41] Markus Enzweiler, Angela Eigenstetter, Bernt Schiele, and Dariu M Gavrila. Multi-cue pedestrian classification with partial occlusion handling. In *Conference on Computer Vision and Pattern Recognition (CVPR)*, pages 990–997. IEEE, 2010.

[42] S Erturk. Region of interest extraction in infrared images using one-bit transform. *Signal Processing Letters*, 2013.

[43] Andreas Ess, Bastian Leibe, and Luc Van Gool. Depth and appearance for mobile scene analysis. In *IEEE 11th International Conference on Computer Vision*, pages 1–8. IEEE, 2007.

[44] Rong-En Fan, Kai-Wei Chang, Cho-Jui Hsieh, Xiang-Rui Wang, and Chih-Jen Lin. Liblinear: A library for large linear classification. *The Journal of Machine Learning Research*, 9: 1871–1874, 2008.

[45] Yajun Fang, Keiichi Yamada, Yoshiki Ninomiya, Berthold Horn, and Ichiro Masaki. Comparison between infrared-image-based and visible-image-based approaches for pedestrian detection. In *Intelligent Vehicles Symposium*, pages 505–510. IEEE, 2003.

[46] Pedro F Felzenszwalb and Daniel P Huttenlocher. Efficient belief propagation for early vision. *International journal of computer vision*, 70(1):41–54, 2006.

[47] Pedro F. Felzenszwalb, Ross B. Girshick, and David McAllester. Cascade object detection with deformable part models. In *IEEE Conference on Computer Vision and Pattern Recognition*, pages 2241–2248, 2010.

[48] Pedro F. Felzenszwalb, Ross B. Girshick, David McAllester, and Deva Ramanan. Object detection with discriminatively trained part-based models. *IEEE Transanctions on Pattern Analysis and Machine Intelligence*, 32(9):1627–1645, 2010.

[49] Clinton Fookes, A Maeder, Sridha Sridharan, and Jamie Cook. Multi-spectral stereo image matching using mutual information. In *2nd International Symposium on 3D Data Processing, Visualization and Transmission*, pages 961–968. IEEE, 2004.

[50] The Royal Society for the Prevention of Accidents. What are the most common causes of road accidents? `http://www.rospa.com/faqs/detail.aspx?faq=298`, 2013. Accessed: 2013-12-03.

[51] D.A. Forsyth and J. Ponce. *Computer vision: a modern approach.* Prentice Hall Professional Technical Reference, 2002.

[52] Yoav Freund and Robert E Schapire. A decision-theoretic generalization of on-line learning and an application to boosting. *Journal of computer and system sciences*, 55(1):119–139, 1997.

[53] Andrea Fusiello, Vito Roberto, and Emanuele Trucco. Efficient stereo with multiple windowing. In *IEEE Conference on Computer Vision and Pattern Recognition*, pages 858–863, 1997.

[54] Tarak Gandhi and Mohan M Trivedi. Pedestrian protection systems: Issues, survey, and challenges. *IEEE Transactions on Intelligent Transportation Systems*, 8(3):413–430, 2007.

[55] Dariu M Gavrila and Stefan Munder. Multi-cue pedestrian detection and tracking from a moving vehicle. *International journal of computer vision*, 73(1):41–59, 2007.

[56] Andreas Geiger, Martin Roser, and Raquel Urtasun. Efficient large-scale stereo matching. In *Asian Conference of Computer Vision*, pages 25–38. Springer, 2011.

[57] Andreas Geiger, Philip Lenz, and Raquel Urtasun. Are we ready for autonomous driving? the kitti vision benchmark suite. In *Computer Vision and Pattern Recognition (CVPR)*, Providence, USA, June 2012.

[58] David Geronimo, Antonio M Lopez, Angel Domingo Sappa, and Thorsten Graf. Survey of pedestrian detection for advanced driver assistance systems. *Transactions on Pattern Analysis and Machine Intelligence*, 32(7):1239–1258, 2010.

[59] Ross B Girshick, Pedro F Felzenszwalb, and David A Mcallester. Object detection with grammar models. In *Advances in Neural Information Processing Systems*, pages 442–450, 2011.

[60] Scott Grauer-Gray and Chandra Kambhamettu. Hierarchical belief propagation to reduce search space using cuda for stereo and motion estimation. In *Workshop on Applications of Computer Vision (WACV)*, pages 1–8. IEEE, 2009.

[61] Scott Grauer-Gray, Chandra Kambhamettu, and Kannappan Palaniappan. Gpu implementation of belief propagation using cuda for cloud tracking and reconstruction. In *IAPR Workshop on Pattern Recognition in Remote Sensing*, pages 1–4. IEEE, 2008.

[62] Erico Guizzo. How Google's Self-Driving Car Works. *http://spectrum.ieee.org/automaton/robotics/artificial-intelligence/how-google-self-driving-car-works*, Retrieved 18 October 1011.

[63] Marc P Hansen and Douglas S Malchow. Overview of swir detectors, cameras, and applications. In *SPIE Defense and Security Symposium*, pages 69390I–69390I. International Society for Optics and Photonics, 2008.

[64] Simon Hermann and Reinhard Klette. Iterative semi-global matching for robust driver assistance systems. In *Proc. Asian Conf. Computer Vision, LNCS*, 2012.

[65] H. Hirschmuller and D. Scharstein. Evaluation of cost functions for stereo matching. In *IEEE Conference on Computer Vision and Pattern Recognition*, pages 1–8, 2007. ISBN 1424411807.

[66] Heiko Hirschmuller. Stereo processing by semiglobal matching and mutual information. *IEEE Transactions on Pattern Analysis and Machine Intelligence*, 30(2):328–341, 2008.

[67] Heiko Hirschmuller and Daniel Scharstein. Evaluation of stereo matching costs on images with radiometric differences. *IEEE Transactions on Pattern Analysis and Machine Intelligence*, 31(9):1582–1599, 2009.

[68] Heiko Hirschmüller, Peter R Innocent, and Jon Garibaldi. Real-time correlation-based stereo vision with reduced border errors. *International Journal of Computer Vision*, 47 (1-3):229–246, 2002.

[69] Asmaa Hosni, Michael Bleyer, Margrit Gelautz, and Christoph Rhemann. Local stereo matching using geodesic support weights. In *16th IEEE International Conference on Image Processing (ICIP)*, pages 2093–2096, 2009.

[70] M. Humenberger, C. Zinner, M. Weber, W. Kubinger, and M. Vincze. A fast stereo matching algorithm suitable for embedded real-time systems. *Computer Vision and Image Understanding*, 2010. ISSN 1077-3142.

[71] Sensors Inc. Why swir? what is the value of shorwave infrared? `http://www.sensorsinc.com/whyswir.html`, 2013. Accessed: 2013-10-12.

[72] Bongjin Jun, Inho Choi, and Daijin Kim. Local transform features and hybridization for accurate face and human detection. *Transactions on Pattern Analysis and Machine Intelligence*, pages 1423–1436, 2013.

[73] DS Kim and KH Lee. Segment-based region of interest generation for pedestrian detection in far-infrared images. *Infrared Physics & Technology*, 61:120–128, 2013.

[74] DS Kim, M Kim, BS Kim, and KH Lee. Histograms of local intensity differences for pedestrian classification in far-infrared images. *Electronics Letters*, 49(4):258–260, 2013.

[75] Andreas Klaus, Mario Sormann, and Konrad Karner. Segment-based stereo matching using belief propagation and a self-adapting dissimilarity measure. In *Proceedings of the 18th International Conference on Pattern Recognition - Volume 03*, ICPR '06, pages 15–18. IEEE Computer Society, 2006. ISBN 0-7695-2521-0.

[76] Vladimir Kolmogorov and Ramin Zabih. Computing visual correspondence with occlusions using graph cuts. In *8th IEEE International Conference on Computer Vision*, volume 2, pages 508–515, 2001.

[77] J.Z. Kolter, Y. Kim, and A.Y. Ng. Stereo vision and terrain modeling for quadruped robots. In *IEEE International Conference on Robotics and Automation, 2009*, pages 1557–1564. IEEE, 2009.

[78] Kurt Konolige. Small vision systems: Hardware and implementation. In *ROBOTICS RESEARCH-INTERNATIONAL SYMPOSIUM-*, volume 8, pages 203–212. MIT PRESS, 1998.

[79] Sebastien Kramm and Abdelaziz Bensrhair. Obstacle detection using sparse stereovision and clustering techniques. In *Intelligent Vehicles Symposium (IV)*, pages 760–765. IEEE, 2012.

[80] Stephen J Krotosky and Mohan M Trivedi. On color-, infrared-, and multimodal-stereo approaches to pedestrian detection. *IEEE Transactions on Intelligent Transportation Systems*, 8(4):619–629, 2007.

[81] Stephen J Krotosky and Mohan M Trivedi. A comparison of color and infrared stereo approaches to pedestrian detection. In *Intelligent Vehicles Symposium*, pages 81–86. IEEE, 2007.

[82] Raphael Labayrade, Didier Aubert, and J-P Tarel. Real time obstacle detection in stereovision on non flat road geometry through" v-disparity" representation. In *Intelligent Vehicle Symposium, 2002. IEEE*, volume 2, pages 646–651. IEEE, 2002.

[83] Lubor Ladickỳ, Paul Sturgess, Chris Russell, Sunando Sengupta, Yalin Bastanlar, William Clocksin, and Philip HS Torr. Joint optimization for object class segmentation and dense stereo reconstruction. *International Journal of Computer Vision*, pages 1–12, 2012.

[84] Bastian Leibe, Edgar Seemann, and Bernt Schiele. Pedestrian detection in crowded scenes. In *IEEE Computer Society Conference on Computer Vision and Pattern Recognition*, volume 1, pages 878–885, 2005.

[85] Guoliang Li, Yong Zhao, Daimeng Wei, and Ruzhong Cheng. Nighttime pedestrian detection using local oriented shape context descriptor. In *Proceedings of the 2nd International Conference on Computer Science and Electronics Engineering*. Atlantis Press, 2013.

[86] J. Li, W. Gong, W. Li, and X. Liu. Robust pedestrian detection in thermal infrared imagery using the wavelet transform. *Infrared Physics & Technology*, 53(4):267–273, 2010.

[87] Rainer Lienhart and Jochen Maydt. An extended set of haar-like features for rapid object detection. In *International Conference on Image Processing*, volume 1, pages I–900. IEEE, 2002.

[88] Qiong Liu, Jiajun Zhuang, and Jun Ma. Robust and fast pedestrian detection method for far-infrared automotive driving assistance systems. *Infrared Physics & Technology*, 2013.

[89] David G Lowe. Distinctive image features from scale-invariant keypoints. *International journal of computer vision*, 60(2):91–110, 2004.

[90] Jiangbo Lu, Gauthier Lafruit, and Francky Catthoor. Anisotropic local high-confidence voting for accurate stereo correspondence. In *Proc. SPIE-IS&T Electronic Imaging*, volume 6812, pages 605822–1, 2008.

[91] Mirko Mählisch, Matthias Oberländer, Otto Löhlein, Dariu Gavrila, and Werner Ritter. A multiple detector approach to low-resolution fir pedestrian recognition. In *Proceedings of the IEEE Intelligent Vehicles Symposium (IV2005), Las Vegas, NV, USA*, 2005.

[92] David Marr, Tomaso Poggio, Ellen C Hildreth, and W Eric L Grimson. A computational theory of human stereo vision. In *From the Retina to the Neocortex*, pages 263–295. Springer, 1991.

[93] Xing Mei, Xun Sun, Mingcai Zhou, Shaohui Jiao, Haitao Wang, and Xiaopeng Zhang. On building an accurate stereo matching system on graphics hardware. In *International Conference on Computer Vision Workshops (ICCV Workshops)*, pages 467–474. IEEE, 2011.

[94] U. Meis, M. Oberlander, and W. Ritter. Reinforcing the reliability of pedestrian detection in far-infrared sensing. In *Intelligent Vehicles Symposium*, pages 779–783. IEEE, 2004.

[95] S. Meister, B. Jähne, and D. Kondermann. Outdoor stereo camera system for the generation of real-world benchmark data sets. *Optical Engineering*, 51(02):021107, 2012.

[96] Sandino Morales and Reinhard Klette. Ground truth evaluation of stereo algorithms for real world applications. In *Computer Vision–ACCV 2010 Workshops*, pages 152–162. Springer, 2011.

[97] Karsten Mühlmann, Dennis Maier, Jürgen Hesser, and Reinhard Männer. Calculating dense disparity maps from color stereo images, an efficient implementation. *International Journal of Computer Vision*, 47(1-3):79–88, 2002.

[98] Harsh Nanda and Larry Davis. Probabilistic template based pedestrian detection in infrared videos. In *Intelligent Vehicle Symposium*, volume 1, pages 15–20. IEEE, 2002.

[99] Sergiu Nedevschi, Silviu Bota, and Corneliu Tomiuc. Stereo-based pedestrian detection for collision-avoidance applications. *IEEE Transactions on Intelligent Transportation Systems*, 10(3):380–391, 2009.

[100] Timo Ojala, Matti Pietikäinen, and David Harwood. A comparative study of texture measures with classification based on featured distributions. *Pattern recognition*, 29(1): 51–59, 1996.

[101] Masatoshi Okutomi, Osamu Yoshizaki, and Goji Tomita. Color stereo matching and its application to 3-d measurement of optic nerve head. In *11th IAPR International Conference on Pattern Recognition*, pages 509–513. IEEE, 1992.

[102] Daniel Olmeda, Jose Maria Armingol, and Arturo de la Escalera. Discrete features for rapid pedestrian detection in infrared images. In *IEEE/RSJ International Conference on Intelligent Robots and Systems (IROS)*, pages 3067–3072. IEEE, 2012.

[103] Daniel Olmeda, Cristiano Premebida, Urbano Nunes, Jose Maria Armingol, and Arturo de la Escalera. Pedestrian detection in far infrared images. *Integrated Computer-Aided Engineering*, 20(4):347–360, 2013.

[104] World Health Organization et al. Global status report on road safety 2013: supporting a decade of action. 2013.

[105] Gary Overett, Lars Petersson, Nathan Brewer, Lars Andersson, and Niklas Pettersson. A new pedestrian dataset for supervised learning. In *Intelligent Vehicles Symposium*, pages 373–378. IEEE, 2008.

[106] Constantine Papageorgiou and Tomaso Poggio. A trainable system for object detection. *International Journal of Computer Vision*, 38(1):15–33, 2000.

[107] Tomaso Poggio, Vincent Torre, and Christof Koch. Computational vision and regularization theory. *Image understanding*, 3(1-18):111, 1989.

[108] W. Richards. Stereopsis and stereoblindness. *Experimental Brain Research*, 10(4):380–388, 1970.

[109] Marcus Rohrbach, Markus Enzweiler, and Dariu M Gavrila. High-level fusion of depth and intensity for pedestrian classification. In *Pattern Recognition*, pages 101–110. Springer, 2009.

[110] Indranil Sarkar and Manu Bansal. A wavelet-based multiresolution approach to solve the stereo correspondence problem using mutual information. *IEEE Transactions on Systems, Man, and Cybernetics, Part B: Cybernetics*, 37(4):1009–1014, 2007.

[111] Ashutosh Saxena, Jamie Schulte, and Andrew Y Ng. Depth estimation using monocular and stereo cues. IJCAI, 2007.

[112] D. Scharstein and R. Szeliski. A taxonomy and evaluation of dense two-frame stereo correspondence algorithms. *International journal of computer vision*, 47(1):7–42, 2002.

[113] Jan Portmann Simon Lynen. Ethz thermal infrared dataset. *http://projects.asl.ethz.ch/datasets/doku.php?id=ir:iricra2014*, 2014.

[114] C Stentoumis, L Grammatikopoulos, I Kalisperakis, E Petsa, and G Karras. A local adaptive approach for dense stereo matching in architectural scene reconstruction. XL: XL–5/W1,219–226, 2013.

[115] F. Suard, A. Rakotomamonjy, A. Bensrhair, and A. Broggi. Pedestrian detection using infrared images and histograms of oriented gradients. In *Intelligent Vehicles Symposium*, pages 206–212. Ieee, 2006.

[116] Deqing Sun, Stefan Roth, and Michael J Black. A quantitative analysis of current practices in optical flow estimation and the principles behind them. *International Journal of Computer Vision*, 106(2):115–137, 2014.

[117] H. Sun, C. Hua, and Y. Luo. A multi-stage classifier based algorithm of pedestrian detection in night with a near infrared camera in a moving car. In *Proceedings Third International Conference on Image and Graphics*, pages 120–123. IEEE, 2004.

[118] Hao Sun, Cheng Wang, and Boliang Wang. Night vision pedestrian detection using a forward-looking infrared camera. In *International Workshop on Multi-Platform/Multi-Sensor Remote Sensing and Mapping (M2RSM)*, pages 1–4. IEEE, 2011.

[119] Jian Sun, Nan-Ning Zheng, and Heung-Yeung Shum. Stereo matching using belief propagation. *IEEE Transactions on Pattern Analysis and Machine Intelligence*, 25(7):787–800, 2003.

[120] Richard Szeliski, Ramin Zabih, Daniel Scharstein, Olga Veksler, Vladimir Kolmogorov, Aseem Agarwala, Marshall Tappen, and Carsten Rother. A comparative study of energy minimization methods for markov random fields with smoothness-based priors. *IEEE Transactions on Pattern Analysis and Machine Intelligence*, 30(6):1068–1080, 2008.

[121] Carlo Tomasi and Roberto Manduchi. Bilateral filtering for gray and color images. In *Sixth International Conference on Computer Vision*, pages 839–846. IEEE, 1998.

[122] Jürgen Valldorf and Wolfgang Gessner. *Advanced microsystems for automotive applications 2005*. Springer Verlag, Berlin, June 2005. ISBN: 3540334092.

[123] W. van der Mark and D.M. Gavrila. Real-time dense stereo for intelligent vehicles. *Transactions on Intelligent Transportation Systems*, 7(1):38–50, 2006. ISSN 1524-9050.

[124] R.F. van der Willigen, W.M. Harmening, S. Vossen, and H. Wagner. Disparity sensitivity in man and owl: Psychophysical evidence for equivalent perception of shape-from-stereo. *Journal of vision*, 10(1), 2010.

[125] O. Veksler. Stereo correspondence by dynamic programming on a tree. In *IEEE Computer Society Conference on Computer Vision and Pattern Recognition*, volume 2, pages 384–390. IEEE, 2005. ISBN 0769523722.

[126] Paul Viola, Michael J Jones, and Daniel Snow. Detecting pedestrians using patterns of motion and appearance. In *9th IEEE International Conference on Computer Vision*, pages 734–741. IEEE, 2003.

[127] S. Walk, N. Majer, K. Schindler, and B. Schiele. New features and insights for pedestrian detection. In *IEEE Conference on Computer Vision and Pattern Recognition*, pages 1030–1037. IEEE, 2010.

[128] Stefan Walk, Konrad Schindler, and Bernt Schiele. Disparity statistics for pedestrian detection: Combining appearance, motion and stereo. In *European Conference on Computer Vision*, pages 182–195. Springer, 2010.

[129] Jiabao Wang, Yafei Zhang, Jianjiang Lu, and Yang Li. Target detection and pedestrian recognition in infrared images. *Journal of Computers*, 8(4), 2013.

[130] Menghua Wang and Wei Shi. The nir-swir combined atmospheric correction approach for modis ocean color data processing. *Optics Express*, 15(24):15722–15733, 2007.

[131] Xiaoyu Wang, Tony X Han, and Shuicheng Yan. An hog-lbp human detector with partial occlusion handling. In *12th International Conference on Computer Vision*, pages 32–39. IEEE, 2009.

[132] Christian Wojek, Stefan Walk, and Bernt Schiele. Multi-cue onboard pedestrian detection. In *IEEE Conference on Computer Vision and Pattern Recognition*, pages 794–801, 2009.

[133] Q. Yang, L. Wang, R. Yang, S. Wang, M. Liao, and D. Nister. Real-time global stereo matching using hierarchical belief propagation. In *The British Machine Vision Conference*, pages 989–998, 2006.

[134] M. Yasuno, S. Ryousuke, N. Yasuda, and M. Aoki. Pedestrian detection and tracking in far infrared images. In *Proceedings Intelligent Transportation Systems*, pages 182–187. IEEE, 2005.

[135] Kuk-Jin Yoon and In-So Kweon. Locally adaptive support-weight approach for visual correspondence search. In *IEEE Conference on Computer Vision and Pattern Recognition*, volume 2, pages 924–931. IEEE, 2005.

[136] R. Zabih and J. Woodfill. Non-parametric local transforms for computing visual correspondence. *Computer Vision NECCV'94*, pages 151–158, 1994.

[137] Ke Zhang, Jiangbo Lu, and Gauthier Lafruit. Cross-based local stereo matching using orthogonal integral images. *IEEE Transactions on Circuits and Systems for Video Technology*, 19(7):1073–1079, 2009.

[138] Li Zhang, Bo Wu, and Ram Nevatia. Pedestrian detection in infrared images based on local shape features. In *IEEE Conference on Computer Vision and Pattern Recognition*, pages 1–8, 2007.

[139] Liang Zhao and Charles E Thorpe. Stereo-and neural network-based pedestrian detection. *IEEE Transactions on Intelligent Transportation Systems*, 1(3):148–154, 2000.